Quantum critical phenomena in two-dimensional fermion systems

Von der Fakultät für Mathematik, Informatik und Naturwissenschaften der RWTH Aachen University zur Erlangung des akademischen Grades eines Doktors der Naturwissenschaften genehmigte Dissertation

vorgelegt von

Stephan Heßelmann, M.Sc.

aus

Lüdinghausen

Berichter: Prof. Stefan Weßel, Ph. D.
Prof. Carsten Honerkamp, Ph. D.

Tag der mündlichen Prüfung: 03.12.2020

Eidesstattliche Erklärung

Ich, Stephan Heßelmann, erkläre hiermit, dass diese Dissertation und die darin dargelegten Inhalte die eigenen sind und selbstständig, als Ergebnis der eigenen originären Forschung, generiert wurden.

Hiermit erkläre ich an Eides statt

1. Diese Arbeit wurde vollständig oder größtenteils in der Phase als Doktorand dieser Fakultät und Universität angefertigt;
2. Sofern irgendein Bestandteil dieser Dissertation zuvor für einen akademischen Abschluss oder eine andere Qualifikation an dieser oder einer anderen Institution verwendet wurde, wurde dies klar angezeigt;
3. Wenn immer andere eigene- oder Veröffentlichungen Dritter herangezogen wurden, wurden diese klar benannt;
4. Wenn aus anderen eigenen- oder Veröffentlichungen Dritter zitiert wurde, wurde stets die Quelle hierfür angegeben. Diese Dissertation ist vollständig meine eigene Arbeit, mit der Ausnahme solcher Zitate;
5. Alle wesentlichen Quellen von Unterstützung wurden benannt;
6. Wenn immer ein Teil dieser Dissertation auf der Zusammenarbeit mit anderen basiert, wurde von mir klar gekennzeichnet, was von anderen und was von mir selbst erarbeitet wurde;
7. Teile dieser Arbeit wurden zuvor veröffentlicht und zwar in: [1–4]

Stephan Heßelmann, M.Sc.
December 2020

Acknowledgements

I would like to thank my advisor Stefan Wessel for his guidance and patience, as well as giving me the opportunity to work on many challenging research projects. I would also like to thank my secondary advisor Carsten Honerkamp for his always friendly demeanor and of course many interesting discussions, scientific and otherwise.

Next I want to thank all of my other collaborators for their great work. In particular, I thank Michael Schuler and Andreas Läuchli for their long standing collaboration on the torus spectroscopy project, Thomas Lang for many helpful discussions about all things Monte Carlo and beyond, and Michael Scherer for being a great teacher of field theory and other topics.

I also want to thank Zi Yang Meng and his group members for providing great hospitality during my stay in Beijing, in addition to facilitating many fruitful discussions. I thank Lei Wang for his scientific openness and willingness to publish his code, which has helped me a lot in my own projects.

I am grateful for the RTG1995, which has supported my position financially and allowed me to travel freely to many interesting places. I also acknowledge computing time provided via the JARA-HPC program.

I would like to thank my colleagues at the RWTH for many discussions and helpful insights, in particular Gulio Schober for his meticulous approach to fRG, and my longtime friend and office mate Jonas Becker for his support. Finally, I thank my family, friends and everyone else who has otherwise supported me.

List of publications

- **Stephan Hesselmann** and Stefan Wessel
  Thermal Ising transitions in the vicinity of two-dimensional quantum critical points
  Phys. Rev. B **93**, 155157 (2016)

- **Stephan Hesselmann**, Daniel D. Scherer, Michael M. Scherer and Stefan Wessel
  Bond-ordered states and f-wave pairing of spinless fermions on the honeycomb lattice
  Phys. Rev. B **98**, 045142 (2018)

- Michael Schuler, **Stephan Hesselmann**, Seth Whitsitt, Thomas C. Lang, Stefan Wessel and Andreas M. Läuchli
  Torus Spectroscopy of the Gross-Neveu-Yukawa Quantum Field Theory: Free Dirac versus Chiral Ising Fixed Point
  arXiv:1907.05373, submitted to Phys. Rev. X (2019)

- **Stephan Hesselmann**, Thomas C. Lang, Michael Schuler, Stefan Wessel and Andreas M. Läuchli
  Comment on "The role of electron-electron interactions in two- dimensional Dirac fermions"
  Science **366** (2019)

- **Stephan Hesselmann**, Carsten Honerkamp, Stefan Wessel and Thomas C. Lang
  Quantifying the fragility of unprotected quadratic band crossing points
  Phys. Rev. B **101**, 075128 (2020)

Abstract

In this thesis I investigate the critical behavior of two-dimensional fermion systems in the vicinity of various phase transitions. While critical phenomena in classical systems have been studied for a long time, quantum phase transitions in fermionic systems have generated a great amount of current interest, contributing to the understanding of, e.g., graphene and high temperature superconductors. This work consists of several projects, most of which focus on the $t - V$ model of spinless fermions on the honeycomb lattice and its phase transitions.

The $t - V$ model, at half-filling, features a quantum critical point of the chiral Ising universality class. In contrast to the conventional Ising universality, this transition includes critical fermionic fields that couple to the order parameter field. I study the behavior of thermal Ising transitions in the vicinity of such a quantum phase transition, and explore further universal features. Furthermore, I present a novel approach to characterize critical points by performing a torus spectroscopy analysis. At the critical point, the low-energy gaps of the lattice model form a universal fingerprint of the transition. This fingerprint is not only characteristic of the quantum phase transition in the lattice model, but also connects to fixed points of the Gross-Neveu-Yukawa field theory. To calculate physical observables and energy gaps, I employ quantum Monte Carlo simulations, which only after rather recent developments can be formulated without a sign-problem.

Finally, I investigate a parameter regime inaccessible to quantum Monte Carlo by breaking the particle-hole symmetry of the model with a finite chemical potential. This allows for the probing of instabilities towards phases beyond half-filling. To perform the instability analysis, I employ functional renormalization group methods with a Fermi surface patching. This method is unbiased towards potential phases, because it treats instabilities in the particle-hole and particle-particle channels on an equal footing. In addition to the commensurate charge-density-wave instability of the half-filled case, I identify a bond-order instability, located at the van Hove filling, and an f-wave superconducting instability at further doping.

Abstract

In dieser Dissertation untersuche ich das kritische Verhalten von zwei-dimensionalen Fermionsystemen in der Nähe von verschiedenen Phasenübergängen. Obwohl das kritsches Verhalten von klassischen System seit langer Zeit untersucht wird, haben Quantenphasenübergänge in Fermionsystemen ein großes Interesse in der aktuellen Forschung erweckt, weil sie zum Verständnis von, unter anderem, Graphen und Hochtemperatursupraleiter beitragen. Die Dissertation besteht aus mehreren Projekten, die meisten davon beziehen sich auf das $t - V$ Modell von spinlosen Fermionen auf dem Honigwabengitter und dessen Phasenübergänge.

Das $t - V$ Modell, bei halber Füllung, besitzt einen quantenkritischen Punkt der chiralen Ising Universalitätsklasse. Im Gegensatz zur konventionellen Ising Universalitätsklasse, behinhaltet dieser Übergang kritische fermionische Felder, die an das Ordnungsparameterfeld koppeln. Ich studiere das Verhalten von thermischen Phasenübergängen in der Nähe eines solchen Quantenphasenübergangs und untersuche weitere universelle Eigenschaften. Weiterhin präsentiere ich einen neuen Ansatz zur Charakterisierung von kritischen Punkten durch eine Spektroskopie-Analyse des Torusspektrums. Am kritischen Punkt bilden die Energielücken des Gittermodells einen universellen Fingerabdruck des Übergangs. Dieser Fingerabdruck ist nicht nur characteristisch für den Quantenphasenübergang des Gittermodells, sondern ist auch mit den Fixpunkten der Gross-Neveu-Yukawa Feldtheorie verbunden. Um die physikalischen Observablen und Energielücken zu berechnen, verwende ich Quantum-Monte-Carlo-Simulationen, welche erst seit Kurzem ohne Vorzeichenproblem formuliert werden können.

Zuletzt untersuche ich einen für Quantum-Monte-Carlo nicht zugänglichen Parameterbereich, in welchem die Teilchen-Loch-Symmetrie des Modells durch ein endliches chemisches Potential gebrochen ist. Das erlaubt es, die Instabilität des Systems gegenüber verschiedenen Phases außerhalb des halb-gefüllten Regimes zu testen. Für diese Instabilitätsanalyse benutze ich die funktionale Renormierungsgruppe mit einem Patching der Fermioberfläche. Diese Methode ist unbefangen gegenüber potentiellen Phasen, weil sie Instabilitäten im Teilchen-Loch-Kanal und Teilchen-Teilchen-Kanal gleichwertig behandelt. Zusätzlich zur gleichmäßigen Ladungsdichtewelle des halb gefüllten Systems, identifiziere ich eine Instabilität gegenüber Bindungsordnung bei der van Hove-Füllung und eine supraleitende Phase mit f-Wellensymmetrie bei erhöhter Dotierung.

Contents

Chapter 1

Introduction

The present dissertation discusses the issue of quantum critical phenomena as it appears in the solution to the quantum many-body problem. I will focus on the key aspects of *symmetry* and *emergence*, which in combination are responsible for much of the complexity encountered in condensed matter physics. The symmetry of a physical system signifies that it appears identical under a different point of view. More concretely, it refers to the system's invariance under symmetry transformations, such as translations and rotations in real space, time reversal or particle-hole transformations. The concept of symmetry is fundamental in physics for many reasons. For one, continuous symmetries are directly related to conserved quantities via the celebrated Noether theorem. More generally, it is also a common property of the microscopic laws of physics, such as the many-body Schrödinger equation, and the observable phases of matter that make up our macroscopic world. This connection is however highly non-trivial, because the symmetry of the macroscopic physical state can differ from that of its microscopic constituents. Systems in which this situation occurs are said to exhibit spontaneous symmetry breaking.

At this point emergence becomes relevant as a second fundamental concept besides symmetry. The essential idea of emergence is that 'the whole is more than the sum of its parts'. If one tries to build a system up from microscopic laws to macroscopic scale, the emerging complexity leads to additional fundamental laws that govern the macroscopic system. In many-body systems this transformation can be formalized mathematically by the thermodynamic limit (sometimes referred to as the $N \to \infty$ limit). This limit is essential for the system to realize phase transitions involving macroscopic states which break the microscopic symmetries spontaneously. The topic of spontaneous symmetry breaking is broad and has many important applications in all fields of physics, and much of the work in this dissertation deals with its details in the context of quantum many-body systems.

The dissertation is organized in six different chapters. This first chapter gives a brief introduces to relevant concepts and models, which will be referenced in later chapters. Conversely, the last chapter offers a conclusion of the thesis as well as a brief outlook of prospective future work.

Chapter 2 deals with the technical details of the quantum Monte-Carlo (QMC) algorithms used in later chapters. In particular, I will give implementation details of the continuous time interaction expansion method (CT-INT) used in Chapter 3, as well as different formulations of the determinantal quantum Monte-Carlo method (DQMC) used in chapter 4. Each of the quantum Monte-Carlo variants deals with the simulation of the $t - V$ model, which describes spinless fermions on the honeycomb lattice, and can be formulated without sign-problem. Differences arise in the statistical sampling processes, which are optimized to measure physical observables either at a finite temperature or with respect to the many-body ground state.

The following chapters are dedicated to the results of individual projects completed during my doctoral studies. All of them share the common aspect of quantum critical phenomena in two dimensional many-body systems, but each highlights a different point of view to the underlying physics. In Chapter 3 I discuss thermal phase transitions in the vicinity of a quantum critical point (QCP), and the interplay of the corresponding classical and quantum scaling regimes. The starting point is the transverse field Ising model, which features a QCP that separates a ferromagnetic phase from a disordered phase. Next is a discussion of the fermionic QCP realized in the aforementioned $t - V$ model, which can be understood as a lattice implementation of the Gross-Neveu-Yukawa (GNY) field theory. The extends of the different scaling regimes are identified, and their critical exponents are calculated using data generated by QMC simulations.

In chapter 4 I present a generalization of the torus spectroscopy technique to the GNY field theory. The key idea is to calculate the critical, low energy torus spectrum of finite clusters, and promote it as a universal fingerprint of the corresponding field theory that characterizes the QCP. I detail how the torus spectrum of the $t - V$ model can be obtained using QMC simulations, and discuss the results in the context of exact diagonlization (ED) and ϵ-expansion calculations performed by my collaborators. Additional insight into the renormalization of the Fermi velocity in the vicinity of QCP is also provided.

Chapter 5 focuses on the $t - V$ model at finite doping. I first lay out the essentials of the functional renormalization group (fRG) as a complementary approach to QMC, because for a finite chemical potential, the $t - V$ model generates a sign-problem in QMC simulations. I therefore employ the fRG to study the instabilities of the $t - V$ beyond half-filling. The main result is a tentative $V - \mu$ phase diagram, which includes the standard charge-density-wave

(CDW) at half-filling, a bond-ordered state at the van Hove filling and a superconducting state with f-wave symmetry at increased doping.

1.1 Spontaneous symmetry breaking and phase transitions

Phases describe different states of matter with distinct physical properties, which are determined by the particles in the system, their interactions and external parameters. Each phase encompasses a connected region in the parameter space of the system, which consists of both Hamiltonian parameters as well as physical variables that describe the thermodynamic equilibrium of the system, such as temperature or chemical potential. As one phase transitions to another, the physical properties of the system change abruptly. In many cases, the transition is between a disordered and a long-range ordered state. In this case, the onset of the ordered phase is signaled by increased correlations of a local quantity, which diverge at the point of the transition. These quantities are denoted as order parameters, because their expectation value is zero in one phase, and finite in the other. As their name suggests, the correlation of a local order parameters over an infinite length scale signifies long range order, which breaks the original symmetry of the Hamiltonian. In this case, the order parameter is related to an infinitesimal external perturbation, which breaks the symmetry of the Hamiltonian spontaneously. Since this process requires a true divergence in the free energy, it is only defined for systems containing infinite particles.

In the traditional Landau-Ginzburg paradigm of classifying phase transitions [5], the order parameter is defined as the first derivative of the free energy with respect to an external perturbation parameter. The external perturbation is chosen such that is breaks the symmetry of the system and induces the long-range order, e.g., the magnetization of a system indicates magnetic order, and is related to a magnetic field. Similarly, the susceptibility is given by the second derivative of the free energy with respect to said parameter. If the order parameter changes discontinuously from zero to a finite value, the phase transition is of first order. If it changes continuously, the divergence is found in higher derivatives of the free energy. In particular, second order phase transitions are continuous in the order parameter, but show a divergent susceptibility. They are of particular interest in statistical physics, because they exhibit universality and can be described using scaling theory.

Most of this thesis deals with the investigation of such second order (or continuous) phase transitions. The order parameter correlations define a new length scale in the system. Upon approaching the phase transition, this correlation length diverges, and thus, the order parameter fluctuates over all possible length scales. This process washes out microscopic details of the original system, and only leaves a handful of fundamental properties that define

the universality class of the phase transition. In particular, the universality classes contain critical exponents, which determine the behavior of critical quantities and correlations in the vicinity of the phase transition.

For thermal phase transitions, the control parameter that drives the transition is given by the temperature of the system in thermal equilibrium. The correlation length ξ then scales as

$$\xi \propto |t|^{\nu}, \tag{1.1}$$

where $t = \frac{T-T_c}{T_c}$ is the reduced temperature, and ν is a critical exponent. Another important scaling relation is given by the decay of order parameter correlations right at the critical point ($t = 0$),

$$\langle \phi(\boldsymbol{r}_i)\phi(\boldsymbol{r}_j)\rangle \propto |\boldsymbol{r}_i - \boldsymbol{r}_j|^{2-d-\eta}, \tag{1.2}$$

where $\phi(\boldsymbol{r})$ denotes the order parameter at position $\boldsymbol{r}$, d is the dimension and η is the anomalous exponent. Further universal exponents related to the scaling of different thermodynamic quantitites can be defined, however most of them are not independent and can be obtained from universal scaling relations.

In contrast to thermal phase transitions, quantum phase transitions take place at zero temperature, and instead of thermal fluctuations in the order parameter expectation value, they are driven by quantum fluctuations in the many-body ground state. This leads to an additional correlation length in imaginary time $\xi_\tau \propto \xi^z$, where the dynamical critical exponent z relates temporal and spatial degrees of freedom. Formally, one can understand the critical quantum system as a classical system of increased dimension $d_{\text{qm}} = z + d$ using the so-called quantum-to-classical mapping [6].

1.2 The honeycomb lattice

The geometry of the honeycomb lattice is interesting, in particular because its two-atomic unit cell and hexagonal structure leads to the emergence of Dirac cones in the dispersion relation of tight-binding models. The Bravais lattice of the honeycomb lattice is equivalent to a triangular lattice with two sites per lattice cell. Fig. 1.1 displays the two most commonly used definitions of the honeycomb lattice. In addition to the orientation, the lattice constant a is a free parameter. In the following chapters, we will stick to $a = 1$ for simplicity.

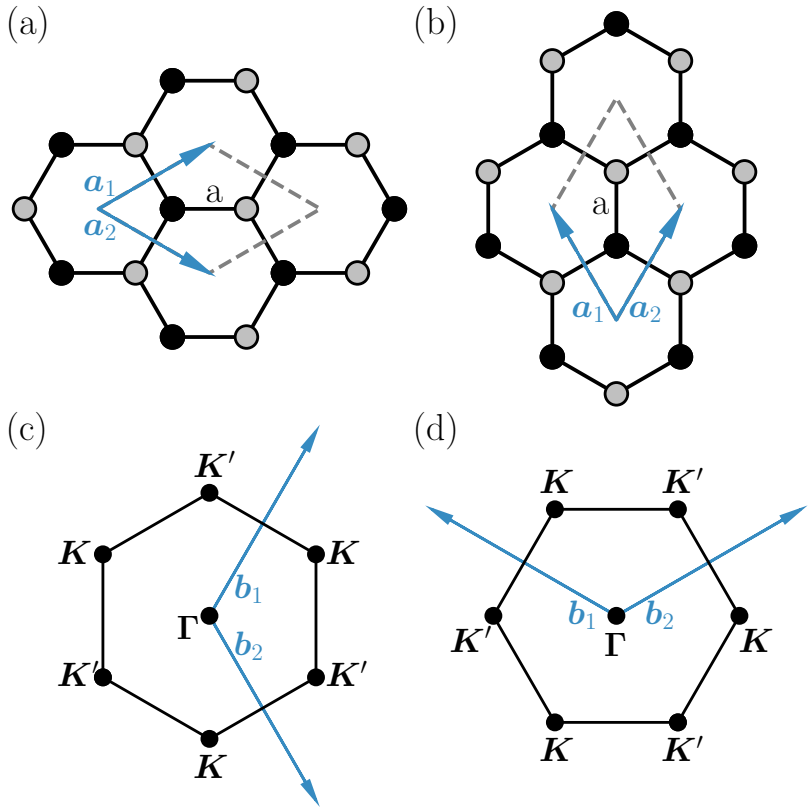

Figure 1.1: Two common definitions of the honeycomb lattice in real and reciprocal space. Panels (a) and (b) show the honeycomb lattice in real space, $\boldsymbol{a}_1$ and $\boldsymbol{a}_2$ are the lattice vectors, a is the lattice constant, and the unit cells are indicated by the dashed lines. The unit cell in (b) is rotated by $90°$ with respect to the on in (a). Panels (c) and (d) show the first Brillouin zones corresponding to (a) and (b) respectively, and $\boldsymbol{b}_1$ and $\boldsymbol{b}_2$ indicate the unit vectors in reciprocal space. The Dirac points K and K' are located at the corners of the Brillouin zones, while the Γ point is in the center.

The unit vectors of the Bravais lattice for the horizontal orientation, cf. panels (a) and (c) in Fig. 1.1, are given by

$$\boldsymbol{a}_1 = \frac{a}{2}\begin{pmatrix} 3 \\ \sqrt{3} \end{pmatrix}, \quad \boldsymbol{a}_2 = \frac{a}{2}\begin{pmatrix} 3 \\ -\sqrt{3} \end{pmatrix}. \tag{1.3}$$

The corresponding unit vectors in reciprocal space are

$$\boldsymbol{b}_1 = \frac{2\pi}{3a}\begin{pmatrix} 1 \\ -\sqrt{3} \end{pmatrix}, \quad \boldsymbol{b}_2 = \frac{2\pi}{3a}\begin{pmatrix} 1 \\ \sqrt{3} \end{pmatrix}, \tag{1.4}$$

and the high symmetry points of the Brillouin zone are given by

$$\boldsymbol{\Gamma} = \begin{pmatrix} 0 \\ 0 \end{pmatrix}, \quad \boldsymbol{K} = \frac{2\pi}{3\sqrt{3}a} \begin{pmatrix} 1 \\ \sqrt{3} \end{pmatrix}, \quad \boldsymbol{K'} = \frac{2\pi}{3\sqrt{3}a} \begin{pmatrix} 1 \\ -\sqrt{3} \end{pmatrix}. \tag{1.5}$$

The vectors of the vertical orientation follow from these by applying a $90°$ rotation.

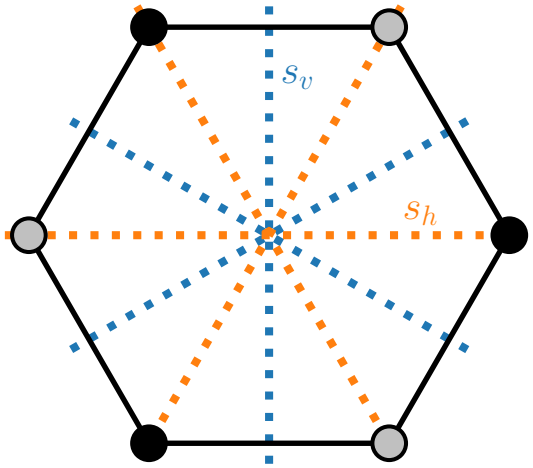

Figure 1.2: Symmetry properties of the honeycomb lattice. The lattice sites are invariant under $60°$, $120°$ and $180°$ rotations about the center of the hexagons. Furthermore, they can be reflected along the mirror axes s_v and s_h.

The honeycomb lattice is symmetric under operations of the D_6 point group, cf. Fig. 1.2, which includes rotations about $60°$, $120°$ and $180°$ about the hexagon center, as well as reflections along axes through the hexagon center. Note that not all of these operations leave the sublattices invariant, but rather map sites from one sublattice to the other.

1.3 The honeycomb $t - V$ model

The $t - V$ model of spinless fermions on the honeycomb lattice is one of the simplest Hubbard-type models that provides graphene-like physics. Its Hamiltonian consists of a nearest-neighbor hopping with amplitude t and a repulsive nearest-neighbor interaction V,

$$\begin{aligned} H &= H_0 + H_I \\ &= -t \sum_{\langle i,j \rangle} \left(c_i^\dagger c_j + c_j^\dagger c_i \right) + V \sum_{\langle i,j \rangle} \left(n_i - \frac{1}{2} \right) \left(n_i - \frac{1}{2} \right), \end{aligned} \tag{1.6}$$

where $c_i^\dagger$ (c_i) are fermionic creation (annihilation) operators and $n_i = c_i^\dagger c_i$ are local density operators. Note that in this notation $\langle i, j \rangle$ labels individual neighboring sites rather than the unit cells, i.e. the proper unit cells and sublattice indices are implied. In addition to the D_6 symmetry of by the honeycomb lattice, the Hamiltonian is also invariant under particle-hole transformations,

$$c_i \to \begin{cases} c_i^\dagger, & i \in A \\ -c_i^\dagger, & i \in B \end{cases}, \tag{1.7}$$

as well as time-reversal transformations,

$$c_{\boldsymbol{k}} \to c_{-\boldsymbol{k}}. \tag{1.8}$$

1.3.1 Tight binding approximation

It is instructive to first consider the Hamiltonian Eq. (1.6) without interactions ($V = 0$). The remaining Hamiltonian is equivalent to the tight binding approximation [7]

$$H_0 = -t \sum_{\boldsymbol{R}} \sum_{i=1,2,3} \left(c_{\boldsymbol{R},A}^\dagger c_{\boldsymbol{R}+\boldsymbol{\delta_i},B} + c_{\boldsymbol{R}+\boldsymbol{\delta_i},B}^\dagger c_{\boldsymbol{R},A} \right), \tag{1.9}$$

where we have highlighted the bipartite structure of the honeycomb lattice by using separate creation/annihilation operators for each sublattice and sum over the positions of each unit cell $\boldsymbol{R}$,

$$c_i = \begin{cases} c_{\boldsymbol{R_i},A}, & i \in \text{ sublattice A} \\ c_{\boldsymbol{R_i},B}, & i \in \text{ sublattice B} \end{cases}, \tag{1.10}$$

as well distance vectors between neighboring unit cells

$$\boldsymbol{\delta} = (-\boldsymbol{a_2}, \boldsymbol{a_1}, -\boldsymbol{a_2}). \tag{1.11}$$

In order to obtain the free dispersion relation we the discrete Fourier transform (L is the number of unit cells in both $\boldsymbol{a}_1$ and $\boldsymbol{a}_2$ direction)

$$c_{\boldsymbol{R},o} = \frac{1}{L} \sum_{\boldsymbol{R}} e^{i\boldsymbol{k}\cdot\boldsymbol{R}} c_{\boldsymbol{k},o}, \tag{1.12}$$

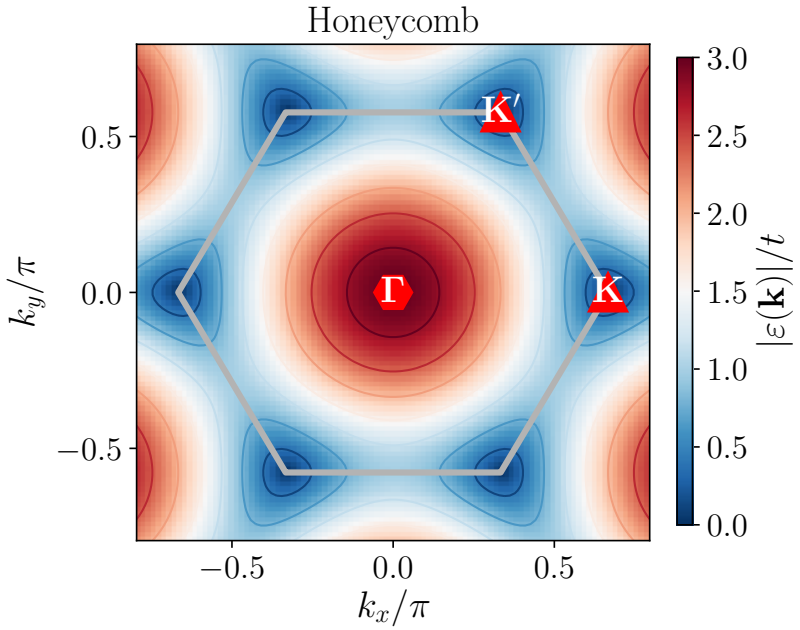

Figure 1.3: Free dispersion of the $t-V$ honeycomb model. Dirac cones with linear dispersion can be found at the $\boldsymbol{K}$ and $\boldsymbol{K}'$ points.

which allows us to rewrite the Hamiltonian in matrix notation

$$H_0 = \sum_{\boldsymbol{k}} \sum_{i=1,2,3} \left(c^\dagger_{\boldsymbol{k},A} c^\dagger_{\boldsymbol{k},B}\right) \begin{pmatrix} 0 & te^{-i\boldsymbol{k}\cdot\boldsymbol{\delta_i}} \\ te^{i\boldsymbol{k}\cdot\boldsymbol{\delta_i}} & 0 \end{pmatrix} \begin{pmatrix} c_{\boldsymbol{k},A} \\ c_{\boldsymbol{k},B} \end{pmatrix}. \tag{1.13}$$

The band structure can then be obtained by a further diagonalization, which yields

$$H_0 = \sum_{\boldsymbol{k},b\in\{c,v\}} \epsilon(\boldsymbol{k}) \alpha^\dagger_{\boldsymbol{k},b} \alpha_{\boldsymbol{k},b}, \tag{1.14}$$

where we have introduced a conduction and valence band with respective single-particle energies

$$\epsilon(\boldsymbol{k}) = \pm\sqrt{3 + 2\cos(\boldsymbol{k}\cdot(\boldsymbol{a_2}-\boldsymbol{a_1})) + 2\cos(\boldsymbol{k}\cdot\boldsymbol{a_1}) + 2\cos(\boldsymbol{k}\cdot\boldsymbol{a_2})}. \tag{1.15}$$

The tight-binding dispersion Eq. (1.15) features Dirac cones with a linearized dispersion, cf. Fig. 1.3, which can be seen explicitly by expanding about the high symmetry points $\boldsymbol{K}$ or $\boldsymbol{K'}$ (cf. Fig. 1.1),

$$\epsilon(\boldsymbol{q} = \boldsymbol{K} - \boldsymbol{k}) = \pm v_F |\boldsymbol{q}| + \mathcal{O}\left(\left(\frac{|\boldsymbol{q}|}{|\boldsymbol{K}|}\right)^2\right). \tag{1.16}$$

The free Fermi velocity is given by $v_F = \frac{3t}{2}$. Since the Fermi surface at half-filling consists only of singular points located at $\boldsymbol{K}$ and $\boldsymbol{K}'$, the ground state is considered a semi-metallic state of matter. Furthermore, the linear dispersion around the Fermi points protects the semi-metallic phase against perturbative short-ranged interactions [8]. Hence, a finite interaction $V_c > 0$ is required to induce a quantum phase transition towards any symmetry-broken phase.

1.3.2 Strong coupling limit

In the strong coupling limit, $V \gg t$, the interacting part of the Hamiltonian effectively maps onto an antiferromagnetic Ising model,

$$\lim_{V/t\to\infty} H_I/t \sim J \sum_{\langle i,j\rangle} \sigma_i \sigma_j, \tag{1.17}$$

with $J = \frac{V}{4t}$ and classical field variables $\sigma_i = \pm 1$. The antiferromagnetic ground state of the Ising model then corresponds to a fermionic model with one fully occupied and one empty sublattice. This configuration corresponds to a commensurate charge-density-wave, which breaks the Z_2 sublattice symmetry of the honeycomb lattice. The onset of the charge-density-wave can be detected by an inequality in the particle density of each sublattice, i.e.

$$\langle n_A \rangle \neq \langle n_B \rangle. \tag{1.18}$$

1.4 Gross-Neveu-Yukawa field theory

Effective quantum field theories (QFTs) of fermionic lattice models provide important insight into the nature of the quantum phase transitions in such models. In particular, the $t-V$ model is regarded as a lattice implementation of various phases of the Gross-Neveu-Yukawa theory of fermionic fields coupled to a Z_2 order parameter in $D = 3$ space-time dimensions [8–10]. The GNY theory encompasses both the semi-metallic phase of Dirac fermions as well as the Z_2 symmetry broken phase. Between those two phases, the theory flows to a fixed point, which describes a quantum critical point of the chiral Ising universality class [11, 12]. The Lagrangian of the GNY theory is given by

$$\mathcal{L}_{\text{GNY}} = -\overline{\Psi}^j \left(\not{\partial} + g_{\text{Y}}\, \phi\right) \Psi^j + \frac{1}{2}\phi \left(s - \partial^2\right) \phi + \frac{\lambda}{4!}\phi^4\,, \tag{1.19}$$

where Ψ^j is an n_{D}-component Dirac spinor with $j = 1, ..., N_f$ flavors and the total number of fermionic degrees of freedom is $N = n_{\mathrm{D}} N_f$. The real scalar field is denoted by ϕ, and g_{Y} is the Yukawa coupling strength between the spinor and scalar fields. In our notation we have $\not{\partial} = \gamma^\mu \partial_\mu$, $\mu \in \{0, \dots D-1\}$ and $\overline{\Psi} = \Psi \gamma^0$, where the γ^μ are $n_{\mathrm{D}} \times n_{\mathrm{D}}$ matrices satisfying the Clifford algebra, $\{\gamma^\mu, \gamma^\nu\} = 2\delta^{\mu\nu}$.

In $D = 3$, the GNY theory features three distinct fixed points, dependent on the tuning parameter s, which describe effective field theories for the semi-metallic phase, the symmetry-broken charge-density-wave, and the quantum critical point in between. For the critical value $s = s_c$ the GNY flows towards the fermionic chiral Ising fixed point, which characterizes the universality class of the quantum phase transition. Importantly, its effective theory includes critical fluctuations of both the fermionic field and the real scalar field. The investigation of this fixed point is non-trivial and will be the topic of later chapters.

For $s < s_c$, the scalar order parameter acquires a finite expectation value, $\langle \phi \rangle \neq 0$, which spontaneously breaks the Z_2 parity symmetry of the theory, which here corresponds to

$$(x^0, x^1, x^2) \to (x^0, -x^1, x^2) \tag{1.20}$$

$$\Psi \to \gamma^1 \Psi \tag{1.21}$$

$$\overline{\Psi} \to -\overline{\Psi} \gamma^1 \tag{1.22}$$

$$\phi \to -\phi \,. \tag{1.23}$$

In this phase, the Dirac fermions become massive and the spectrum develops a gap above a two-fold degenerate ground state, which corresponds to the two configurations of the commensurate charge-density-wave.

Conversely, for $s > s_c$, the tuning parameter s flows to infinity while g_{Y} and λ flow to zero. Hence, the fermions decouple from the bosonic field, and in the low-energy limit, the theory describes the semi-metallic state of massless Dirac fermions. The effective theory of this Dirac fixed point is characterized by the non-interacting Lagrangian,

$$\mathcal{L}_{\mathrm{D}} = -\overline{\Psi}^j \not{\partial} \Psi^j . \tag{1.24}$$

Due to the absence of fermionic interactions, this Lagrangian is exactly solvable.

Chapter 2

Quantum Monte Carlo for two-dimensional fermion systems

When studying interacting many-body fermionic systems in equilibrium, one is generally interested in their collective properties, which are best described in the framework of statistical mechanics. Our goal is therefore to calculate quantities which are related to the statistical description like the (grand-)partition function as well as thermodynamic averages and correlation functions.

In the following I will outline generalizations of the Monte Carlo method suitable for simulating fermionic lattice models. The resulting quantum Monte Carlo (QMC) method introduces the imaginary time axis as an additional dimension into the classical Monte Carlo method. Many different QMC formulations exist and are used extensively in condensed matter physics. I will focus on the continuous time interaction expansion method (CT-INT) introduced by Rubtsov et al. [13], the finite temperature auxiliary field method (determinantal QMC / DQMC) introduced by Blankenbecler, Scalapino and Sugar (BSS) [14–16], as well as the linear continuous time interaction expansion method (LCT-INT) introduced by Iazzi et al [17, 18]. The latter two methods can be formulated in a projective scheme at zero temperature.

2.1 Monte Carlo for the classical Ising model

Let us briefly review the basic techniques of Monte Carlo for classical systems by considering the seminal Ising model. In dimensions $d \geq 2$ the Ising model features a ferromagnetic phase below T_c and a paramagnetic phase above T_c, while at the critical temperature T_c the system undergoes a second order phase transition induced by the spontaneous breaking of the global

Z_2 spin symmetry. The classical Hamiltonian function is given by

$$H = -J \sum_{\langle \boldsymbol{i},\boldsymbol{j} \rangle} \sigma_{\boldsymbol{i}}^z \sigma_{\boldsymbol{j}}^z, \tag{2.1}$$

where $\sigma_{\boldsymbol{i}}^z = \pm 1$ denotes a classical spin variable placed on a lattice at position $\boldsymbol{R_i}$. For a system of N_s spins one can define a configurations $C = |\sigma_{\boldsymbol{1}}^z, \sigma_{\boldsymbol{2}}^z, ..., \sigma_{\boldsymbol{N_s}}^z\rangle$, each of which contribute with a weight factor $p(C) = e^{-E(C)/kT}$ to the canonical partition function at temperature T, such that

$$Z = \sum_{\{C\}} e^{-E(C)/kT}. \tag{2.2}$$

Clearly not all configurations are equally important, because configurations with $E(C) \gg kT$ have exponentially suppressed weight factors. This leads to the idea of importance sampling: One interprets the weight of a configuration as the occurrence probability in a random walk through configuration space. If the weight factors can be calculated for all possible configurations, the partition function can be constructed from the simulated random walk. A widely used implementation of such a scheme is the Metropolis algorithm [19], in which one jumps from configuration $C \to C'$ if

$$q < \frac{p(C')}{p(C)} = \exp\left(-\Delta E/kT\right) \tag{2.3}$$

with $\Delta E = E\left(C'\right) - E\left(C\right)$ and q is a uniformly drawn random number $q \in [0, 1]$. After a warm up phase, the configurations drawn according to the Boltzmann distribution as it appears in the canonical partition function. Measurements of thermodynamic observables are taken after a sufficient number of updates has effectively decorrelated the configurations. Given an observable A, repeated measurements provide a statistical estimator

$$\bar{A} = \frac{1}{N_m} \sum_{i=1}^{N_m} A(C_i). \tag{2.4}$$

The statistical uncertainty of the estimator scales inversely with the square root of the number of measurements N_m,

$$\sigma_{\bar{A}} \sim \frac{1}{\sqrt{N_m}}. \tag{2.5}$$

What we have ultimately achieved is the calculation of thermodynamic observables with fixed statistical uncertainty in polynomial time. This computational scaling is a substantial

improvement over the exact formula, which is intractable for all but the smallest lattices due to the exponentially large space of configurations.

2.2 Decomposition of the quantum partition function

To quantify the effects of quantum mechanical fluctuations and detect possible ordering tendencies of the system, we need to calculate quantum mechanical averages such as

$$\langle \hat{O} \rangle_{GS} = \frac{\langle \Psi_0 | \hat{O} | \Psi_0 \rangle}{\langle \Psi_0 | \Psi_0 \rangle}, \tag{2.6}$$

$$\langle \hat{O} \rangle = \frac{\mathrm{Tr}\left[e^{-\beta \hat{H}} \hat{O} \right]}{\mathrm{Tr}\left[e^{-\beta \hat{H}} \right]} \text{ or} \tag{2.7}$$

$$C_{AB}(\tau) = \langle \hat{A}(\tau) \hat{B} \rangle, \tag{2.8}$$

either in the ground state or at a finite inverse temperature $\beta = \frac{1}{kT}$. Concrete examples are the magnetic structure factor

$$S(\boldsymbol{q}) = \frac{1}{N_s} \sum_{\boldsymbol{i},\boldsymbol{j}} e^{i\boldsymbol{q}\cdot(\boldsymbol{i}-\boldsymbol{j})} \langle \hat{\boldsymbol{S}}_{\boldsymbol{i}} \cdot \hat{\boldsymbol{S}}_{\boldsymbol{j}} \rangle, \tag{2.9}$$

which is peaked in the presence of magnetic order at the ordering vector $\boldsymbol{q}$, or the staggered density-density structure factor

$$D(\boldsymbol{q}) = \frac{1}{N_s} \sum_{\boldsymbol{i},\boldsymbol{j}} e^{i\boldsymbol{q}\cdot(\boldsymbol{i}-\boldsymbol{j})} \langle (\hat{n}_{\boldsymbol{i},A} - \hat{n}_{\boldsymbol{i},B}) (\hat{n}_{\boldsymbol{j},A} - \hat{n}_{\boldsymbol{j},B}) \rangle, \tag{2.10}$$

which detects charge order with ordering vector $\boldsymbol{q}$.

The numerical evaluation of expectation values for a given Hamiltonian is tied to its quantum partition partition function. The working principle of QMC is to decompose individual terms of the quantum partition function into a sum of configurations distributed according to the weight function $p(C)$

$$Z = \mathrm{Tr}\left[e^{-\beta \hat{H}} \right] = \sum_{\{C\}} p(C), \tag{2.11}$$

after which one can proceed using the classical Metropolis algorithm. Of course the decomposition in Eq. (2.11) is not uniquely defined and heavily basis dependent. Various QMC methods are build around different implementations of Eq. (2.11) using a particular decomposition of the quantum partition function.

In the following sections I will discuss the details of three related QMC methods suitable for simulations of fermionic lattice systems:

- **CT-INT**

  The continuous time interaction expansion (CT-INT) method was originally developed by Rubtsov et al. [13]. It is based on a formal series expansion in the interaction, and in contrast to regular perturbation theory the expansion is numerically exact and not limited to the small coupling regime. As its name suggests, the expansion is formulated in continuous time without discretization error. The CT-INT method is capable of simulating Hamiltonians with a general non-local and time-dependent fermionic interaction at finite temperature. The method is most commonly used in dynamical mean field theory (DMFT) where it serves as a general purpose impurity solver.

- **BSS**

  The BSS method was first introduced by Blankenbecler, Scalapino and Sugar (BSS)[14–16]. It is also referred to as auxiliary field method or determinantal QMC (DQMC). One first uses a Trotter-Suzuki decomposition [20, 21] to decouple the single-body Hamiltonian from the two-body interaction Hamiltonian in the trace of the partition function. In contrast to the CT-INT method one then introduces auxiliary scalar field variables at fixed time steps to decouple the four-fermion interaction term and integrate out the fermionic degrees of freedom.

- **LCT-INT**

  The linear continuous time interaction expansion method was introduced by Iazzi et al. [17, 18]. Its numerical implementation is based on the Green function representation of the BSS method, however it does not rely on the Trotter-Suzuki decomposition with finite time steps. Rather, one employs an interaction expansion in spirit similar to CT-INT to deal with the fermionic interaction in continuous time.

2.2.1 Continuous time interaction expansion (CT-INT)

Let us start our discussion with a general model Hamiltonian, which consists of a one-body part H_0 and a general two-body interaction H_I,

$$H = H_0 + H_I \tag{2.12}$$

$$H_0 = \sum_{ij} K_{ij} c_i^\dagger c_j \tag{2.13}$$

$$H_I = \sum_{ijkl} V_{ijkl}\, c_i^\dagger c_j^\dagger c_l c_k. \tag{2.14}$$

We want to describe the system in thermal equilibrium defined by the canonical ensemble at temperature T. To find an appropriate configuration space it is helpful to begin the derivation with the following calculation. Note that the τ-dependence of operators is to be understood as the imaginary time evolution within the Matsubara formalism, and is taken with respect to the free Hamiltonian $\hat{O}(\tau) = e^{H_0\tau}\hat{O}e^{-H_0\tau}$. In this context $\beta = \frac{1}{kT}$ denotes the inverse temperature.

$$A(\beta) \coloneqq e^{\beta H_0} e^{-\beta H} \tag{2.15}$$

$$\begin{aligned} \frac{dA}{d\beta} &= e^{\beta H_0}(H_0 - H)e^{-\beta H} \\ &= -e^{\beta H_0} H_I e^{-\beta H_0} A(\beta) \\ &= -H_I(\beta) A(\beta) \end{aligned} \tag{2.16}$$

$$\Rightarrow A(\beta) = \mathcal{T}_\tau e^{-\int_0^\beta H_I(\tau) d\tau} \tag{2.17}$$

With this intermediate result, the partition function can be rewritten in terms of averages, which are taken with respect to the free Hamiltonian H_0 (denoted by $\langle \dots \rangle_0 \coloneqq \mathcal{T}_\tau \operatorname{Tr}\left[e^{-\beta H_0} \dots\right] / Z_0$).

$$\begin{aligned} Z &= \operatorname{Tr}\left[e^{-\beta H}\right] \\ &= \operatorname{Tr}\left[e^{-\beta H_0} A(\beta)\right] \\ &= \operatorname{Tr}\left[e^{-\beta H_0} \mathcal{T}_\tau e^{-\int_0^\beta H_I(\tau) d\tau}\right] \\ &= \sum_{k=0}^{\infty} \int_0^\beta d\tau_1 \cdots \int_{\tau_{k-1}}^\beta d\tau_k \operatorname{Tr}\left[e^{-\beta H_0} e^{\tau_k H_0}(-H_I) \dots e^{-(\tau_2 - \tau_1) H_0}(-H_I) e^{-\tau_1 H_0}\right] \\ &= Z_0 \sum_{k=0}^{\infty} \frac{(-1)^k}{k!} \int_0^\beta d\tau_1 \cdots \int_0^\beta d\tau_k \langle H_I(\tau_1) \dots H_I(\tau_k)\rangle_0 \end{aligned} \tag{2.18}$$

Note that the grand canonical partition function is used here, as the term $-\mu N$ can be included into H_0 (or set to zero in case of half filling). In terms of Feynman diagrams, this expansion equals a sum over all diagrams including closed diagrams, and all expansion orders. One can further decompose the interaction part of the Hamiltonian into a sum of operators that are enumerated by a multi-index $x = (i, j, k, l)$, such that

$$h(x, \tau) = V_{ijkl}\, e^{\tau H_0} c_i^\dagger c_j^\dagger c_l c_k e^{-\tau H_0} \tag{2.19}$$

$$H_I = \sum_x h(x, 0). \tag{2.20}$$

The partition function can then be expressed as the sum over all configurations $\mathcal{C} = \{(x_1, \tau_1), \ldots, (x_k, \tau_k)\}$ of interaction vertices $\{h(x, \tau)\}$, such that

$$\begin{aligned} Z/Z_0 &= \sum_{k=0}^{\infty} \int_0^\beta d\tau_1 \cdots \int_{\tau_{k-1}}^\beta d\tau_k \sum_{x_1} \cdots \sum_{x_k} (-1)^k \operatorname{Tr}\left[e^{-\beta H_0} \prod_{n=1}^{k} h(x_n, \tau_n) \right] / Z_0 \\ &= \sum_{k=0}^{\infty} \int_0^\beta d\tau_1 \cdots \int_0^\beta d\tau_k \sum_{x_1} \cdots \sum_{x_k} \frac{(-1)^k}{k!} \langle h(x_1, \tau_1) \ldots h(x_k, \tau_k) \rangle_0 \\ &= \sum_{\mathcal{C}} w(\mathcal{C}). \end{aligned} \tag{2.21}$$

Here we introduced the configuration weight

$$w(\mathcal{C}) = (-1)^k \langle h(x_1, \tau_1) \ldots h(x_k, \tau_k) \rangle_0. \tag{2.22}$$

The Monte Carlo simulation aims to perform importance sampling on the configuration space using the weight function $w(\mathcal{C})$. Note that in Eq. (2.21) the configuration $\mathcal{C}$ is interpreted as an unordered set of vertices, which cancels the factor $\frac{1}{k!}$ in Eq. (2.22).

Because of the explicit expansion in the interaction CT-INT is also referred to as a weak-coupling expansion. It should be noted that the interaction expansion is only of a formal nature and all perturbation orders are sampled over. In fermionic systems on a finite lattice the degrees of freedoms are bounded by the size of the Hilbert space. The distribution function of the perturbation order k has a maximum at $k_{\text{max}} < \infty$ and perturbations orders $|k - k_{\text{max}}| \gg 1$ are exponentially suppressed. It is therefore not necessary to restrict k by imposing a cutoff on the perturbation order to ensure convergence.

Spinless fermions on honeycomb lattice

Let us now return to the $t - V$ model of spinless fermions on a honeycomb lattice (cf. section 1.3), and consider its implementation in CT-INT [22]. Following Eq. (2.20), we find

the decomposition

$$\begin{aligned} h(x_k, \tau_k) &= V \left(n_{i_{2k-1}}(\tau_k) - \frac{1}{2} \right) \left(n_{i_{2k}}(\tau_k) - \frac{1}{2} \right) \\ x_k &= (i_{2k-1}, i_{2k}) \in \langle i, j \rangle, \end{aligned} \tag{2.23}$$

from which we can derive the configuration weight as

$$\begin{aligned} w(\mathcal{C}) =& (-V)^k \left\langle \left(n_{i_1}(\tau_1) - \frac{1}{2} \right) \left(n_{i_2}(\tau_2) - \frac{1}{2} \right) \cdots \times \right. \\ & \left. \left(n_{i_{2k-1}}(\tau_{2k-1}) - \frac{1}{2} \right) \left(n_{i_{2k}}(\tau_{2k}) - \frac{1}{2} \right) \right\rangle_0 \\ =& (-V)^k \det(G^k), \end{aligned} \tag{2.24}$$

where Wick's theorem is used to express the expectation value as the determinant of the propagator matrix (or Green's function matrix), which is given by[1]

$$G^k_{pq} = G^0_{i_p i_q}(\tau_p - \tau_q) - \frac{\delta_{pq}}{2} \tag{2.25}$$

and can be written explicitly as a $2k \times 2k$ matrix

$$G^k = \begin{pmatrix} G^0_{i_1 i_1}(0^+) - \frac{1}{2} & G^0_{i_1 i_2}(0^+) & \dots & G^0_{i_1 i_{2k-1}}(\tau_1 - \tau_{2k-1}) & G^0_{i_1 i_{2k}}(\tau_1 - \tau_{2k}) \\ G^0_{i_2 i_1}(0^-) & G^0_{i_2 i_2}(0^+) - \frac{1}{2} & \dots & G^0_{i_2 i_{2k-1}}(\tau_2 - \tau_{2k-1}) & G^0_{i_2 i_{2k}}(\tau_2 - \tau_{2k}) \\ \vdots & \vdots & \ddots & \vdots & \vdots \\ G^0_{i_{2k-1} i_1}(\tau_{2k-1} - \tau_1) & G^0_{i_{2k-1} i_2}(\tau_{2k-1} - \tau_2) & \dots & G^0_{i_{2k-1} i_{2k-1}}(0^+) - \frac{1}{2} & G^0_{i_{2k-1} i_{2k}}(0^+) \\ G^0_{i_{2k} i_1}(\tau_{2k} - \tau_1) & G^0_{i_{2k} i_2}(\tau_{2k} - \tau_2) & \dots & G^0_{i_{2k} i_{2k-1}}(0^-) & G^0_{i_{2k} i_{2k}}(0^+) - \frac{1}{2} \end{pmatrix}.$$

Here $G^0_{ij}(\tau) = \langle c_i(\tau) c^\dagger_j \rangle_0$ is the non-interacting Green's function and is given by

$$G^0_{ij}(\tau > 0) = \left(\frac{e^{K\tau}}{1 + e^{\beta K}} \right)_{ij} \tag{2.26}$$

$$G^0_{ij}(\tau < 0) = -\left(\frac{e^{K(-\tau+\beta)}}{1 + e^{\beta K}} \right)_{ij} = -\eta_i \eta_j G^0_{ij}(\tau > 0) \tag{2.27}$$

[1] Note that the indices p, q refer to the p-th row and q-th column of G^k, while i_p, i_q denote the vertices associated to p, q.

with the hopping matrix K

$$K_{ij} = \begin{cases} -t, & (i,j) \in \langle i,j \rangle \\ 0, & \text{otherwise} \end{cases}, \tag{2.28}$$

and the sublattice sign factor η (A and B denote the two sublattices of the honeycomb lattice respectively)

$$\eta_i = \begin{cases} 1, & i \in A \\ -1, & i \in B \end{cases}. \tag{2.29}$$

In the case of particle-hole symmetry one finds $G^0_{ii}(\tau = 0^+) = \frac{1}{2}$, and the diagonal elements of G^k vanish. The full Green's function matrix inherits property (2.27) of the free Green's function

$$G^k_{pq} = -\eta_{i_p}\eta_{i_q} G^k_{qp}. \tag{2.30}$$

In fact, this symmetry property can be used to lift the sign problem for the $t - V$ model. However, because it relies directly on particle-hole symmetry, it no longer prevents a sign problem beyond half-filling [23].

2.2.2 Finite temperature auxiliary field expansion (BSS)

The key ingredient of the Monte Carlo algorithm by BSS is the introduction of auxilliary fields through a discrete Hubbard-Stratonovitch tranformation. This decouples the fermion interaction, such that the effective action $S[\phi(i,\tau)]$ becomes non-interacting,

$$\mathrm{Tr}\left[e^{-\beta H}\right] = \int d\Phi(i,\tau)\; e^{-S[\phi(i,\tau)]}, \tag{2.31}$$

where i sums over lattice sites and $\tau \in [0,\beta]$. The basic idea is then to sample over all field configurations by expressing their statistical weight in terms of Green functions, which conveniently also allows us to directly extract physical observables via the Wick theorem.

Let us now work out the decomposition of the partition function for the $t - V$ model in more detail. We follow the notation introduced in Eqs. (2.13). The first step is to perform a Trotter decomposition to separate the single particle from the two particle interaction term in

the Hamiltonian

$$Z = \mathrm{Tr}\left[e^{-\beta H}\right] = \mathrm{Tr}\left[\left(e^{-\Delta_\tau H_0} e^{-\Delta_\tau H_I}\right)^m\right] + \mathcal{O}(\Delta_\tau^2), \tag{2.32}$$

which introduces the Trotter error Δ_τ with $m\Delta_\tau = \beta$. In principle, the Trotter error can be decreased by an order of magnitude by using the symmetric Trotter decomposition up to second order [24, 25]

$$e^{-\beta H} = e^{\frac{-\Delta_\tau H_0}{2}} e^{-\Delta_\tau H_I} e^{-\frac{\Delta_\tau}{2} H_0} + \mathcal{O}(\Delta_\tau^3). \tag{2.33}$$

The symmetric Trotter decomposition is commonly used if the interaction can be decomposed into

$$H_I = \sum_i^{N_s} u(i), \tag{2.34}$$

such that the terms $[u(i), u(j)] = 0$ commute. This is the case for the Hubbard model with onsite interaction, however for the $t - V$ model, the interaction can only be decomposed into

$$\begin{aligned} H_I &= V \sum_{b=1}^{N_b} \sum_{\langle ij \rangle_b} \left(n_i - \frac{1}{2}\right)\left(n_j - \frac{1}{2}\right) \\ &= \sum_{b=1}^{N_b} \sum_{\langle ij \rangle_b} u_b(i,j) \end{aligned} \tag{2.35}$$

where the index b classifies the type of nearest neighbor bond and $[u_b(i,j), u_{b'}(i,j)] = \text{const} \times \delta_{bb'}$. This generalization becomes necessary because the local density-density interaction in the $t - V$ model involves $N_b = 3$ neighboring bonds for each lattice site. For this reason, the symmetric Trotter formula would lead to the more complicated decomposition

$$\begin{aligned} e^{-\beta H} =& e^{-\frac{\Delta_\tau}{2} H_0} e^{-\frac{\Delta_\tau}{2} \sum_{\langle ij \rangle_1} u_1} e^{-\frac{\Delta_\tau}{2} \sum_{\langle ij \rangle_2} u_2} e^{-\Delta_\tau \sum_{\langle ij \rangle_3} u_3} \\ & e^{-\frac{\Delta_\tau}{2} \sum_{\langle ij \rangle_2} u_2} e^{-\frac{\Delta_\tau}{2} \sum_{\langle ij \rangle_1} u_1} e^{-\frac{\Delta_\tau}{2} H_0} + \mathcal{O}(\Delta_\tau^3), \end{aligned} \tag{2.36}$$

which greatly complicates the update scheme of the auxilliary fields. Instead we choose to keep terms up to first order in Δ_τ,

$$e^{-\Delta_\tau (H_0 + H_I)} = e^{-\Delta_\tau H_0} e^{-\Delta_\tau H_I} + \mathcal{O}(\Delta_\tau^2), \tag{2.37}$$

After the Trotter decomposition, the next step is the usage of a discrete Hubbard-Stratonovich transformation

$$\begin{aligned} e^{-\Delta_\tau \sum_{\langle i,j\rangle_b} u_b(i,j)} &= e^{-\Delta_\tau V \sum_{\langle i,j\rangle_b} \left(n_i - \frac{1}{2}\right)\left(n_j - \frac{1}{2}\right)} \\ &= e^{-\frac{\Delta_\tau V}{2} \sum_{\langle i,j\rangle_b} \left[\left(c_i^\dagger c_j + c_j^\dagger c_i\right)^2 - \frac{1}{2}\right]} \\ &= \frac{1}{2} e^{-\frac{\Delta_\tau V}{2}} \sum_{\{s_{ij}=\pm 1\}} \exp\left(-\sum_{\langle i,j\rangle_b} \lambda s_{ij}\left(c_i^\dagger c_j + c_j^\dagger c_i\right)\right), \end{aligned} \tag{2.38}$$

with $\cosh(\lambda) = e^{\frac{\Delta_\tau V}{2}}$. This transformation introduces independent auxiliary fields $s_{ij} = \pm 1$ for each time slice and lattice bond $(i,j) \in \langle i,j\rangle_b$. The free fermion terms can now be expressed in terms of K and V, which are $N_s \times N_s$ matrices in the single particle basis,

$$-t \sum_{\langle i,j\rangle_b} \left(c_i^\dagger c_j + c_j^\dagger c_i\right) = \sum_{i,j} c_i^\dagger (K_b)_{i,j} c_j = \boldsymbol{c}^\dagger K_b \boldsymbol{c} \tag{2.39}$$

$$-\sum_{\langle i,j\rangle_b} \lambda s_{ij}\left(c_i^\dagger c_j + c_j^\dagger c_i\right) = \sum_{i,j} c_i^\dagger (V_b)_{i,j} c_j = \boldsymbol{c}^\dagger V_b(\boldsymbol{s}) \boldsymbol{c}. \tag{2.40}$$

We further introduce the imaginary time propagators between discrete time steps $n_i \Delta_\tau = \tau_i$

$$U_{\boldsymbol{s}}(\tau_2, \tau_1) = \prod_{n=n_1+1}^{n_2} \prod_{b=1}^{N_b} e^{-\Delta_\tau \boldsymbol{c}^\dagger K_b \boldsymbol{c} + \boldsymbol{c}^\dagger V_b(\boldsymbol{s}_b^n)\boldsymbol{c}} \tag{2.41}$$

$$B_{\boldsymbol{s}}(\tau_2, \tau_1) = \prod_{n=n_1+1}^{n_2} \prod_{b=1}^{N_b} e^{-\Delta_\tau K_b + V_b(\boldsymbol{s}_b^n)}, \tag{2.42}$$

such that we are now ready to trace out the fermionic operators. We finally obtain determinants as the configuration weights

$$\begin{aligned} Z &= C^m \sum_{\{\boldsymbol{s}\}} \mathrm{Tr}\left[U_{\boldsymbol{s}}(\beta, 0)\right] \\ &= C^m \sum_{\{\boldsymbol{s}\}} \det\left[1 + B_{\boldsymbol{s}}(\beta, 0)\right] \\ &= \sum_{\mathcal{C}} w(\mathcal{C}). \end{aligned} \tag{2.43}$$

Green function

The expectation value of general observables can be expressed as a weighted sum of their Monte Carlo estimators,

$$\begin{aligned}\langle O\rangle &= \frac{\mathrm{Tr}[e^{-\beta H}O]}{\mathrm{Tr}[e^{-\beta H}]} \\ &= \sum_{\boldsymbol{s}} p(\boldsymbol{s})\langle O\rangle_{\boldsymbol{s}},\end{aligned} \tag{2.44}$$

where the statistical weight is

$$p(\boldsymbol{s}) = \frac{\det\left[1 + B_{\boldsymbol{s}}(\beta,0)\right]}{\sum_{\boldsymbol{s}'}\det\left[1 + B_{\boldsymbol{s}'}(\beta,0)\right]} \tag{2.45}$$

and the estimator is evaluated on a given configuration $\boldsymbol{s}$

$$\langle O\rangle_{\boldsymbol{s}} = \frac{\mathrm{Tr}\left[U_{\boldsymbol{s}}(\beta,\tau)OU_{\boldsymbol{s}}(\tau,0)\right]}{\sum_{\boldsymbol{s}'}\mathrm{Tr}\left[U_{\boldsymbol{s}'}(\beta,0)\right]}. \tag{2.46}$$

Furthermore, the fermionic operators in Eq. (2.46) can be traced out again, and we can use the propagators B_s to express the estimator as [24, 25]

$$\langle O\rangle_{\boldsymbol{s}} = \mathrm{Tr}\left[\left(1 - \left(1 + B_{\boldsymbol{s}}(\tau,0)B_{\boldsymbol{s}}(\beta,\tau)\right)^{-1}\right)O\right]. \tag{2.47}$$

We can now identify the representation of the single-particle Green function at equal times - for the time slice defined by τ - in terms of the propagators as

$$\begin{aligned}\left(G_{\boldsymbol{s}}(\tau,\tau)\right)_{ij} &= \langle c_i(\tau)c_j^\dagger(\tau)\rangle_{\boldsymbol{s}} \\ &= \left(1 + B_{\boldsymbol{s}}(\tau,0)B_{\boldsymbol{s}}(\beta,\tau)\right)^{-1}.\end{aligned} \tag{2.48}$$

Moreover, Eq. (2.48) can be generalized to the unequal time case

$$\begin{aligned}\left(G_{\boldsymbol{s}}(\tau_1,\tau_2)\right)_{ij} &= \mathcal{T}\langle c_i(\tau_1)c_j^\dagger(\tau_2)\rangle_{\boldsymbol{s}} \\ &= \begin{cases}\left(B_{\boldsymbol{s}}(\tau_1,\tau_2)G_{\boldsymbol{s}}(\tau_2,\tau_2)\right)_{ij}, \tau_1 > \tau_2 \\ -\left(\left(1 - G_{\boldsymbol{s}}(\tau_2,\tau_2)\right)B_{\boldsymbol{s}}^{-1}(\tau_2,\tau_1)\right)_{ij}, \tau_1 < \tau_2\end{cases}.\end{aligned} \tag{2.49}$$

2.2.3 Linear continuous time interaction expansion (LCT-INT)

The LCT-INT algorithm is comprised of a combination of both CT-INT and BSS. The initial decomposition of the partition function is based on the continuous interaction expansion,

which is identical to the starting point of the traditional CT-INT algorithm (notation is adopted from Sec. 2.2.1)

$$Z = \sum_{k=0}^{\infty} \int_0^\beta d\tau_1 \cdots \int_0^\beta d\tau_k \sum_{x_1} \cdots \sum_{x_k} \frac{(-1)^k}{k!} \operatorname{Tr}\left[e^{-\beta H_0} \prod_{n=1}^{k} h(x_n, \tau_n) \right]. \tag{2.50}$$

Instead of sampling Eq. 2.50 directly, one may introduce the imaginary time propagator in analogy to the BSS algorithm

$$U_{\mathcal{C}}(\tau, \tau') = e^{-\tau \boldsymbol{c}^\dagger K \boldsymbol{c}} \prod_{\tau \geq \tau_n \geq \tau'} \left[h(x_n, \tau_n) \right] e^{\tau' \boldsymbol{c}^\dagger K \boldsymbol{c}}, \tag{2.51}$$

which allows us to express the partition function as

$$Z = \sum_{k=0}^{\infty} \int_0^\beta d\tau_1 \cdots \int_0^\beta d\tau_k \sum_{x_1} \cdots \sum_{x_k} \frac{(-1)^k}{k!} \operatorname{Tr}\left[U_{\mathcal{C}}(\beta, 0) \right]. \tag{2.52}$$

At this point we cannot yet integrate out the fermions because of the remaining factors of $h(x_n, \tau_n)$, which still contain terms of the form $c^\dagger c^\dagger cc$. Let us now assume that the fermionic interaction terms are of the density-density type, as is the case for Hubbard-type lattice models. In this case the interaction can be expressed as exponentials of bilinear fermion operators using the identity

$$\hat{n}_i = \frac{1}{2} \left(1 - e^{i\pi \hat{n}_i} \right). \tag{2.53}$$

For the case of the aforementioned $t - V$ model we obtain [17]

$$H_I = \frac{V}{4} \sum_{\langle i,j \rangle} e^{i\pi(\hat{n}_i + \hat{n}_j)}. \tag{2.54}$$

In the following I will focus on this particular form of the interaction, although more general density-density can be handled by the algorithm. After inserting the identity of Eq. (2.54) into Eq. (2.52), we can integrate out the fermionic degrees of freedom using the Gaussian

integral identity,

$$\begin{aligned} Z &= \sum_{\mathcal{C}} (-1)^k \operatorname{Tr}\left[U_{\mathcal{C}}(\beta, 0)\right] \\ &= \sum_{\mathcal{C}} \left(\frac{-V}{4}\right)^k \det\left[1 + B_{\mathcal{C}}(\beta, 0)\right] \\ &= \sum_{\mathcal{C}} w(\mathcal{C}), \end{aligned} \tag{2.55}$$

where we have introduced the imaginary time propagator in matrix form

$$B_{\mathcal{C}}(\tau, \tau') = e^{-\tau K} \prod_{\tau \geq \tau_n \geq \tau'} \left[X(x_n, \tau_n)\right] e^{\tau' K}. \tag{2.56}$$

In analogy to the BSS algorithm we can express the equal-time Green function at time τ as

$$G_{\mathcal{C}}(\tau, \tau) = \left[1 + B_{\mathcal{C}}(\tau, 0) B_{\mathcal{C}}(\Theta, \tau)\right]^{-1}. \tag{2.57}$$

Here, $X(x_n, \tau_n)$ is a $N_s \times N_s$ matrix, and for the $t - V$ model its entries follow from Eq. (2.54). In the real space orbital basis we find

$$\left(X(x, 0)\right)_{mn} = \langle m | e^{i\pi(n_i + n_j)} | n \rangle \tag{2.58}$$

where the multi-index $x = (i, j) \in \langle i, j \rangle$ signifies a nearest neighbor bond. More explicitly, the matrix X is diagonal and its non-zero elements are

$$\left(X(x, 0)\right)_{mm} = \begin{cases} -1, \text{ for } m = i \text{ or } m = j \\ 1, \text{ otherwise} \end{cases}. \tag{2.59}$$

2.2.4 Zero temperature projection scheme

In addition to the finite temperature formulation, the BSS and LCT-INT algorithms can also directly access the ground state properties of the system with only slight modifications. This is achieved by calculating ground state expectation values through the projection of a trial wave function $|\Psi_T\rangle$ along the imaginary axis

$$\frac{\langle \Psi_0 | O | \Psi_0 \rangle}{\langle \Psi_0 | \Psi_0 \rangle} = \lim_{\Theta \to \infty} \frac{\langle \Psi_T | e^{-\Theta/2H} O e^{-\Theta/2H} | \Psi_T \rangle}{\langle \Psi_T | e^{-\Theta H} | \Psi_T \rangle}. \tag{2.60}$$

We require the wave function to be a Slater determinant such that we can express it through a matrix P

$$|\Psi_T\rangle = \prod_i^{N_p} \left(\boldsymbol{c}^\dagger P\right)_i |0\rangle. \tag{2.61}$$

Here the dimension of P is given by $N_s \times N_p$, where N_s is the number of sites and N_p is the number of particles. To avoid the sign-problem, the trial-wave function must be chosen as an eigenstate of the particle-hole operator. For the specific case of the $t-V$ model, I refer to section 4.5.3 for a detailed discussion of the construction of the trial-wave function including various symmetries.

We ultimately find a decomposition very similar to the finite temperature case

$$\langle\Psi_T|e^{-\Theta H}|\Psi_T\rangle = \sum_{\mathcal{C}} q(\mathcal{C}) \det\left[P^\dagger B_{\mathcal{C}}(\Theta,0)P\right], \tag{2.62}$$

from which the weight function follows as

$$w(\mathcal{C}) = q(\mathcal{C}) \det\left[P^\dagger B_{\mathcal{C}}(\Theta,0)P\right], \tag{2.63}$$

and the representation of the Green function reduces to

$$G_{\mathcal{C}}(\tau,\tau) = 1 - B_{\mathcal{C}}(\tau,0)P\left(P^\dagger B_{\mathcal{C}}(\Theta,0)P\right)^{-1} P^\dagger B_{\mathcal{C}}(\Theta,\tau). \tag{2.64}$$

Alternatively, one may decompose the Green function into three separate parts

$$1 - G_{\mathcal{C}}(\tau,\tau) = R_{\mathcal{C}} W_{\mathcal{C}} L_{\mathcal{C}}, \tag{2.65}$$

with

$$R_{\mathcal{C}} = B_{\mathcal{C}}(\tau,0)P \tag{2.66}$$

$$W_{\mathcal{C}} = \left(P^\dagger B_{\mathcal{C}}(\Theta,0)P\right)^{-1} \tag{2.67}$$

$$L_{\mathcal{C}} = P^\dagger B_{\mathcal{C}}(\Theta,\tau). \tag{2.68}$$

This representation is more efficient during the sampling process because of the reduced dimension of the $R_{\mathcal{C}}$ ($N_s \times N_p$), $W_{\mathcal{C}}$ ($N_p \times N_p$) and $L_{\mathcal{C}}$ ($N_p \times N_s$) matrices. However, the trade off is that for each measurement the Green function matrix is not in memory and has to be recomputed. In the following I will focus on the Green function representation for simplicity and consistency with the finite temperature formulation, and because translating

between Eqs. (2.64, 2.67) is possible without complication. Furthermore, all the following discussion of transition probabilities, updates and numerical stabilization can be formulated analogously for both the finite temperature scheme and zero temperature projection scheme.

2.3 Transition probabilities and update schemes

The goal so far has been to express the partition function as a sum of configuration weights

$$Z = \sum_{\mathcal{C}} w(\mathcal{C}) \tag{2.69}$$

such that one may use Monte Carlo methods to perform importance sampling. The most important pitfall of such quantum Monte Carlo schemes concerns the positivity of all configuration weights $w(\mathcal{C})$, which in its form (Eq. 2.22) cannot be guaranteed for general models. At this point we assume all weights to be positive and postpone the discussion of the *sign problem* to section 2.7. In this section we focus on basic Monte Carlo updates that constitute the random walk through configuration space.

The goal is to generate configurations according to their statistical weight $w(\mathcal{C})$ with which they contribute to the partition function. This can be achieved by drawing configurations along a Markov chain

$$\mathcal{C}_0 \to \mathcal{C}_1 \to \mathcal{C}_2 \to \mathcal{C}_3 \to \dots \tag{2.70}$$

where we start at an initial configuration $\mathcal{C}_0$ and generate the new configuration based on the previous one. Formally the Markov chain is defined by the transition matrix $T(\mathcal{C} \to \mathcal{C}')$ which indicates the transition probability to go from configuration $\mathcal{C}$ to configuration $\mathcal{C}'$. The elements of the transition matrix are chosen such that the frequency of generated configurations reproduce the normalized probability density function of the partition function

$$p(\mathcal{C}) = \frac{w(\mathcal{C})}{Z}. \tag{2.71}$$

The Markovian process succeeds under the following conditions:

- **Ergodicity:** It must be possible to reach any configuration $\mathcal{C}'$ from any other configuration $\mathcal{C}$ in a finite number of steps.

- **Normalization:** For each configuration the transition probabilities must be normalized

$$\sum_{C' \in \{\mathcal{C}\}} T(\mathcal{C} \to \mathcal{C}') = 1. \tag{2.72}$$

- **Stationary Distribution:** One possible solution to obtain a stationary distribution is the detailed balance condition:

$$\frac{T(\mathcal{C} \to \mathcal{C}')}{T(\mathcal{C}' \to \mathcal{C})} = \frac{p(\mathcal{C}')}{p(\mathcal{C})} \tag{2.73}$$

To find a solution to $T(\mathcal{C} \to \mathcal{C}')$ that fulfills these properties one can use the Metropolis algorithm. The next element in the Markov chain is proposed with probability $P(\mathcal{C} \to \mathcal{C}')$ and accepted with probability $A(\mathcal{C} \to \mathcal{C}')$, such that the transition probability factorizes,

$$T(\mathcal{C} \to \mathcal{C}') = P(\mathcal{C} \to \mathcal{C}') \cdot A(\mathcal{C} \to \mathcal{C}'). \tag{2.74}$$

The acceptance probability in the Metropolis algorithm is then given by

$$A(\mathcal{C} \to \mathcal{C}') = \min\left(1, \frac{P(\mathcal{C}' \to \mathcal{C})\, p(\mathcal{C}')}{P(\mathcal{C} \to \mathcal{C}')\, p(\mathcal{C})}\right) \tag{2.75}$$

2.3.1 Interaction vertex representation in CT-INT

Transition probabilities

To sample over the set of all CT-INT vertex configurations $\{C_k\}$ with

$$C_k = \{x_1, \ldots, x_k\}, \tag{2.76}$$

it is apparent that one requires vertex addition and removal updates. These two kind of updates are already sufficient to guarantee ergodicity as long as vertices with all possible values of the multi-index x_n are accounted for. From every configuration one could remove all vertices and build up any other arbitrary configuration from scratch by inserting back the new vertices. Vertex addition/removal updates therefore make up the backbone of CTQMC simulations.

First consider the fact that the proposal probability can be split into two parts

$$P(\mathcal{C} \to \mathcal{C}') = a \cdot b(\mathcal{C} \to \mathcal{C}') \tag{2.77}$$

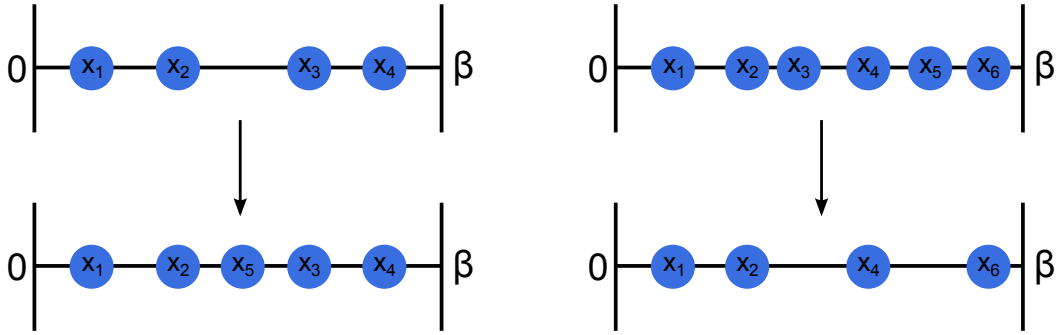

(a) Vertex addition (b) Vertex removal

Figure 2.1: Illustration of basic vertex addition and removal updates. The blue dots contain the information of each vertex (e.g. the interaction bond) and the associated imaginary time $\tau_i \in [0, \beta)$.

where a is an arbitrary a priori proposal probability that determines the frequency of the update in the Monte Carlo simulation and $b(\mathcal{C} \to \mathcal{C}')$ is the probability to select specific vertices for the update. To illustrate this point, we shall work out the respective transition probabilities for the spinless fermion model.

Vertex addition

Vertex addition updates describe updates between the configurations

$$\mathcal{C}_k = \{x_1, \ldots, x_k\} \tag{2.78}$$

$$\mathcal{C}_{k+n} = \{x_1, \ldots, x_k\} \cup \{x_{k+1}, \ldots, x_{k+n}\} \tag{2.79}$$

where n is the number of added vertices. The selection probability $b(\mathcal{C}_{k+n} \to \mathcal{C}_k)$ is given by the probability to select n vertices out of $k+n$ vertices for removal

$$b\left(\mathcal{C}_{k+n} \to \mathcal{C}_k\right) = 1/\binom{k+n}{n}. \tag{2.80}$$

Conversely, we have

$$b\left(\mathcal{C}_k \to \mathcal{C}_{k+n}\right) = n! \frac{\prod_{i=k+1}^{k+n} d\tau_i}{(\beta N_b)^n} \tag{2.81}$$

where $\frac{d\tau}{\beta}$ is the infinitesimal probability to pick a specific imaginary time τ and $\frac{1}{N_b}$ is the probability to place the vertex on a certain bond.[2] Since the vertices in each configuration

[2] $N_b = 3L^2$ is the number of bonds on the honeycomb lattice.

are unordered, the factor $n!$ accounts for the number of permutations that lead to the same configuration. Combining Eq. (2.80), (2.81), (2.77), (2.75), (2.71) and (2.24) we obtain

$$\begin{aligned} A(\mathcal{C}_k \to \mathcal{C}_{k+n}) &= \min\left(1, \frac{a_{\text{rem}}^n}{a_{\text{add}}^n}(\beta N_b)^n \frac{k!}{(k+n)!}\frac{w(\mathcal{C}_{k+n})}{w(\mathcal{C}_k)}\right) \\ &= \min\left(1, \frac{a_{\text{rem}}^n}{a_{\text{add}}^n}(-V\beta N_b)^n \frac{k!}{(k+n)!}\frac{\det(G^{k+n})}{\det(G^k)}\right) \end{aligned} \tag{2.82}$$

where all infinitesimal integration factors as well as the normalization do in fact cancel out.

Vertex removal

Vertex removal updates are similar to vertex addition updates in the sense that they are complementary to each other. They involve configurations

$$\mathcal{C}_k = \{x_1, \ldots, x_k\} \tag{2.83}$$

$$\mathcal{C}_{k-n} = \{x_1, \ldots, x_k\} \backslash \{x_{k-n}, \ldots, x_k\} \tag{2.84}$$

and their acceptance probabilities are given by

$$\begin{aligned} A(\mathcal{C}_k \to \mathcal{C}_{k-n}) &= \min\left(1, \frac{a_{\text{add}}^n}{a_{\text{rem}}^n}\frac{1}{(\beta N_b)^n}\frac{k!}{(k-n)!}\frac{w(\mathcal{C}_{k-n})}{w(\mathcal{C}_k)}\right) \\ &= \min\left(1, \frac{a_{\text{add}}^n}{a_{\text{rem}}^n}\frac{1}{(-V\beta N_b)^n}\frac{k!}{(k-n)!}\frac{\det(G^{k-n})}{\det(G^k)}\right) \end{aligned} \tag{2.85}$$

From a computational point of view calculating the ratio of two determinants is very expansive and scales as $\mathcal{O}(k^3)$. Fortunately, one can use the fact that during the update process comparatively only a few rows and columns of G^k change to construct *fast updates rules*, which only scale as $\mathcal{O}(k^2)$. They are dealt with in section 2.5.

2.3.2 Green function representation in BSS

Auxiliary field updates

For the BSS algorithm, the configuration space is given by the set of all possible auxiliary field configurations on all time slices

$$\mathcal{C}_{\boldsymbol{s}} = \{s_1, \ldots, s_m\}. \tag{2.86}$$

To update a given configuration, we can propose to flip the auxiliary field on a particular time slice. To keep the detailed balance condition, we accept this move with the probability

$$R = \min\left(\frac{p(\boldsymbol{s'})}{p(\boldsymbol{s})}\right) = \min\left(\frac{w(\mathcal{C}')}{w(\mathcal{C})}\right). \tag{2.87}$$

In the simplest case, we only update a single auxiliary field. The new configuration is then identical to the previous one, except at bond $\boldsymbol{i} \in \langle i, j\rangle_b$ and time slice n ($\tau = \Delta_\tau n$), such that

$$s'_{\boldsymbol{j},m} = \begin{cases} s_{\boldsymbol{j},m} \text{ if } \boldsymbol{i} \neq \boldsymbol{j} \text{ or } n \neq m \\ -s_{\boldsymbol{j},m} \text{ if } \boldsymbol{i} = \boldsymbol{j} \text{ and } n = m \end{cases}. \tag{2.88}$$

The acceptance probability for a single auxiliary field flip can be computed from the old Green function for both the finite temperature and projective case. To derive this, we rewrite the modified interaction term in terms of the unchanged auxiliary field, such that

$$\begin{aligned} \Delta &= \left(e^{V(\boldsymbol{s}'_n)} e^{-V(\boldsymbol{s}_n)} - 1\right) \\ \Leftrightarrow e^{V(\boldsymbol{s}'_n)} &= (1+\Delta)\, e^{V(\boldsymbol{s}_n)}. \end{aligned} \tag{2.89}$$

For the finite temperature case we then obtain the acceptance probability as [24, 25]

$$\begin{aligned} R &= \frac{\det\left[1 + B_{\boldsymbol{s}'}(\beta, 0)\right]}{\det\left[1 + B_{\boldsymbol{s}}(\beta, 0)\right]} \\ &= \frac{\det\left[1 + B_{\boldsymbol{s}}(\beta, \tau)(1+\Delta)B_{\boldsymbol{s}}(\tau, 0)\right]}{\det\left[1 + B_{\boldsymbol{s}}(\beta, 0)\right]} \\ &= \det\left[1 + \Delta B_{\boldsymbol{s}}(\tau, 0)(1 + B_{\boldsymbol{s}}(\tau, 0))^{-1} B_{\boldsymbol{s}}(\beta, \tau)\right] \\ &= \det\left[1 + \Delta(1 - (1 + B_{\boldsymbol{s}}(\tau, 0) B_{\boldsymbol{s}}(\beta, \tau))^{-1})\right] \\ &= \det\left[1 + \Delta(1 - G_{\boldsymbol{s}}(\tau, \tau))\right], \end{aligned} \tag{2.90}$$

and in the projective case

$$\begin{aligned} R &= \frac{\det\left[P^\dagger B_{s'}(\Theta,0)P\right]}{\det\left[P^\dagger B_s(\Theta,0)P\right]} \\ &= \frac{\det\left[P^\dagger B_s(\Theta,\tau)(1+\Delta)B_s(\tau,0)P\right]}{\det\left[P^\dagger B_s(\Theta,0)P\right]} \\ &= \det\left[P^\dagger B_s(\Theta,\tau)(1+\Delta)B_s(\tau,0)P\left(P^\dagger B_s(\Theta,0)P\right)^{-1}\right] \\ &= \det\left[1+P^\dagger B_s(\Theta,\tau)\Delta B_s(\tau,0)P\left(P^\dagger B_s(\Theta,0)P\right)^{-1}\right] \\ &= \det\left[1+\Delta B_s(\tau,0)P\left(P^\dagger B_s(\Theta,0)P\right)^{-1}P^\dagger B_s(\Theta,\tau)\right] \\ &= \det\left[1+\Delta(1-G_s(\tau,\tau))\right], \end{aligned} \tag{2.91}$$

where we have used the identity $\det[1+AB] = \det[1+BA]$.

After a successful flip we have to update the Green function corresponding to its new auxiliary field configuration $G_s(\tau) \to G_{s'}(\tau)$. For the finite temperature case we need to evaluate

$$G_{s'}(\tau,\tau) = \left[1+(1+\Delta)B_s(\tau,0)B_s(\beta,\tau))\right]^{-1}, \tag{2.92}$$

and for the projective case

$$G_{s'}(\tau,\tau) = 1-(1+\Delta)B_s(\tau,0)P\left(P^\dagger B_s(\Theta,0)P\right)^{-1}P^\dagger B_s(\Theta,\tau). \tag{2.93}$$

Both expressions can be evaluated efficiently with the help of the Woodbury matrix formula due to the sparsity of the Δ matrix (cf. section 2.5).

The sampling procedure is then as follows: For a given time slice $\tau_1 = n\Delta_\tau$, we try to flip all auxiliary fields and update the Green function appropriately when field updates are accepted. To proceed, we wrap the Green function to the next time slice $\tau_2 = (n+1)\Delta_\tau$ such that

$$G_s(\tau_2,\tau_2) = B_s(\tau_2,\tau_1)G_s(\tau_1,\tau_1)B_s(\tau_2,\tau_1)^{-1}, \tag{2.94}$$

after which we can again try to flip all auxiliary fields. In this manner we can sweep back and forth and take measurements in between the updates using Wick's theorem.

2.3.3 Green function representation in LCT-INT

Vertex updates

For the LCT-INT algorithm, the configuration space is given by the set of all possible vertex configurations of the interaction expansion

$$\mathcal{C}_k = \{(x_1, \tau_1), \ldots, (x_k, \tau_k)\}. \tag{2.95}$$

The sampling of the configuration space is performed by adding and removing vertices similarly to the CT-INT algorithm, however the configuration weights are expressed via the Green function as in the BSS algorithm. To minimize the amount of wrapping operations on the Green function, the imaginary time interval is split into M intervals of size Δ_{window},

$$\Delta_{\text{window}} = \begin{cases} \frac{\beta}{M} \text{ , finite temperature} \\ \frac{\Theta}{M} \text{ , projective} \end{cases} . \tag{2.96}$$

The different intervals are then updated individually, which limits the maximum wrapping time after each update to Δ_{window}.

The probability to add a vertex, at time τ and on bond $(i,j) \in \langle i,j \rangle$, to the current configuration can be calculated as [17, 18]

$$\begin{aligned} R_{\text{add}} &= P_k^{\text{add}} \frac{w(\mathcal{C}_{k+1})}{w(\mathcal{C}_k)} \\ &= P_k^{\text{add}} \left(-\frac{V}{4}\right) \frac{\det\left[1 + B_{\mathcal{C}_{k+1}}(\beta, 0)\right]}{\det\left[1 + B_{\mathcal{C}_k}(\beta, 0)\right]} \\ &= P_k^{\text{add}} \left(-\frac{V}{4}\right) \frac{\det\left[1 + B_{\mathcal{C}_k}(\beta, \tau) X(i,j) B_{\mathcal{C}_k}(\tau, 0)\right]}{\det\left[1 + B_{\mathcal{C}_k}(\beta, 0)\right]} \\ &= P_k^{\text{add}} \left(-\frac{V}{4}\right) \det\left[1 + (X(i,j) - 1)(1 - G_{\mathcal{C}_k}(\tau))\right], \end{aligned} \tag{2.97}$$

where we have used $\Delta = X(i,j) - 1$ in Eqns. (2.89, 2.90). The normalization factor is given by

$$P_{\text{add}} = \frac{N_b \Delta_{\text{window}}}{N_\Delta + 1}, \tag{2.98}$$

where N_b is the number of interacting bonds, Δ_{window} is the window size and N_Δ is the number of vertices in the window. Following the calculation of Eq. (2.91), we obtain the

same result for the projective algorithm

$$\begin{aligned} R_{\text{add}} &= P_k^{\text{add}} \left(-\frac{V}{4}\right) \frac{\det\left[P^\dagger B_{\mathcal{C}_{k+1}}(\Theta,0)P\right]}{\det\left[P^\dagger B_{\mathcal{C}_k}(\Theta,0)P\right]} \\ &= P_k^{\text{add}} \left(-\frac{V}{4}\right) \det\left[1+(X(i,j)-1)(1-G_{\mathcal{C}_k}(\tau))\right]. \end{aligned} \tag{2.99}$$

To remove a vertex from the current configuration at time τ, we simply need to invert Eqs. (2.97),

$$\begin{aligned} R_{\text{remove}} &= P_k^{\text{remove}} \frac{w(\mathcal{C}_{k-1})}{w(\mathcal{C}_k)} \\ &= P_k^{\text{remove}} \left(-\frac{V}{4}\right) \frac{\det\left[1+B_{\mathcal{C}_k}(\beta,0)\right]}{\det\left[1+B_{\mathcal{C}_{k-1}}(\beta,0)\right]} \\ &= P_k^{\text{remove}} \left(-\frac{V}{4}\right) \frac{\det\left[1+B_{\mathcal{C}_k}(\beta,\tau)X^{-1}(i,j)B_{\mathcal{C}_k}(\tau,0)\right]}{\det\left[1+B_{\mathcal{C}_k}(\beta,0)\right]} \\ &= P_k^{\text{remove}} \left(-\frac{V}{4}\right) \det\left[1+(X^{-1}(i,j)-1)(1-G_{\mathcal{C}_k}(\tau))\right], \end{aligned} \tag{2.100}$$

where the normalization factor is given by

$$P_{\text{remove}} = \frac{N_\Delta}{N_b \Delta_{\text{window}}}, \tag{2.101}$$

and the result for the projective algorithm can again be expressed identically via the projective Green function.

After a successful update, the Green function must be changed according to the new vertex configuration $G_{\mathcal{C}}(\tau) \to G_{\mathcal{C}'}(\tau)$. We can combine both vertex addition $(+)$ and removal $(-)$ to obtain for finite temperatures

$$G_{\mathcal{C}'}(\tau,\tau) = \left[1+X^{\pm}(i,j)B_{\mathcal{C}}(\tau,0)B_{\mathcal{C}}(\beta,\tau))\right]^{-1}, \tag{2.102}$$

and for the projective case

$$G_{\mathcal{C}'}(\tau,\tau) = 1 - X^{\pm}(i,j)B_{\mathcal{C}}(\tau,0)P\left(P^\dagger B_{\mathcal{C}}(\Theta,0)P\right)^{-1} P^\dagger B_{\mathcal{C}}(\Theta,\tau). \tag{2.103}$$

Both expressions can be evaluated efficiently due to the sparsity of the $X(i,j)$ matrix (cf. section 2.5).

2.4 Observables and correlation functions

The previous sections focused on how to generate configurations which are distributed according their contributions to the partition function

$$Z = \sum_{\mathcal{C}} w(\mathcal{C}), \tag{2.104}$$

where $\sum_{\mathcal{C}}$ can contain summations over both discrete and continuous variables. In the following we shall discuss how to extract expectation values of observables from such distributions.

The expectation value of a general observable A in a continuous ensemble $\mathcal{E}$ distributed by ρ is given by

$$\langle A \rangle = \frac{1}{Z} \int_{x \in \mathcal{E}} \mathcal{A}(x) \rho(x) dx, \tag{2.105}$$

with Z being the partition function $Z = \int_{x \in \mathcal{E}} \rho(x) dx$ and $\mathcal{A}$ being the representation depended estimator of A. The Monte Carlo average denotes the average taken over N measurements taken during the Markov process and serves as an approximation to Eq. (2.105),

$$\langle A \rangle \approx \langle A \rangle_{\text{MC}} = \frac{1}{N} \sum_{i=1}^{N} \mathcal{A}(x_i). \tag{2.106}$$

2.4.1 Wick theorem

We have seen in section 2.3 that the state of the sampling process is characterized by the single particle Green function for the CT-INT, BSS and LCT-INT algorithm. Furthermore, in each case the Green function effectively corresponds to a non-interacting system - this is achieved either directly by the interaction expansion in CT-INT and LCT-INT, or by the decoupling of the interaction in BSS. We can therefore employ the Wick theorem to compute an estimator of an arbitrary observable from the Green function representation directly during the sampling process.

A generic, equal-time observable with four fermionic operators can be decomposed as follows,

$$\begin{aligned} \langle c_a^\dagger c_b c_c^\dagger c_d \rangle_{\mathcal{C}} &= \langle c_a^\dagger c_b \rangle_{\mathcal{C}} \langle c_c^\dagger c_d \rangle_{\mathcal{C}} + \langle c_a^\dagger c_d \rangle_{\mathcal{C}} \langle c_b c_c^\dagger \rangle_{\mathcal{C}} \\ &= (\delta_{ab} - G_{ba})(\delta_{cd} - G_{dc}) + (\delta_{ad} - G_{da}) G_{bc}. \end{aligned} \tag{2.107}$$

For time displaced observables, the Wick theorem works analogously. Given $\tau_1 > \tau_2$, we find

$$\begin{aligned}\langle c_a^\dagger(\tau_1)c_b(\tau_1)c_c^\dagger(\tau_2)c_d(\tau_2)\rangle_{\mathcal{C}} &= \langle c_a^\dagger(\tau_1)c_b(\tau_1)\rangle_{\mathcal{C}}\langle c_c^\dagger(\tau_2)c_d(\tau_2)\rangle_{\mathcal{C}} + \langle c_a^\dagger(\tau_1)c_d(\tau_2)\rangle_{\mathcal{C}}\langle c_b(\tau_1)c_c^\dagger(\tau_2)\rangle_{\mathcal{C}} \\ &= (\delta_{ab} - G_{ba}(\tau_1,\tau_1))(\delta_{cd} - G_{dc}(\tau_2,\tau_2)) - G_{da}(\tau_2,\tau_1)G_{bc}(\tau_1,\tau_2).\end{aligned} \tag{2.108}$$

2.4.2 Measurements in CT-INT

To illustrate the use of the Wick theorem in CT-INT, let us assume we want to measure the density-density correlation function between two points (i, j) on a lattice of spinless fermions

$$C(i,j) = \left\langle \eta_i\eta_j \left(n_i - \frac{1}{2}\right)\left(n_j - \frac{1}{2}\right)\right\rangle \tag{2.109}$$

with staggered sublattice factors η_i and η_j. Following the calculation in section 2.2.1 one can expand Eq. (2.109) into an expression similar to the interaction expansion of the partition function

$$\begin{aligned}Z &= Z_0 \sum_{k=0}^{\infty} \frac{(-V)^k}{k!} \int_0^\beta d\tau_2 \int_0^\beta d\tau_4 \cdots \int_0^\beta d\tau_{2k} \times \\ &\quad \left\langle \left(n_{i_1}(\tau_1) - \frac{1}{2}\right)\left(n_{i_2}(\tau_2) - \frac{1}{2}\right)\ldots\left(n_{2k-1}(\tau_{2k-1}) - \frac{1}{2}\right)\left(n_{2k}(\tau_{2k}) - \frac{1}{2}\right)\right\rangle_0 \\ &= Z_0 \sum_{k=0}^{\infty} \frac{(-V)^k}{k!} \int_0^\beta d\tau_2 \int_0^\beta d\tau_4 \cdots \int_0^\beta d\tau_{2k} \det(G^k)\end{aligned} \tag{2.110}$$

$$\begin{aligned}C(i,j) &= \frac{\eta_i\eta_j}{\beta}\frac{Z_0}{Z} \sum_{k=0}^{\infty} \frac{(-V)^k}{k!} \int_0^\beta d\tau_2 \int_0^\beta d\tau_4 \cdots \int_0^\beta d\tau_{2k} \int_0^\beta d\tau \times \\ &\quad \left\langle \left(n_{i_1}(\tau_1) - \frac{1}{2}\right)\left(n_{i_2}(\tau_2) - \frac{1}{2}\right)\ldots\left(n_{i_{2k-1}}(\tau_{2k-1}) - \frac{1}{2}\right)\left(n_{i_{2k}}(\tau_{2k}) - \frac{1}{2}\right) \times \right. \\ &\quad \left. \left(n_i(\tau) - \frac{1}{2}\right)\left(n_j(\tau) - \frac{1}{2}\right)\right\rangle_0 \\ &= \frac{\eta_i\eta_j}{\beta}\frac{Z_0}{Z} \sum_{k=0}^{\infty} \frac{(-V)^k}{k!} \int_0^\beta d\tau_2 \int_0^\beta d\tau_4 \cdots \int_0^\beta d\tau_{2k} \int_0^\beta d\tau \det(G^{k;ij\tau})\end{aligned} \tag{2.111}$$

where we have defined the $(2k+2) \times (2k+2)$ extended Green's function matrix

$$G^{k;ij\tau} = \left(\begin{array}{c|cc} G^0_{i_p i_q}(\tau_p - \tau_q) - \frac{\delta_{pq}}{2} & G^0_{i_p i}(\tau_{i_p} - \tau_i) & G^0_{i_p j}(\tau_{i_p} - \tau_j) \\ \hline G^0_{i i_q}(\tau_i - \tau_{i_q}) & 0 & G^0_{ij}(0^+) \\ G^0_{j i_q}(\tau_j - \tau_{i_q}) & G^0_{ji}(0^-) & 0 \end{array} \right). \tag{2.112}$$

The factor $\frac{1}{\beta}$ appears in Eq. (2.111) through the insertion of unity $\beta \int_0^\beta e^{H_0\tau} e^{-H_0\tau} d\tau = 1$ that is used to create time depended operators $n_i(\tau)$ and $n_j(\tau)$ to combine them with the other operators into the sampling process. Similar to the partition function Eq. (2.111) can be rewritten as a sum of weighted configurations

$$C(i,j) = \frac{1}{Z} \sum_{\mathcal{C}} v(\mathcal{C}) \tag{2.113}$$

$$v(\mathcal{C}) = Z_0 \eta_i \eta_j \frac{(-V)^k}{\beta} \det(G^{k;ij\tau}) \tag{2.114}$$

One can now rewrite Eq. (2.113) in terms of the partition function weights $w(\mathcal{C})$

$$\begin{aligned} C(i,j) &= \frac{1}{Z} \sum_{\mathcal{C}} v(\mathcal{C}) \frac{w(\mathcal{C})}{w(\mathcal{C})} \\ &= \frac{1}{Z} \sum_{\mathcal{C}} \mathcal{A}(\mathcal{C}) w(\mathcal{C}) \end{aligned} \tag{2.115}$$

to obtain the Monte Carlo estimator

$$\begin{aligned} \mathcal{A}(\mathcal{C}) &= \frac{v(\mathcal{C})}{w(\mathcal{C})} \\ &= \eta_i \eta_j \frac{Z_0}{\beta} \frac{\det(G^{k;ij\tau})}{\det(G^k)} \end{aligned} \tag{2.116}$$

such that in agreement with Eq. (2.106)

$$C_{\mathrm{MC}}(i,j) = \frac{1}{N} \sum_{m=1}^{N} \mathcal{A}(\mathcal{C}_m) \approx C(i,j). \tag{2.117}$$

2.4.3 Measurements in BSS and LCT-INT

The measurement procedure of the BSS and LCT-INT algorithm is fairly simple, because we have direct access to the single-particle Green function $G_{\mathcal{C}}(\tau,\tau)$ at all times during the sampling process. We can therefore evaluate Eqs. (2.107, 2.108) directly after each update step. In the projective formulation, it is important to take measurements only in a

measurement window around $\frac{\Theta}{2}$, such that

$$|\tau - \Delta_{\text{measure}}| \approx \frac{\Theta}{2}. \tag{2.118}$$

In this way it is ensured that the expectation values are taken with regards to the sufficiently projected state.

To perform time-displaced measurements of the form $O(\tau)$, we start at time τ_1 and propagate the Green function according to Eq. (2.49), such that we obtain $G_{\mathcal{C}}(\tau_1, \tau_2)$ and $\tau = \tau_1 - \tau_2$. Again, in the projective formulation the measurement should be centered around the half-way point at $\frac{\Theta}{2}$, i.e. $\tau_1 = \frac{\Theta}{2} + \frac{\tau}{2}$ and $\tau_2 = \frac{\Theta}{2} - \frac{\tau}{2}$. To provide a numerically stable measurement at zero temperature, we can make use of the projective property of the Green function [26]. To this extent, the time-displaced Green function is calculated as a product of Green function with smaller displacement,

$$G_{\mathcal{C}}\left(\frac{\Theta}{2} + \frac{\tau}{2}, \frac{\Theta}{2} - \frac{\tau}{2}\right) = \prod_{n=0}^{N-1} G_{\mathcal{C}}\left(\frac{\Theta}{2} - \frac{\tau}{2} + (n+1)\Delta\tau, \frac{\Theta}{2} - \frac{\tau}{2} + n\Delta\tau\right), \tag{2.119}$$

where $\tau = N\Delta\tau$.

2.5 Efficient numerical implementation

In the following sections I will discuss some of the important details of the various numerical implementations, which are required for efficient sampling and updating schemes.

2.5.1 Fast updates in CT-INT

The essential numerical ingredient of the CT-INT algorithm is the ratio of determinants that is present in every type of update. This is problematic at first sight because the computation of determinants is very costly with a $O(n^3)$ scaling for a $n \times n$ matrix. When the CT-INT algorithm was first proposed by Rubtsov it was noted that one can use the fact that the matrices involved in each update differ only by a small number of rows and columns, which allows to reduce the complexity of each matrix update to $O(n^2)$ and makes the method numerically feasible.

It turns out that the key to an efficient numerical treatment is the inverse of the propagator matrix $M^k = \left(G^k\right)^{-1}$, which we keep in memory at all times. Each update therefore consists of two steps [22, 27]:

- Calculation of the acceptance probability, which involves the computation of determinant ratio.
- Upon acceptance, calculate the transition of $M^k \to (M')^{k'}$ corresponding to the new configuration.

Efficient vertex addition

To calculate the acceptance probability in an efficient manner one makes use of the matrix determinant lemma

$$\det \begin{pmatrix} A & B \\ C & D \end{pmatrix} = \det(A) \det(D - CA^{-1}B) \tag{2.120}$$

which factorizes the determinant of an arbitrary block matrix.

Let us consider the addition of n (worm) vertices[3]. The update is characterized by the configuration transition $\mathcal{C}^k \to \mathcal{C}^{k+n}$. The Green's function matrix of the new configuration can be partitioned analogously to Eq. (2.120)

$$G^{k+n} = \begin{pmatrix} G^k & u \\ v & w \end{pmatrix} \tag{2.121}$$

where G^k is a $2k \times 2k$ matrix, u is a $2k \times 2n$ matrix, v is a $2n \times 2k$ matrix and w is a $2n \times 2n$ matrix[4]. All matrix elements are given by the bare Green's function (see Eq. (2.25) for the spinless fermion case) and can be looked up from memory.

Combining Eq. (2.120) and (2.121) we obtain

$$\frac{\det(G^{k+n})}{\det(G^k)} = \det\left(w - vM^k u\right) \tag{2.122}$$

where $M^k = \left(G^k\right)^{-1}$ is known and stored in memory from the previous update. The determinant ratio is reduced to the addition and determinant of a $2n \times 2n$ matrix as well as a $(2n \times 2k)(2k \times 2k)(2k \times 2n)$ matrix product[5]. Given that the number of vertices added is much smaller than the average perturbation order $n \ll k$ the former are essentially free and only the latter give a significant contribution to the computational effort. Overall

[3] The same principles apply both for regular interaction vertices as well as worm vertices.

[4] This is for the spinless fermion nearest-neighbor interaction. Depending on what operators are involved in the interaction expansion the dimension might change.

[5] The matrix product can be handled efficiently by calling the optimized BLAS routine *dgemm*.

this constitutes a significant improvement to the naive determinant ratio and results in the mentioned $O(k^2)$ scaling.

To update the inverse Green's function $M^k \to M^{k+n}$ we make the partition ansatz

$$M^{k+n} = \begin{pmatrix} P & Q \\ R & S \end{pmatrix} \tag{2.123}$$

where the dimensions of the blocks are identical to Eq. (2.121). Note that in contrast to Eq. (2.121) $P \neq M^k$. Using simple block matrix inversion formulas[6] we obtain

$$S = \left(w - vM^k u\right)^{-1} \tag{2.124}$$

$$Q = -M^k u S \tag{2.125}$$

$$R = -SvM^k \tag{2.126}$$

$$P = M^k + M^k u S v M^k. \tag{2.127}$$

The overall scaling is equal to Eq. (2.122) as the inverse in Eq. (2.124) is only of a $2n \times 2n$ matrix and the remaining block matrix operations amount to $O(k^2)$ scaling.

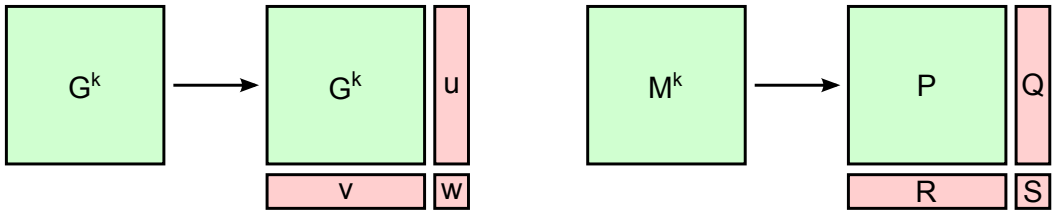

(a) Green's function matrix (b) Inverted Green's function matrix

Figure 2.2: Visual illustration of the block partitioning during the addition of vertices.

Efficient vertex removal

For the vertex removal it is important to that the vertices have the correct alignment in the matrix to make use of Eq. (2.122) and Eq. (2.124). In particular removing n random vertices corresponds to removing rows and columns from the middle of the matrix, which complicates the partitioning of the matrices. To make use of the block matrix formulas a simple solution is to swap the vertices which are to be removed with the outer most vertices[7]. By doing so

[6] It is also possible to use the Sherman-Morrison-Woodbury formula to update inverse matrices. This however has the disadvantage that one has to apply the formula twice because one has to update rows and columns separately, which results in more matrix multiplications and thus slower code.

[7] Remember that the determinant of the Green's function matrix corresponds to the weight of unordered configurations. It is therefore legitimate to change the order of the vertices in the matrix without changing

we arrive at the partitioning

$$G^k = \begin{pmatrix} G^{k-n} & u \\ v & w \end{pmatrix}, \quad M^k = \begin{pmatrix} P & Q \\ R & S \end{pmatrix}. \tag{2.128}$$

The determinant ratio is then given by

$$\frac{\det\left(G^{k-n}\right)}{\det\left(G^k\right)} = \frac{1}{\det\left(w - vM^k u\right)} = \det(S) \tag{2.129}$$

The inverse Green's function matrix M^k of the previous configuration is fully in memory and no actual computation has to be carried to out other than the determinant of a small $2n \times 2n$ matrix. The updated M^{k-n} can be computed from Eq. (2.127)

$$M^{k-n} = P - QS^{-1}R. \tag{2.130}$$

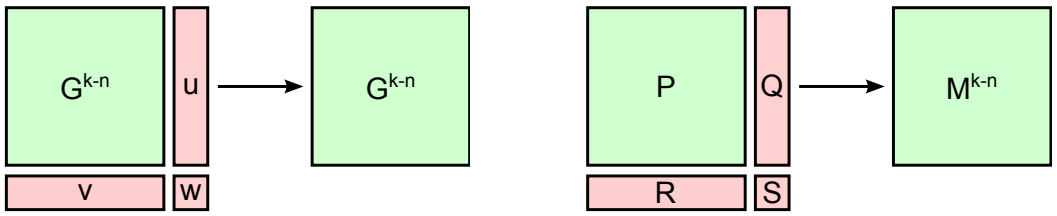

(a) Green's function matrix (b) Inverted Green's function matrix

Figure 2.3: Visual illustration of the block partitioning during the removal of vertices.

The worm shift update is analogous in the sense that it can be understood as a removing all worms and adding the shifted worm vertices.

2.5.2 Worm algorithm for CT-INT

To characterize phase transitions one has to determine and calculate the relevant order parameters of the transition. The traditional measurement approach involves expressing the expectation value as a weighted sum over an Monte Carlo estimator. The importance sampling is done over Feynman diagram contributions to the partition function and from these configurations the observable configurations are constructed.

One disadvantage of this method is that there is no guarantee that the importance sampling will yield configurations that contribute with high weight to the observable ensemble.

the weight. This is also evident explicitly because swapping both rows and columns of a matrix leaves the determinant unchanged.

Furthermore for each expectation value of the form (2.109) the estimator has to be evaluated, which typically involves the computation of a determinant ratio as shown in Eq. (2.116). This can become inefficient if the order parameter is a large sum of expectation values with different orders of magnitude. It would be desirable to also perform importance sampling in the contributions to the order parameter sum, such as to limit the estimator evaluations to the significantly contributing terms.

The idea of the worm algorithm is to extend the configuration space and provide a way to sample diagram contributions to the partition function and order parameter separately. In this section we will work out the details of the worm algorithm in regards to the order parameters relevant to the spinless fermion model (see section 2.2.1), however the method can be generalized to different models in a straightforward fashion.

To detect the quantum phase transition of the spinless fermion model the relevant observables are given by the square and quartic of the CDW (charge density wave) order parameter as well as the RG-invariant Binder ratio [28]

$$M_2 = \frac{1}{N_s^2} \sum_{ij} \eta_i \eta_j \left\langle \left(n_i - \frac{1}{2}\right) \left(n_j - \frac{1}{2}\right) \right\rangle \tag{2.131}$$

$$M_4 = \frac{1}{N_s^4} \sum_{ijkl} \eta_i \eta_j \eta_k \eta_l \left\langle \left(n_i - \frac{1}{2}\right) \left(n_j - \frac{1}{2}\right) \left(n_k - \frac{1}{2}\right) \left(n_l - \frac{1}{2}\right) \right\rangle \tag{2.132}$$

$$B = \frac{M_4}{M_2^2} \tag{2.133}$$

where $N_s = 2L^2$ is the number of sites in the honeycomb lattice of linear dimension L.

The configuration weight with respect to M_2 and M_4 can be derived by the same interaction expansion performed on the partition function (see section 2.2.1 and Eq. (2.111), and Ref. [22]). It yields

$$M_2 = \frac{1}{\beta N_s^2} \frac{Z_0}{Z} \sum_{k=0}^{\infty} \frac{(-V)^k}{k!} \int_0^\beta d\tau_2 \int_0^\beta d\tau_4 \cdots \int_0^\beta d\tau_{2k} \int_0^\beta d\tau \sum_{ij} \eta_i \eta_j \det(G^{k;ij\tau}) \tag{2.134}$$

$$M_4 = \frac{1}{\beta N_s^4} \frac{Z_0}{Z} \sum_{k=0}^{\infty} \frac{(-V)^k}{k!} \int_0^\beta d\tau_2 \int_0^\beta d\tau_4 \cdots \int_0^\beta d\tau_{2k} \int_0^\beta d\tau \sum_{ijkl} \eta_i \eta_j \eta_k \eta_l \det(G^{k;ijkl\tau}) \tag{2.135}$$

with the extended Green's function matrix $G^{k;ij(kl)\tau}$ defined as in Eq. (2.112). To ease notation we introduce the rescaled observables

$$W_2 = \zeta_2 \beta N_s^2 Z M_2 \tag{2.136}$$
$$W_4 = \zeta_4 \beta N_s^4 Z M_4 \tag{2.137}$$

where the scaling factors ζ_2 and ζ_4 balance the relative importance of each configuration sector and can be chosen arbitrarily. They can be tuned during the thermalization process such that each sector is covered equally. The last (two) interaction vertex (vertices) of $G^{k;ij(kl)\tau}$ are referred to as worm(s) in analogy to the dangling worm ends in the world line worm algorithm. The configuration space is enlarged to cover Z, W_2 and W_4

$$\{\mathcal{C}\} = \{\mathcal{C}\}_Z \cup \{\mathcal{C}\}_{W_2} \cup \{\mathcal{C}\}_{W_4} \tag{2.138}$$

and the overall volume is given by

$$Z + W_2 + W_4 = Z_0 \sum_{\alpha=Z,W_2,W_4} \sum_{\mathcal{C}\in\{\mathcal{C}\}_\alpha} w_\alpha(\mathcal{C}) \tag{2.139}$$

with the configuration weights in each sector [22]

$$w_Z(\mathcal{C}) = (-V)^k \det(G^k) \tag{2.140}$$
$$w_{W_2}(\mathcal{C}) = \eta_i \eta_j \zeta_2 (-V)^k \det(G^{k;ij\tau}) \tag{2.141}$$
$$w_{W_4}(\mathcal{C}) = \eta_i \eta_j \eta_k \eta_l \zeta_4 (-V)^k \det(G^{k;ijkl\tau}). \tag{2.142}$$

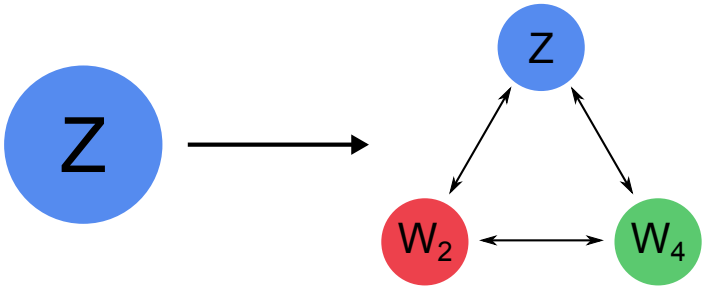

Figure 2.4: Schematic picture of the configuration space enlargement. Instead of only sampling Z (left side), we extend the configuration space to also include W_2 and W_4 (right side).

Measurements in worm space

One advantage of the worm algorithm is that the measurement process is trivial and constant in time as one only has to keep track of a histogram of worm positions. The estimators of Z, W_2 and W_4 are directly given by the relative time spent in each sector

$$\langle Z\rangle_{\text{MC}} = \frac{\Delta Z}{\Delta Z + \Delta W_2 + \Delta W_4} \tag{2.143}$$

$$\langle W_2\rangle_{\text{MC}} = \frac{\Delta W_2}{\Delta Z + \Delta W_2 + \Delta W_4} \tag{2.144}$$

$$\langle W_4\rangle_{\text{MC}} = \frac{\Delta W_4}{\Delta Z + \Delta W_2 + \Delta W_4} \tag{2.145}$$

$$\tag{2.146}$$

The Monte Carlo averages of the observables (2.131), (2.132) and (2.133) are then given by

$$\langle M_2\rangle_{\text{MC}} = \frac{1}{\zeta_2 \beta N_s^2} \frac{\langle W_2\rangle_{\text{MC}}}{\langle Z\rangle_{\text{MC}}} \tag{2.147}$$

$$\langle M_4\rangle_{\text{MC}} = \frac{1}{\zeta_4 \beta N_s^4} \frac{\langle W_4\rangle_{\text{MC}}}{\langle Z\rangle_{\text{MC}}} \tag{2.148}$$

$$\langle B\rangle_{\text{MC}} = \frac{\beta\zeta_2^2}{\zeta_4} \frac{\langle W_4\rangle_{\text{MC}}\langle Z\rangle_{\text{MC}}}{\langle W_2\rangle_{\text{MC}}^2}. \tag{2.149}$$

The density-density correlation function can be retrieved from the relative weight of the worm positions in W_2 space

$$C(i,j) = \frac{1}{\zeta_2 \beta} \frac{\eta_i \eta_j \Delta W_2(i,j)}{\Delta Z} \tag{2.150}$$

Updates in worm space

The worm algorithm involves both vertex addition/removal updates in each distinct sector as well as specific worm updates that change between the different regions in configuration space. The addition/removal updates for regular interaction vertices is analogous to section 2.5.1 with the modification that one has to replace G^k by $G^{k;ij(kl)\tau}$ if the algorithm resides in W_2 (W_4) space. The remaining updates can be categorized as follows [22]:

- $\mathbf{Z \leftrightarrow W_2}$:
  To go from Z to W_2 we create a worm at (i, j, τ). Since the worm can be located anywhere on the lattice (as opposed to the nearest-neighbor interaction vertices) there is a freedom in choosing i and j. One possibility is to take a random site i and choose

site j from a set of neighborhood sites. If the neighborhood around site i contains m sites to choose j from, the probability to select a specific pair (i, j) is given by $\frac{1}{N_s m}$. As to not create a bias upon removing the worm both sites have to fulfill the neighborhood condition again. The probability to pick a specific imaginary time τ is $\frac{d\tau}{\beta}$.

Similar to section 2.5.1 the acceptance probabilities to add/remove the worm are given by

$$A(\mathcal{C}_Z \to \mathcal{C}_{W_2}) = \min\left(1, \frac{P(\mathcal{C}_{W_2} \to \mathcal{C}_Z)p(\mathcal{C}_{W_2})}{P(\mathcal{C}_Z \to \mathcal{C}_{W_2})p(\mathcal{C}_Z)}\right) \tag{2.151}$$

$$= \min\left(1, \frac{a_{\mathcal{C}_{W_2}\to\mathcal{C}_Z}}{a_{\mathcal{C}_Z\to\mathcal{C}_{W_2}}} \frac{1}{\frac{1}{N_s m\beta}} \frac{w(\mathcal{C}_{W_2})}{w(\mathcal{C}_Z)}\right) \tag{2.152}$$

$$= \min\left(1, \frac{a_{\mathcal{C}_{W_2}\to\mathcal{C}_Z}}{a_{\mathcal{C}_Z\to\mathcal{C}_{W_2}}} \eta_i\eta_j\zeta_2 N_s m\beta \frac{\det(G^{k;ij\tau})}{\det(G^k)}\right) \tag{2.153}$$

$$A(\mathcal{C}_{W_2} \to \mathcal{C}_Z) = \min\left(1, \frac{a_{\mathcal{C}_Z\to\mathcal{C}_{W_2}}}{a_{\mathcal{C}_{W_2}\to\mathcal{C}_Z}} \eta_i\eta_j \frac{1}{\zeta_2 N_s m\beta} \frac{\det(G^k)}{\det(G^{k;ij\tau})}\right) \tag{2.154}$$

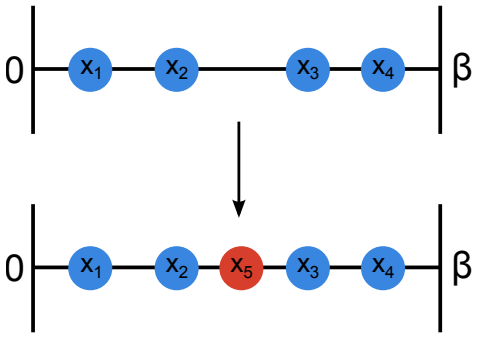

Figure 2.5: Illustration of the $Z \to W_2$ update through worm vertex addition. The new configuration contains all previous vertices (blue dots) in addition to the new worm vertex (green dot).

Another way to effectively change between Z and W_2 space is to reinterpret an existing interaction vertex as a worm. This process is called an open update and is inverted by a close update. The advantage of this special update is that the configuration does not change technically and therefore the determinant ratio is one. The perturbation order is

changed by one in the process. The acceptance probabilities are

$$A(\mathcal{C}_Z \to \mathcal{C}_{W_2}) = \min\left(1, \frac{a_{\text{close}}}{a_{\text{open}}} 2\zeta_2 \frac{k}{V}\right) \tag{2.155}$$

$$A(\mathcal{C}_{W_2} \to \mathcal{C}_Z) = \min\left(1, \frac{a_{\text{open}}}{a_{\text{close}}} \frac{1}{2\zeta_2} \frac{V}{k+1}\right) \tag{2.156}$$

where the factor 2 appears because (i, j, τ) and (j, i, τ) are counted as two different configurations.

- $\mathbf{W_2 \leftrightarrow W_4}$:
  To progress from W_2 to W_4 another single worm is added analogously to the $Z \to W_2$ transition. The imaginary time τ is equal to the existing worm. This is because in the interaction expansion of M_4 (see Eq. (2.135)) all particle number operators have the same imaginary time argument. In different models the worm each worm node might correspond to a single fermionic createn/annihilation operator with individual arguments. In this case one has to make slight changes to the proposal probabilities and Green's function matrix.

$$A(\mathcal{C}_{W2} \to \mathcal{C}_{W_4}) = \min\left(1, \frac{a_{\mathcal{C}_{W_4} \to \mathcal{C}_{W_2}}}{a_{\mathcal{C}_{W_2} \to \mathcal{C}_{W_4}}} \eta_k \eta_l \frac{N_s m \zeta_4}{\zeta_2} \frac{\det(G^{k;ijkl\tau})}{\det(G^{k;ij\tau})}\right) \tag{2.157}$$

$$A(\mathcal{C}_{W_4} \to \mathcal{C}_{W_2}) = \min\left(1, \frac{a_{\mathcal{C}_{W_2} \to \mathcal{C}_{W_4}}}{a_{\mathcal{C}_{W_4} \to \mathcal{C}_{W_2}}} \eta_k \eta_l \frac{\zeta_2}{N_s m \zeta_4} \frac{\det(G^{k;ij\tau})}{\det(G^{k;ijkl\tau})}\right) \tag{2.158}$$

- $\mathbf{Z \leftrightarrow W_4}$:
  To go from the partition function sector to the W_4 one has to insert two worms. Again there is a freedom of choice in where the worm nodes are located on the lattice as long as worm addition and removal updates stay inverse to each other. One option is to choose one site at random and select three sites from a neighborhood around that site.

$$A(\mathcal{C}_{W2} \to \mathcal{C}_{W_4}) = \min\left(1, \frac{a_{\mathcal{C}_{W_4} \to \mathcal{C}_Z}}{a_{\mathcal{C}_Z \to \mathcal{C}_{W_4}}} \eta_i \eta_j \eta_k \eta_l \frac{N_s m^3 \beta \zeta_4}{\zeta_2} \frac{\det(G^{k;ijkl\tau})}{\det(G^{k;ij\tau})}\right) \tag{2.159}$$

$$A(\mathcal{C}_{W_4} \to \mathcal{C}_{W_2}) = \min\left(1, \frac{a_{\mathcal{C}_Z \to \mathcal{C}_{W_4}}}{a_{\mathcal{C}_{W_4} \to \mathcal{C}_Z}} \eta_i \eta_j \eta_k \eta_l \frac{\zeta_2}{N_s m^3 \beta \zeta_4} \frac{\det(G^{k;ij\tau})}{\det(G^{k;ijkl\tau})}\right) \tag{2.160}$$

- **Worm updates :**
  It is also possible to perform updates on the worm vertices without changing to a different sector. This can become necessary to make sure every worm configuration can be sampled ergodicly. The worm shift update moves worm vertices to different

lattice sites and/or changes the imaginary time argument τ. In our case we move one worm site i to a random site i' in a neighborhood of the original position and modify the time argument $\tau' = \tau + r$ where $r \in [-0.05\beta, 0.05\beta]$. Since the worm shift update is inverse to itself no ratio of a priori proposal probabilities comes into play. The acceptance probability is given by

$$A(\mathcal{C} \to \mathcal{C}') = \min\left(1, \eta_i \eta_{i'} \frac{\det(G^{k;i'j(kl)\tau'})}{\det(G^{k;ij(kl)\tau})}\right). \tag{2.161}$$

Furthermore worm replacement updates have been proposed by Gunacker et al. [29] which involve swapping the arguments of an interaction vertex with a worm vertex. It was shown that these updates can significantly reduce the auto-correlation times when the worm corresponds to a pair of creation/annihilation operators with different time arguments. The replacement update then allows to sample worm configurations that where the worm operators are temporal far apart. Since in our case the worm corresponds to configurations with the same time argument this update did not yield any improvements to auto-correlation.

Note that the acceptance probabilities of several updates depend explicitly on the values of ζ_2 and ζ_4. One can therefore try to increase the acceptance rate by finding optimal values for ζ_2 and ζ_4. The minimal requirement is that they are chosen such that all updates have a finite acceptance rate.

2.5.3 Fast updates in BSS

In Eq. (2.90) we calculated the acceptance probability as $R = \det[M]$, such that we need to calculate the determinant of the matrix $M = 1 + \Delta(1 - G(\tau, \tau))$. To evaluate Eq. (2.90) efficiently, we can make use of the fact that Δ is a heavily sparse matrix. This sparsity is caused by the interaction V, which can typically be decomposed such that it acts only on a single lattice site or bond. Assuming that only the auxiliary field pertinent to the bond $(i, j) \in \langle i, j\rangle_b$ is modified by the update, we can rewrite Eq. (2.90) as the determinant of a 2×2 matrix [24, 25]

$$\begin{aligned} R_{\boldsymbol{s}} &= \det[1_{2\times 2} + \Delta^{ij,ij}(1_{2\times 2} - G_{\boldsymbol{s}}^{ij,ij}(\tau, \tau))] \\ &= \det[M^{ij,ij}]. \end{aligned} \tag{2.162}$$

where the upper index ij, ij denotes a projection onto the two-dimensional block defined by the index pair (i, j). To efficiently update the Green function matrix after a successful update,

we keep the matrix $M^{ij,ij}$ in memory. The updated Green function matrix is then given by

$$G_{\boldsymbol{s}'} = G_{\boldsymbol{s}} + G_{\boldsymbol{s}}^{\bullet,ij}\Delta^{ij,ij}(M^{ij,ij})^{-1}(G_{\boldsymbol{s}} - 1)^{ij,\bullet}, \tag{2.163}$$

where $\bullet, ij$ denotes a projection onto the columns and $ij, \bullet$ denotes a projection onto the rows given by (i, j).

2.5.4 Fast updates in LCT-INT

Updates rules

For the LCT-INT algorithm the acceptance probability of either adding or removing vertices has the same form as for the BSS algorithm, however the explicit form of Δ is simplified and independent of any auxiliary field. From Eqs. (2.97, 2.100) follows that the acceptance probability is proportional to [17, 18]

$$R_{\mathcal{C}}^{\text{add/rem}} \propto \det[1_{2\times 2} + (X(i,j)^{\pm} - 1_{2\times 2})(1_{2\times 2} - G_{\mathcal{C}}^{ij,ij}(\tau,\tau))]. \tag{2.164}$$

Furthermore, taking the explicit form of X and X^{-1} from Eq. (2.59) for the $t-V$ model we find

$$\begin{aligned} R_{\mathcal{C}}^{\text{add/rem}} &= 4(G_{\mathcal{C}})_{ij}(G_{\mathcal{C}})_{ji} \\ &= 4(G_{\mathcal{C}})_{ij}^2, \end{aligned} \tag{2.165}$$

where we have used the sublattice symmetry of the honeycomb lattice in the last step.

Similar to the BSS algorithm, we can evaluate Eq. (2.102) efficiently by making use of the sparseness of $X(i, j)$,

$$(G_{\mathcal{C}'})_{mn} = (G_{\mathcal{C}})_{mn} - \frac{(G_{\mathcal{C}})_{mj}[(G_{\mathcal{C}})_{in} - \delta_{in}]}{(G_{\mathcal{C}})_{ij}} - \frac{(G_{\mathcal{C}})_{mi}[(G_{\mathcal{C}})_{jn} - \delta_{jn}]}{(G_{\mathcal{C}})_{ji}}. \tag{2.166}$$

Optimal single-particle basis

The wrapping of the Green function to a new time $G_{\mathcal{C}}(\tau,\tau) \to G_{\mathcal{C}}(\tau',\tau')$ via Eq. (2.94) requires the evaluation of terms of the form $e^{-\tau K}$, which are costly to compute for arbitrary values of τ. This problem does not appear in the BSS formulation because in that case the imaginary time values are fixed by the discretization $\Delta\tau$. To reduce the complexity of the matrix exponential, one may perform a basis transformation into the eigen basis of the

transition matrix K. The transformed propagators are then given by [17, 18]

$$\left(U^\dagger e^{-\tau K} U\right)_{mn} = e^{-\tau E_m}\delta_{mn} \tag{2.167}$$

$$\left(U^\dagger X(i,j) U\right)_{mn} = \delta_{mn} - 2U^\dagger_{mi}U_{in} - 2U^\dagger_{mj}U_{jn} \tag{2.168}$$

where the unitary transformation matrix U is defined by $K = U\Lambda_K U^\dagger$ with $(\Lambda_K)_{mn} = E_m\delta_{mn}$. The update probabilities are then calculated from the transformed Green function $\tilde{G} = U^\dagger G U$, and measurements can be taken in either basis.

2.6 Numerical stabilization

Different types of numerical stabilization generally become necessary after a certain amount of updates has lead to a degradation in the Green function, or its representation, due to the accumulation of rounding errors or the mixing of different numerical scales.

2.6.1 Rebuilding from scratch in CT-INT

It can become necessary to rebuild the Green function matrix from scratch from the vertex list [13]. The accumulated error can be gauged by the difference of the old and new Green function matrix,

$$\Delta_{\text{err}} = |M' - M|_{\text{max}}. \tag{2.169}$$

One can choose different norms to characterize the error. In practice, the rebuilding interval should be set such that the rounding error remains controlled and at least does not exceed single floating point precision $\Delta_{\text{err}} \approx 10^{-8}$.

2.6.2 Separation of scales in BSS and LCT-INT

It turns out that the updating process as it is described in section 2.3 is not numerically stable [16, 24, 25]. The culprit is the product of matrix exponentials in the propagators $B_{\mathcal{C}}(\tau_1, \tau_2)$, which mix values of different scale and propagate them exponentially. Ultimately, the small scales are washed out completely by the largest term. The different scales must therefore be separated during the update process, such that only matrices with values of similar scales are multiplied directly. This can be achieved by the singular value decomposition

(SVD),

$$B_{m\times n} = U_{m\times m} D_{m\times n} V_{n\times n}, \tag{2.170}$$

where $U_{m\times m}$ and $V_{n\times n}$ are unitary matrices of similar scale. The diagonal matrix $D_{m\times n}$ contains the singular values of $B_{m\times n}$, which encode the different scales present in $B_{m\times n}$.

Alternatively, one may use the QR factorization with column pivoting,

$$B_{m\times n} = Q_{m\times m} R_{m\times n} P^{\dagger}_{n\times n}, \tag{2.171}$$

where $Q_{m\times m}$ is a unitary matrix, $R_{m\times n}$ is an upper triagonal matrix and $P^{\dagger}_{n\times n}$ is a permutation matrix. One can separate the scales in analogy to the SVD decomposition by assigning

$$U_{m\times m} = Q_{m\times m} \tag{2.172}$$
$$D_{m\times n} = \text{diag}(R_{m\times n}) \tag{2.173}$$
$$V_{n\times n} = D^{-1}_{n\times m} R_{m\times n} P^{\dagger}_{n\times n}. \tag{2.174}$$

Finite temperature BSS

The stabilization is performed during the sampling after a certain number of Green function wraps. The interval can be chosen freely, and is set as a multiple of the Trotter discretization time $\Delta_{\text{stab}} = N_{\text{stab}}\Delta\tau$. The implementation of the stabilization then relies on the successive application of Eq. (2.170) to the propagators [24, 25, 30],

$$B_{\boldsymbol{s}}(2\Delta_{\text{stab}}, \Delta_{\text{stab}}) \underbrace{B_{\boldsymbol{s}}(\Delta_{\text{stab}}, 0)}_{U_1 D_1 V_1} = \underbrace{((B_{\boldsymbol{s}}(2\Delta_{\text{stab}}, \Delta_{\text{stab}})U_1)D_1}_{U_2 D_2 V} V_1 = U_2 D_2 V_2, \tag{2.175}$$

where $V_2 = V V_1$. Iterating this stabilization procedure we can rewrite the Green function at time $\tau = n\Delta_{\text{stab}}$ as

$$B_{\boldsymbol{s}}(\tau, 0) = U_R D_R V_R \tag{2.176}$$
$$B_{\boldsymbol{s}}(\beta, \tau) = V_L D_L U_L \tag{2.177}$$
$$\begin{aligned} G_{\boldsymbol{s}}(\tau,\tau) &= (1 + B_{\boldsymbol{s}}(\tau, 0) B_{\boldsymbol{s}}(\beta, \tau))^{-1} \\ &= (U_L)^{-1} (\underbrace{(U_L U_R)^{-1} + D_R (V_R V_L) D_L)}_{UDV})^{-1} U_R^{-1} \\ &= (V U_L)^{-1} D^{-1} (U_R U^{-1}). \end{aligned} \tag{2.178}$$

In this expression both the left and right matrix products are of unit scale, and only the diagonal matrix D contains the now separated scales of the Green function. During the sampling process the matrices $U_R, D_R, V_R, V_L, D_L, U_L$ are stored in memory such that they can be used again after the sweep direction has been reversed.

Projective scheme BSS

The stabilization at zero temperatures works very similar to the finite temperature one. The difference is that the stabilized Green function may be computed entirely from the unitary matrices U_L and U_R [16, 24, 25],

$$B_{\boldsymbol{s}}(\tau, 0)P = U_R D_R V_R \tag{2.179}$$

$$P^\dagger B_{\boldsymbol{s}}(\Theta, \tau) = V_L D_L U_L \tag{2.180}$$

$$\begin{aligned} G_{\boldsymbol{s}}(\tau, \tau) &= 1 - B_{\boldsymbol{s}}(\tau, 0)P \left(P^\dagger B_{\boldsymbol{s}}(\Theta, 0)P\right)^{-1} P^\dagger B_{\boldsymbol{s}}(\Theta, \tau) \\ &= 1 - U_L (U_R U_L)^{-1} U_R. \end{aligned} \tag{2.181}$$

Since the scale dependent diagonal matrix D drops out, the projective scheme is numerically very stable.

Stabilization in LCT-INT

The stabilization in the LCT-INT is again very similar to the BSS algorithm. It uses the same Green function representation, although the efficient sampling routine requires an additional basis transformation (see Section (2.5.4)). Since the LCT-INT is formulated as a continuous time expansion, the stabilization interval is not related to any imaginary time discretization. Rather, we define stabilization blocks of arbitrary length Δ_{stab}. For each stabilization block, one keeps matrices analogous to Eqs. (2.177, 2.180) in memory. To recompute the Green function at an arbitrary time τ within the n-th stabilization block, i.e. $\tau \in [n\Delta_{\text{stab}}, (n+1)\Delta_{\text{stab}}]$, we compute [17, 18]

$$B_{\mathcal{C}}(\tau, n\Delta_{\text{stab}}) U_n D_n V_n = U_R D_R V_R \tag{2.182}$$

$$V_{n+1} D_{n+1} U_{n+1} B_{\mathcal{C}}((n+1)\Delta_{\text{stab}}, \tau) = V_L D_L U_L. \tag{2.183}$$

Afterwards we can calculate the stabilized Green function analogous to Eq. (2.178, 2.181). Once we wrap into a new stabilization block, the corresponding stabilization matrices are updated and stored in memory for the backwards sweep.

2.7 Sign problem

The sign problem is ultimately related to the fact that the eigen basis of the Hamiltonian is not known during the simulation (otherwise one could sample the trace over the density matrix in the eigen basis and calculate the Boltzmann factors directly). But of course if we knew the eigen basis of the interacting system, the problem would already be solved. For generic decompositions of the partition function there is no guarantee that each contribution is positive, which is a necessary condition to interpret the weight function as a statistical probability. A naive solution is to interpret only the absolute values of the weight function as probabilities. This however leads to statistical fluctuations that scale with the inverse average of the sign. It is difficult to make general statements about the occurrence of the sign-problem because for any given system an unknown decomposition that guarantees positivity might exist. In this sense the sign problem cannot be solved numerically in an efficient way, but it may be circumvented all together by an appropriate algorithm.

The $t - V$ model in particular, sign-problem-free formulations based on the fermion-bag idea have been found only relatively recently [23] compared to the spinful Hubbard model. Note that both models are only without sign problem at half-filling, because the respective algorithms rely on the explicit particle-hole symmetry of the Hamiltonian. After the discovery of the first sign-problem-free formulation of the $t - V$ model, the scope of related models without sign problem has been further expanded by formulations based on the split-orthogonal group [31] as well as majorana fermions [32, 33].

Chapter 3

Thermal Ising transitions in the vicinity of quantum critical points

In this chapter, I focus on the phase transitions of the honeycomb $t-V$ model (cf. section 1.3), which is a reduction of the full graphene model to spinless fermions and local interactions. Nevertheless, the universal behavior at the quantum critical point (QCP) of this model is characteristic for Hubbard-like models with relativistic dispersion relations, and is captured by the Gross-Neveu-Yukawa (GNY) theory [34, 8, 35]. In contrast to the conventional ϕ^4-theory, which describes the phase transition underlying the spontaneous breaking of a $O(N)$ symmetry, in the GNY theory the Dirac spinors couple to the order parameter field of the spontaneously broken $O(N)$ chiral symmetry. One therefore obtains a set of chiral universality classes, which are distinct from their regular counterparts without fermionic degrees of freedom.

I provide a discussion about the notion of scaling in the vicinity of a quantum critical point, with special attention given to the interplay of quantum and thermal fluctuations, as well as the thermal phase diagram. To this extent, I follow up on my Master thesis project [36], which contains a similar discussion for the quantum Ising model, as well as a preliminary investigation of the $t-V$ model. As part of my doctoral studies I have refined and significantly expanded on the data and analysis for the $t-V$ model, such that I include this part of the project also in this thesis. Finally, the encountered problems related to the extraction of critical exponents will serve as a basis for further analysis from different perspectives in later chapters. The results of this chapter have been published in Ref. [1]. I performed the quantum Monte Carlo simulations and the associated data analysis, and created the figures, while Stefan Wessel has directed the investigation.

3.1 Critical scaling in the thermal and quantum regime

The insulating ground state of the $t-V$ model exhibit longe-range order, which spontaneously breaks the Z_2 chiral symmetry of the Dirac fermions, and is characterized by the formation of a charge-density-wave (CDW) phase. Since the broken symmetry is discrete, an extended symmetry-broken phase at finite temperatures is possible, in accordance with the Mermin-Wagner theorem for two-dimensional materials.

This extended long-range ordered phase is enclosed by a line of thermal phase transitions (see Fig. 3.1), which terminates at the QCP. At finite temperatures, the fermions decouple from the critical order parameter fluctuations, and the chiral symmetry of the Dirac fermions is restored by the thermal transition. By the general principles of dimensional reduction and universality [37], the thermal transitions are then of the classical two-dimensional Ising kind. This leads to the formation of two separate scaling regimes, which are governed by quantum and thermal fluctuations of the order parameter, respectively.

In the vicinity of the quantum critical point, the quantum fluctuations are enhanced and compete against the thermal fluctuations. Upon approaching the quantum critical point, this competition ultimately drives the ordering temperature to zero. Furthermore, the extent of the thermal scaling regime, i.e. the area of the phase diagram which is close to the thermal transition line and where the scaling exponents are those of the two-dimensional Ising model, shrinks to zero close to the quantum critical point. For small temperatures, the transition line itself, i.e. the ordering temperature $T_c(g)$ as a function of the dimensionless interaction parameter g, is expected to follow the asymptotic scaling form

$$T_c \propto |g - g_c|^{z\nu}, \tag{3.1}$$

where g_c is the critical interaction strength, z denotes the dynamical exponent and ν is the correlation length exponent for the order parameter in the quantum ground state. The phase boundaries of the thermal phase diagram are therefore constrained by the critical exponents of the quantum phase transition at zero temperature. Fig. 3.1

In the following, we perform simulations at finite temperatures of the $t - V$ model to establish the thermal phase diagrams. To this extent, we determine the ordering temperature $T_c(g)$, and verify that the thermal and quantum scaling regimes are distinct in their critical exponents. In particular, we determine the quantum critical exponent ν from the asymptotic scaling form in Eq. (3.1), as well as the anomalous exponent η from the scaling in the finite temperature regime above the quantum critical point. Note that the dynamical exponent z is fixed to one for the quantum phase transition because of the emergent Lorentz invariance of the effective action in the continuum limit [8]. Since the classical thermal transitions do not

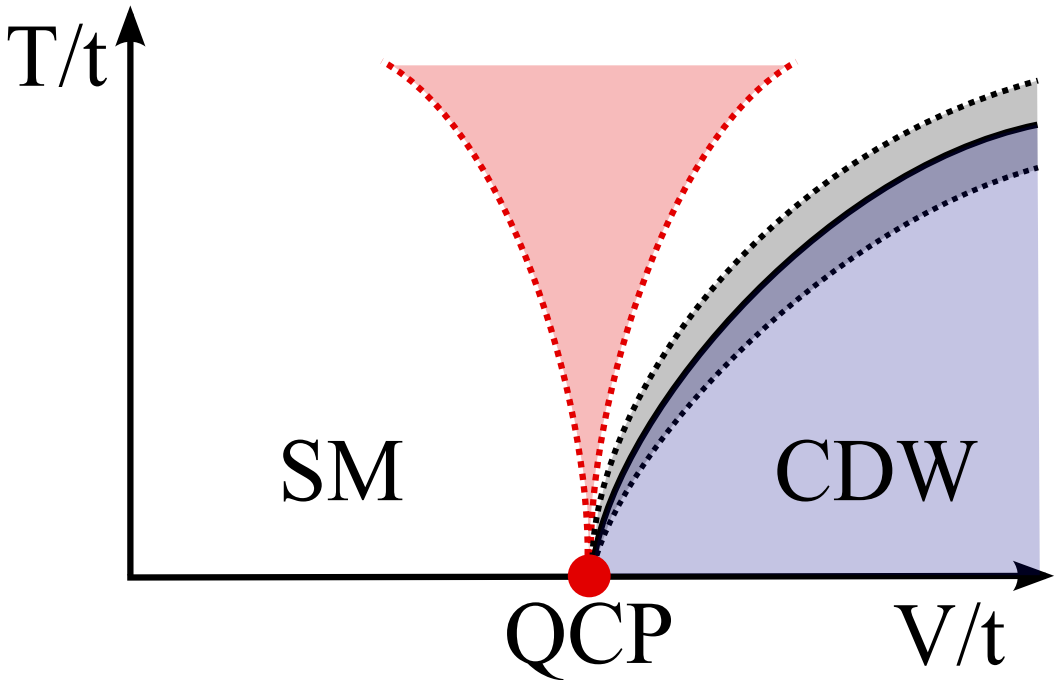

Figure 3.1: Sketch of the thermal phase diagram of the $t - V$ model. The quantum critical point separates the semi-metallic phase from the charge-density-wave (shaded in blue). The line of critical temperatures is indicated by a solid black line, and the associated thermal scaling regime is illustrated by the grey shaded region within the dotted lines. The quantum critical point is given by the red dot, and the associated quantum critical regime is illustrated by the red shaded region.

have an equivalent notion of imaginary time, their corresponding dynamical exponent can be set to zero.

3.2 Honeycomb $t - V$ model

3.2.1 Model definition

Here we investigate the $t-V$ model of spinless fermions on the honeycomb lattice, described by the Hamiltonian (cf. section 1.3)

$$H = -t \sum_{\langle i,j \rangle} \left(c_i^\dagger c_j + c_j^\dagger c_i \right) + V \sum_{\langle i,j \rangle} \left(n_i - \frac{1}{2} \right) \left(n_j - \frac{1}{2} \right), \tag{3.2}$$

$$\tag{3.3}$$

where $c_i^\dagger$ (c_i) creates (annihilates) a spinless fermion on the i-th lattice sites, and $\langle i, j \rangle$ indicates a summation over the set of nearest neighbor bonds of the honeycomb lattice. The

interaction term is written to be particle-hole symmetric form at half-filling – additionally we set the chemical potential to zero, i.e. $\mu = 0$, which guarantees half-filling.

The simulations are carried out using the CT-INT quantum Monte-Carlo algorithm described in chapter 2, augmented with the worm sampling technique to efficiently sample the fourth moment of the order parameter, which is required for the calculation of the Binder ratio. We simulated lattices finite clusters of the honeycomb lattice with periodic boundary conditions and a rhombus torus shape. Importantly, we only considered lattices of linear size L and $N_s = 2L^2$ lattice sites, with L constrained to a multiple of 3. This guarantees that the Dirac points, which are essential to the low-energy description of the half-filled system, are included in the discretized reciprocal lattice. By considering only this type of lattice cluster we effectively reduce the finite-size impact caused by the momentum discretization.

Still, the QMC algorithms capable of simulating fermionic lattice models without sign problem are generally significantly less efficient than their spin model counterparts. We are therefore more restricted in the system sizes available to us, which inevitably limits the precision our analysis. Nevertheless, with the CT-INT algorithm we were able to access lattice sizes of up to $L = 21$ at temperatures down to $T \sim 0.1t$ in the vicinity of the quantum critical point.

3.2.2 Discussion of scaling behavior

In the following, we first focus on the thermal regime of classical scaling around the line of ordering temperatures $T_c(V)$. We employ standard finite-size scaling analysis to locate the critical temperature at a fixed value of the interaction $V > V_c$ in the ordered phase. Since the thermal critical region is characterized by the two-dimensional Ising model, we can make use of the Onsager solution [38] to obtain the exact values for critical exponents as $\nu_{2D} = 1$, $\eta_{2D} = 1/4$, and $\beta_{2D} = 1/8$. As mentioned above, at finite temperatures the phase transition is purely classical, and therefore the dynamical exponent is zero. Nevertheless, one may still define a dynamical exponent z_{MC}, which describes the phenomenon of *critical slowing down* in Monte Carlo simulations – in this case the time axis is given by the autocorrelation time between between Monte Carlo steps, and the critical exponent is implementation dependent. In our discussion of critical behavior, the dynamical exponent z therefore refers to the former definition.

The phase transition from the semi-metallic (SM) phase to the commensurate charge-density-wave (CDW) phase of the $t - V$ model is signaled by the staggered density, whose

n-th moment is given by

$$M_n = \left\langle \left(\frac{1}{N_s} \sum_i \left(n_{i,A} - n_{i,B} \right) \right)^n \right\rangle , \tag{3.4}$$

where the summation is over the number of unit cells and N_s denotes the number of lattice sites. A standard scaling analysis of Eq. (3.4) leads to the scaling ansatz

$$M_n = L^{-\frac{n}{2}\eta_{2\mathrm{D}}} f_{M_n}(t_r L^{1/\nu_{2\mathrm{D}}}), \tag{3.5}$$

which expresses the scaling of M_n in terms of the critical exponents $\nu_{2\mathrm{D}}$ and $\eta_{2\mathrm{D}}$, as well as the reduced temperature $t_r = \frac{T-T_c}{T_c}$ and the linear lattice dimension L.

A convenient quantity is given by the Binder ratio,

$$B = \frac{M_4}{M_2^2}, \tag{3.6}$$

whose scaling function

$$B = f_B(t_r L^{1/\nu_{2D}}) \tag{3.7}$$

does no longer depend on $\eta_{2\mathrm{D}}$. In the following, we compute the rescaled quadratic order parameter estimator $L^{\eta_{2D}} M_2$ and the Binder ratio B, at various values of the interaction and temperature. We aim to first determine the ordering temperature as function of the interaction, and then proceed with a discussion of the critical exponents of the chiral Ising quantum critical point.

Thermal phase diagram

The Binder ratio is often used to locate critical values at which a phase transition takes place, in particular, if the critical exponents for the phase transition are not known. To do so, one makes use of the fact that at the critical temperature ($t_r = 0$), the leading scaling form in Eq. (3.7) becomes independent of L, and the finite-size data of B^Q for different system sizes intersect at the critical temperature. In the same fashion, for M_2^Q the intersection at $T = T_c$ occurs for the appropriately rescaled data $L^{\eta_{2D}} M_2^Q$. However, corrections to this leading finite-size scaling form may cause a systematic drift in the crossing points. One thus obtains a sequence of crossing points for successively larger system sizes, which converges to the true value of the critical temperature in the limit of large system sizes.

As an exemplary demonstration of our analysis, we present the results of this analysis for the interaction value $V = 1.75t$ in Fig. 3.2. We find that i) the crossing points shift their location with varying system size, ii) the Binder ratio and the scaled order parameter converge

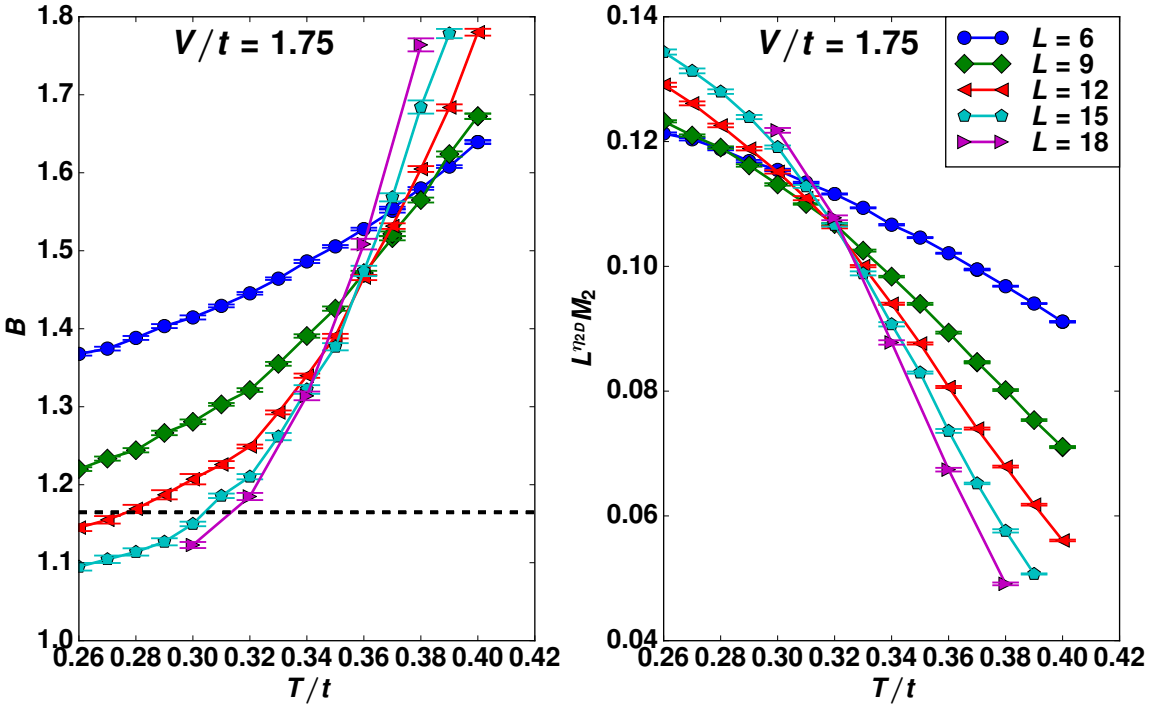

Figure 3.2: Finite size data for B (left panel) and $L^{\eta_{2D}} M_2$ (right panel) for the spinless fermion $t - V$ model at $V/t = 1.75$ in the critical region of the thermal Ising transition. The dashed line indicates the value of the critical Binder ratio for the Ising model on the honeycomb lattice. Figure reprinted from [1].

to the true critical temperature from opposite sides, iii) the scaled order parameter generally shows faster convergence than the Binder ratio, and finally, iv) the finite-size corrections grow larger upon approaching the critical interaction strength. Furthermore, due to the increased numerical cost of the fermionic quantum Monte-Carlo algorithm, we are restricted to rather small system sizes. Because the small number of data points makes the extrapolation of the crossing point sequence somewhat unreliable, we estimate the error on the critical temperature based on the interval between data points in which the true crossing point lies, also taking the aforementioned lower and upper bounds from the two quantities into account. In the case of $V = 1.75t$, we estimate the critical temperature as $T_c = 0.325(10)t$. The same analysis is repeated for other values of V to determine the line of ordering temperatures which encircles the charge-density-wave phase.

We may additionally verify the universality of the critical Binder ratio. Based on universality, one anticipates that the true crossing point, i.e. the Binder ratio $B(V_c)$ exactly at the critical temperature, takes on a value that is universal modulo lattice parameters such as the aspect ratio and unit cell shape. In the left panel of Fig. 3.2 the value of the critical Binder ratio $B_c = 1.1645157(3)$ is indicated by a dashed line, and has been obtained by classical

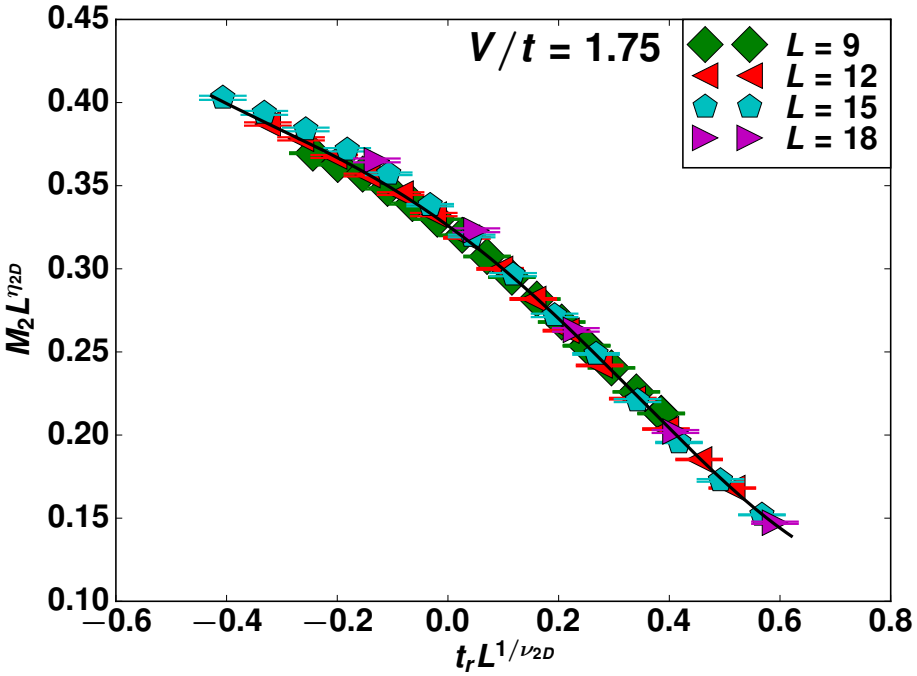

Figure 3.3: Data collapse plot of the data for M of the $t - V$ model at $V/t = 1.75$. The line denotes the expanded scaling function. Figure reprinted from [1].

Monte-Carlo simulations of the Ising model on the triangular lattice at the critical temperature $T_c = T_c = 1.5186519J$ [39–41]. We find that in our simulations of the $t - V$ model, the Binder ratio crossing points still lies above this value, although the trend is downward for the larger system sizes.

To supplement the crossing point analysis, we also performed the data collapse analysis based on Eq. (3.5) for M_2. Even though the scaling functions f_{M_2} is unknown, their shape can be inferred by plotting $M_2 L^{\eta_{2D}}$ against the argument of the scaling functions $t_r L^{1/\nu_{2D}}$. In this type of analysis the free parameters T_c, ν_{2D} and η_{2D} are chosen such that each curve of separate L collapses onto a single line, which then traces the scaling function. Of course in this specific case, the critical exponents $\nu_{2D} = 1$ and $\eta_{2D} = \frac{1}{4}$ are known exactly – this leaves the critical temperature as the only free parameter.

The results of this analysis for $V = 1.75t$ are shown in Fig. 3.3. The scaling function is formally expanded up to forth order in its argument and we use the Levenberg-Marquardt scheme to fit the finite-size data to the scaling ansatz. The error on the fit parameters are calculated using a bootstrapping procedure. In our approach we make the assumption that i) the system size is sufficiently large to justify the asymptotic scaling form, and ii) the reduced temperatures are not too large, i.e. the condition $|t_r| L^{1/\nu} \ll 1$ should be fulfilled. In practice, the latter condition is often somewhat relaxed with reasonable agreement up to $|t_r| L^{1/\nu}\, O(1)$.

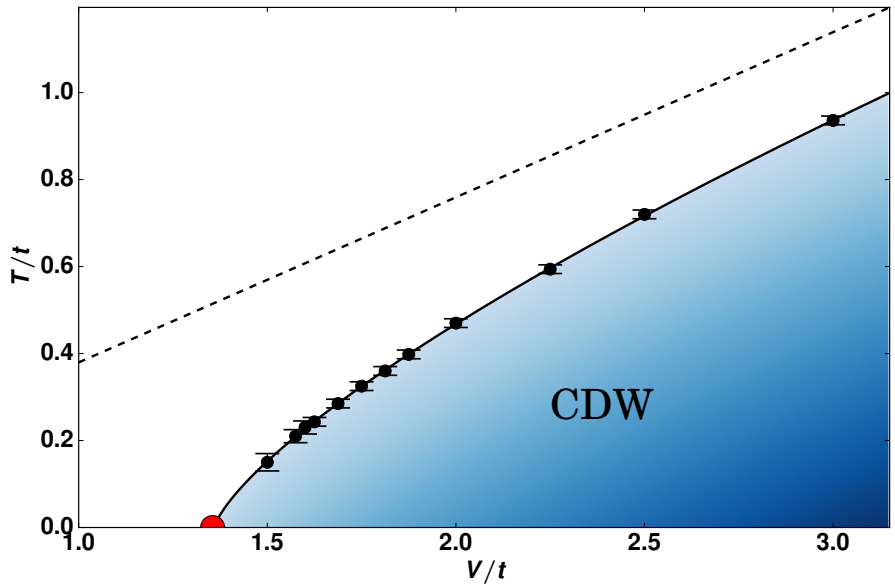

Figure 3.4: Thermal phase diagram of the spinless fermion $t - V$ model on the honeycomb lattice. The solid line is a fit of the numerical data to the scaling from from Eq. (3.1). Figure reprinted from [1].

We find that the rescaled data points yield a satisfactory collapse, even though minor corrections to scaling are noticeable. The extracted estimate for the critical temperature is $T_c/t = 0.315(20)$, which is in agreement with the previous estimate of the crossing point analysis. Moreover, we verified that upon rescaling the argument, the fitted scaling function can be mapped onto the scaling function of the finite-temperature transition in the quantum Ising model. This is another prediction of scaling theory, and demonstrates the two-dimensional Ising universality of the thermal transitions in both models.

To conclude this section, we summarize the results of the crossing point and data collapse analysis in the thermal phase diagram of the $t - V$ model, which is illustrated in Fig. 3.4. We have verified that the onset of the CDW at finite temperatures is signaled by a thermal phase transition of the two-dimensional Ising universality class, and in the following we will work to provide estimates for critical exponents of the chiral Ising quantum critical point.

Critical exponents

After the construction of the aforementioned thermal phase diagram, we proceed to analyze the scaling of the critical ordering temperature in respect to the asymptotic scaling form of Eq. 3.1. To do so, we leave both the critical interaction V_c as well as the critical exponent ν as free parameters, while the relativistic invariance of the Gross-Neveu-Yukawa theory

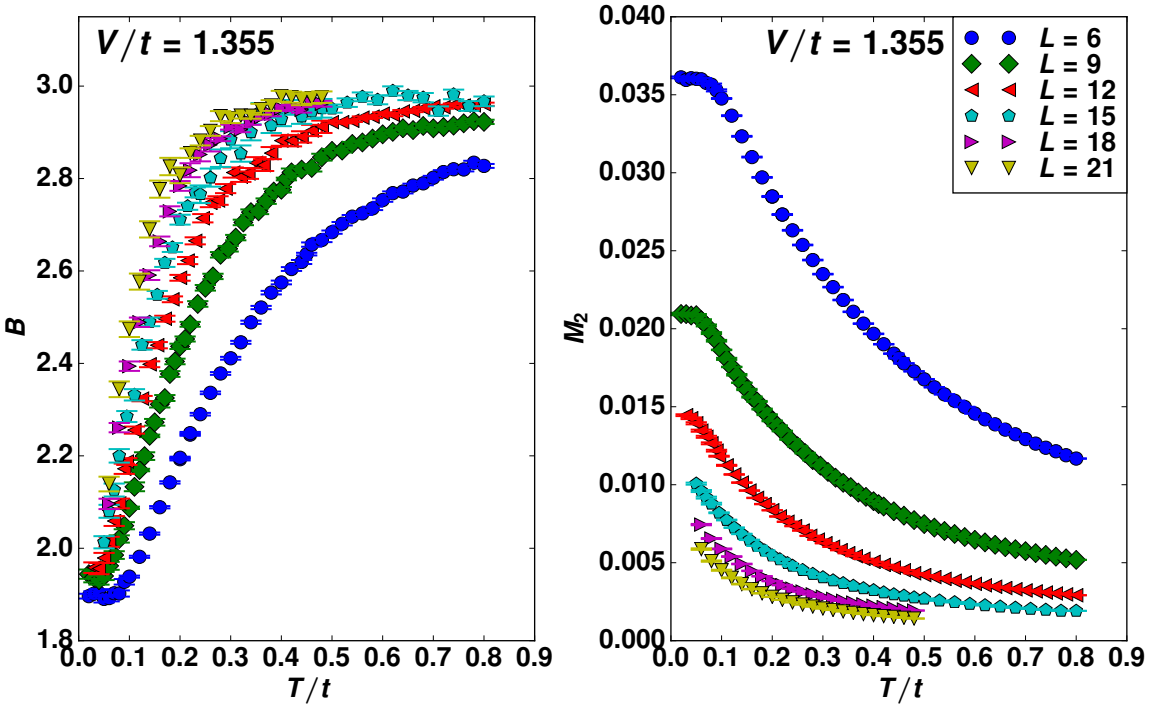

Figure 3.5: Finite-temperature data for B (left panel) and M_2 (right panel) for the spinless fermion $t - V$ model at $V/t = 1.355$, atop the quantum critical point, for various system sizes. Figure reprinted from [1].

fixes the dynamical exponent as $z = 1$. The best fit is then achieved by a critical interaction strength of $V_c = 1.359(30)$ and correlation length exponent $\nu = 0.74(4)$. The uncertainties on these parameters are obtained by the Bootstrap method. We note that there is the additional systematic error on the critical exponent, which is caused by the corrections to the asymptotic scaling form. We performed the fit in the range $(g - g_c)/g_c = (V - V_c)/V_c \lesssim 1$, for which we find a chi-square value of $\chi^2/\text{d.o.f.} \sim O(1)$. The drift on the exponent value is therefore already masked by the errors on the individual data points. Moreover, the bootstrapped error from the fit is larger than the 5% systematic error we observed for the quantum Ising model for this fitting range (cf. Ref. [1]). Finally, we briefly compare with the results of previous ground-state Monte-Carlo studies (cf. Section 3.3 for more details): the authors of Refs. [22, 18] report values of $V_c = 1.356(1)t$ and $\nu = 0.80(3)$, while in Ref. [33] values of $V_c = 1.355(1)$ and $\nu = 0.77(3)$ were reported. We find that our values are consistent with both of these results, and conclude that the underlying chiral Ising quantum critical governs the ordering transition to the CDW phase also at finite temperatures to such a degree, that the anticipated scaling regime is within grasp of our numerical simulations.

As mentioned in Section 3.1, the scaling regime of the quantum critical point extends to finite temperatures (cf. Fig. 3.1). We may therefore evaluate the scaling ansatz of the order

parameter in the proximity of the quantum critical point as

$$M_2 = L^{-z-\eta} f_{M_2}\left(\frac{V-V_c}{V_c} L^{1/\nu}, TL^z\right) \tag{3.8}$$

$$\xrightarrow{V\to V_c} L^{-z-\eta}\hat{f}_{M_2}\left(TL^z\right). \tag{3.9}$$

In the same fashion, the appropriate scaling ansatz for the Binder ratio is given by

$$B = f_{M_2}\left(\frac{V-V_c}{V_c} L^{1/\nu}, TL^z\right) \tag{3.10}$$

$$\xrightarrow{V\to V_c} \hat{f}_B\left(TL^z\right). \tag{3.11}$$

To explore the scaling in this so-called quantum critical fan, we therefore generate data at finite temperatures up to $T \approx t$ directly on top of the quantum critical point at $V = V_c \approx 1.355t$. For larger temperatures one eventually enters a cross-over regime to non-universal behavior, which is decoupled from the quantum critical CDW order parameter fluctuations that govern the quantum critical fan. The data of this finite temperature line atop the quantum critical point is illustrated in Fig. 3.5, in which the left and right panels show the Binder ratio and the order parameter M_2, respectively.

The scaled quantities B and $M_2 L^z$ are shown in Fig. 3.6. Based on Eq. (3.11), we anticipate that the Binder ratio is asymptotically invariant under length scale transformations at $V = V_c$, i.e. as a function of TL^z it should collapse for all values of L modulo corrections to the asymptotic scaling form. Indeed, we find all system sizes produce a decent collapse, although small deviations due to corrections to scaling can still be observed. Nevertheless, the overall quality of the collapse indicates the validity of the ansatz in Eq. (3.11), and the underlying assumption that the available temperatures are sufficiently small for the considered system sizes. Additionally, we can verify our assumption of $z = 1$ by treating z as a free parameter, and performing a fit based on Bayesian inference [42]. For the Binder ratio, this fit results in an estimate for the dynamical exponent of $z = 0.99(1)$. To provide meaningful errors on the fit parameters we employ a combination of bootstrap sampling and a variational choice of fitting parameters such as initial conditions and minimal system size. The minimization problem of the log-likelihood function is solved numerically with the standard Newton conjugate gradient algorithm.

In the same fashion, we perform a fit for the order parameter, now treating $z = 1$ as fixed and leaving the anomalous exponent η as a free parameter. A Bayesian fit up to $TL^z/t \lesssim 4$, which is approximately the region of decent collapse for the Binder ratio, provides the estimate $\eta = 0.255(10)$. However, it is difficult to find an objectively best collapse, because as one changes η, some parts of the curve collapse, while other parts deviate. Clearly,

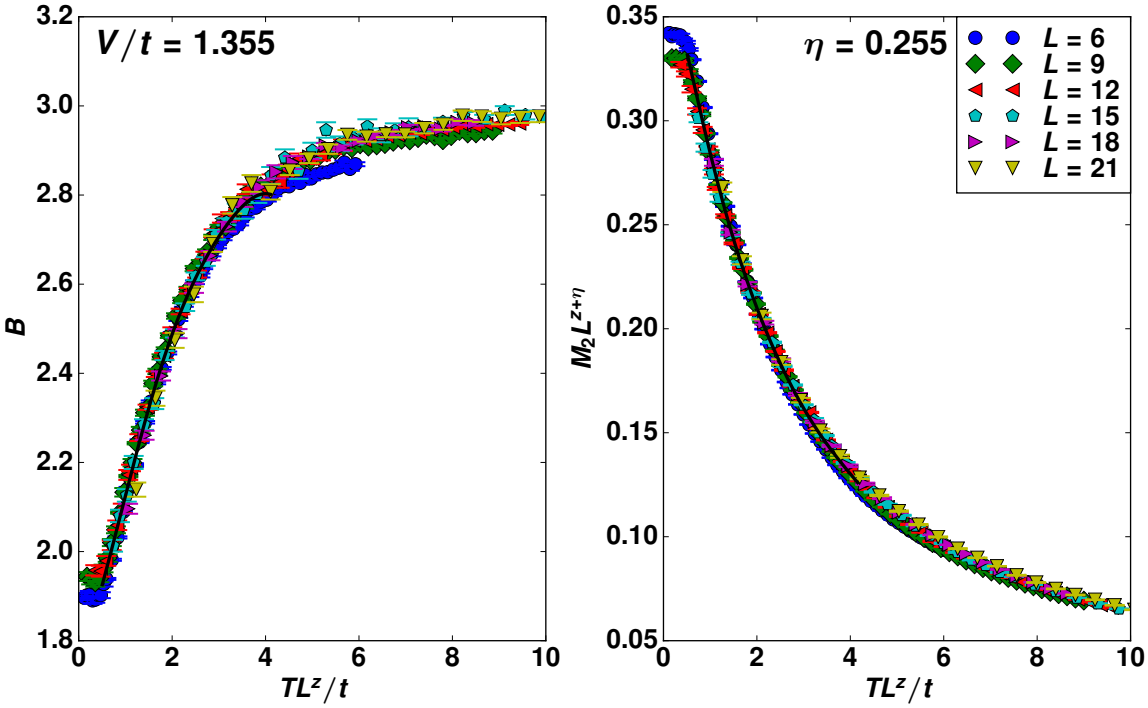

Figure 3.6: Data collapse of the finite temperature data for B (left panel) and M_2 (right panel) for the spinless fermion $t - V$ model at $V/t = 1.355$, atop the quantum critical point, for various system sizes. A value of $\eta = 0.255$ was used in the right panel, and $z = 1$. Figure reprinted from [1].

finite-size corrections are still present for the considered system sizes. Furthermore, one has to remember that corrections to scaling are expected to cause staggered deviations to the collapse, and that forcing a collapse for limited system sizes could potentially give misleading results. For this reason, one would ideally require the data to collapse using system sizes of different order of magnitude. Unfortunately, in our case, this check is unavailable to us because of the high numerical cost of simulating significantly larger lattices.

To get a better overview of the potential range for η, we also perform M_2 collapses based on previous estimates of η, which were based on ground state QMC simulations. In Refs. [22] and [18] a value of $\eta = 0.307(2)$ was obtained from simulations with L up to 18, while in Ref. [33] a value of $\eta = 0.45(2)$ with system sizes of up to $L = 24$ was reported. To check the consistency with our finite temperature data of the quantum critical regime, we fix the anomalous exponent to the respective values $\eta = 0.3$ and $\eta = 0.45$, and show the resulting collapse in the left and right panels of Fig. 3.7. We find that up to values of $\eta = 0.3$, there is still a reasonable good collapse up to $TL^z \approx 2t$, while for larger values the curves start to drift apart. In particular, the value of $\eta = 0.45$ seems to be too large, as the deviations are not in line the collapse of the Binder ratio.

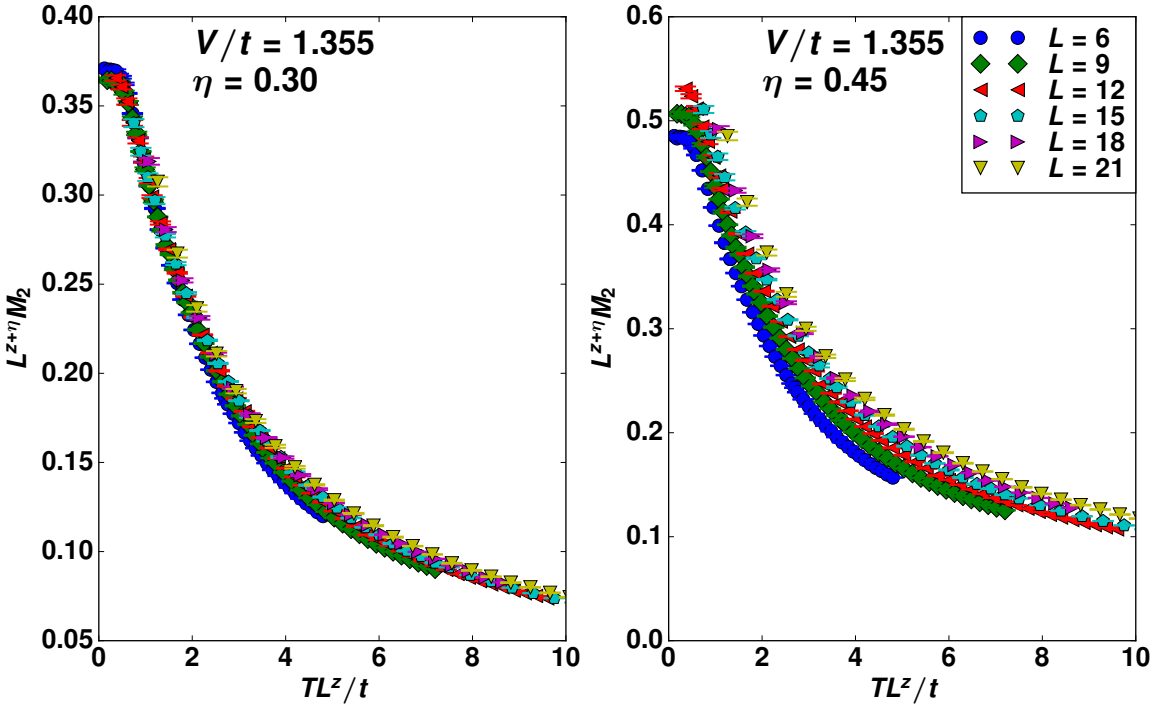

Figure 3.7: Attempted data collapse of the finite temperature data M_2 for the spinless fermion $t-V$ model at $V/t = 1.355$, atop the quantum critical point, for various system sizes with $\eta = 0.3$ (left panel) and $\eta = 0.45$ (right panel), and $z = 1$. Figure reprinted from [1].

To conclude this analysis, we choose our final estimate of η such that the collapse of the scaled order parameter reaches approximately the same quality as the collapse of the Binder ratio, which was entirely independent of η. By this logic, we arrive at a final value of $\eta \approx 0.25 - 0.3 = 0.275(25)$. Finally, and on a more qualitative account, we note that for the $t-V$ model the scaling function $\tilde{f}$ does not exhibit a local maximum (cf. the right panel of Fig. 3.6), in contrast to what was observed for the corresponding scaling function of the quantum Ising model (cf. Ref. [1]). This observation provides a direct qualitative distinction of the two different universality classes at the corresponding quantum critical points.

3.3 Discussion of critical exponents

To conclude this chapter about the thermal transitions near a quantum critical point, I want to briefly summarize our results and discuss them in the context of other publications. In the previous sections, we employed quantum Monte Carlo simulations for the $t-V$ model to map out the thermal phase diagram, and we investigated the scaling behavior in both the critical thermal regime and the quantum critical regime. The critical exponents for the

Method	ν	η
$4-\epsilon$, 1st order [12]	0.709	0.577
$4-\epsilon$, 2st order [12]	0.797	0.531
FRG (linear cutoff) [43, 44]	0.927	0.525
FRG (exp. cutoff) [44]	0.962	0.554
FRG [45]	0.929	0.602
$1/N$ expansion [43]	0.738	0.635
CT-INT (GS) [22]	$0.80(3)$	$0.302(7)$
M-QMC (GS) [32, 33]	$0.77(3)$	$0.45(2)$
LCT-INT (GS) [18]	$0.80(3)$	$0.302(7)$
Fermion Bag (GS) [46]	$0.88(2)$	$0.54(6)$
CT-INT ($T>0$), here	$0.74(4)$	$0.275(25)$

Table 3.1: Overview of reported estimates for the critical exponents ν and η for the $N_f = 1$, Z_2-Gross-Neveu theory in 2+1 dimensions (analytic approaches) as well as the spinless fermion $t-V$ model on the honeycomb lattice (QMC approaches). GS indicates that ground state correlations were targeted, while the results reported here (in the last row) were obtained from the finite-temperature scaling. Note, that for the LCT-INT (linear CT-INT) method, with system sizes up to $L = 18$ the values of Ref [22] (with L up to 15) were used and checked for consistency, but no independent finite-size analysis was performed. In the M-QMC (Majorana QMC) approach of Ref [18], system sizes up to $L = 24$ were employed.

thermal regime were given by those of the two-dimensional Ising model – they are of course well known from the exact Onsager solution to be $\nu_{\text{2D}} = 1.0$ and $\eta_{\text{2D}} = 0.25$. We verified the correctness of the scaling ansatz with these exponents in the thermal regime, and used them to determine the ordering temperatures.

The critical exponents of the quantum critical points are more elusive. The fermionic degrees of freedom significantly increase the numerical complexity of the simulations, such that only small lattices were available to us. This not only increases the risk of systematic errors due to finite-size corrections to scaling, but also decreases the quality of the data, i.e. the Monte-Carlo error bars become larger. Nevertheless, our result for the correlation length exponent is in decent agreement with previous results, which are summarized in Table 3.1 and include results from both numerical simulations and analytic calculations. However, for the anomalous exponent η the results are less satisfying. In this case, the analytic approaches mostly agree on a value around $\eta \approx 0.55$, however the numerical approaches provide a significantly smaller value, the closest one being the value $\eta = 0.45(2)$ from Ref. [32, 33]. Of course, the disagreement already within the different quantum Monte Carlo works is particularly disappointing, and points to potential finite-size effects. Furthermore, after the publication of our findings, new Monte Carlo results have been reported that seem to confirm the necessacity for very large lattices [46]. In our analysis, we based the estimate for η on

the assumption that the collapse of the scaled order parameter should have approximately the same corrections to scaling as the Binder ratio. We have verified this assumptions for the quantum Ising model as well, however, it is possible, that unforeseen correction terms appear in the scaling ansatz for the $t - V$ model.

Finally, it should be noted that disagreement of various methods in regards to critical exponents is not unique to the chiral Ising universality class. For the chiral Heisenberg universality, similar disagreements have emerged in recent years [47, 48]. Of course it would the desirably to overcome these discrepancies by pursuing higher orders of the ϵ-expansion, and by simulating larger lattices by using novel Monte-Carlo techniques [46]. Alternatively, one could think of different quantifiers, that characterize the universality classes. This is exactly the motivation for the torus spectroscopy, which is detailed in Chapter 4. It provides both a qualitative and quantitative characterization of quantum critical points, and has already been applied to the quantum Ising model in Ref [49]. In Chapter 4, we will extend this work to the chiral Ising universality class by analyzing the torus spectrum of the $t - V$ model.

Chapter 4

Torus spectroscopy of the Gross-Neveu-Yukawa quantum field theory

In this chapter I provide a discussion of the torus spectroscopy analysis of the free Dirac and chiral Ising fixed points of the Gross-Neveu-Yukawa quantum field theory. Both of these fixed points are realized as the low-energy effective theory of the $t - V$ lattice model, in the weak-coupling limit and at the critical interaction, respectively. In general, the critical torus spectrum of lattice models has been shown to serve as a fingerprint for the underlying quantum critical point, and in this case it provides us with a universal characterization of the chiral Ising universality class. The torus spectroscopy can therefore be seen as an alternative method to the conventional characterization through universal critical exponents, which is discussed in more detail in Chapter 3 of this thesis. The numerical simulations for the spectroscopy analysis include exact diagonalization of small lattice clusters, as well as quantum Monte Carlo simulations for larger lattices. The results of this chapter have been published in Ref. [3] and Ref. [4]. The exact diagonalization has been carried out by Michael Schuler, while the quantum Monte Carlo simulations have been carried out by myself as part of this thesis. In addition, the results are contrasted with an ϵ-expansion calculation of the effective field theory, which has been performed by Seth Whitsitt. The figures have been created by Michael Schuler, Thomas Lang and myself. Andreas Läuchli and Stefan Wessel directed the investigations.

4.1 Torus spectra as universal fingerprints of critical points

While the critical exponents are in principal sufficient to distinguish the different universality classes, their precise calculation is often very challenging due to either their intricate finite size scaling in finite lattice approaches or because formally divergent series expansions require complicated resummation techniques up to high orders. Furthermore, even though the critical exponents physically express the emergent scale invariance at the critical point, a further qualitative discussion is often not possible. Take for example the classical three-dimensional Heisenberg and Ising universality classes. The respective critical exponents for the correlation length ν and the anomalous exponent η are given by [50, 51]

$$\nu_{\text{3D Ising}} \approx 0.630(1) \tag{4.1}$$

$$\eta_{\text{3D Ising}} \approx 0.036(1) \tag{4.2}$$

$$\nu_{\text{3D Heisenberg}} \approx 0.704(6) \tag{4.3}$$

$$\eta_{\text{3D Heisenberg}} \approx 0.028(2). \tag{4.4}$$

Even though the underlying physics of the respective models is totally different, the critical exponents do not convey this difference. In fact, for many universality classes the critical exponents are quite similar, with little to no qualitative difference. In addition, as alluded to above, they can be notoriously difficult to calculate to high precision, such that within the estimated uncertainty they match multiple universality classes (of course in practice one only considers universality classes that fit the symmetries of the model).

Another example is the chiral Ising universality class. In Chapter 3 we discussed the thermal phase diagram of the $t - V$ model, and proposed a scheme to extract the critical exponents of the chiral Ising quantum critical point from its finite temperature data. However, we found that the resulting critical exponents were partly inconsistent with previous estimates [52–56], with finite size scaling corrections being the most likely culprit. The chiral Heisenberg universality class is yet another example, for which a series of inconsistent critical exponents has been reported [47, 48, 55, 57].

In the following sections, we will investigate the torus spectroscopy method as an alternative classification tool, which provides both qualitative and quantitative signatures of the universality class. The main idea goes back to the concept of *state-operator correspondence*, which has been discovered in the context of conformal field theories. It describes a mapping between the exact scaling dimensions of the field theory in $\mathbb{R}^d$ and the Hamiltonian spectrum in radial quantization $S^{d-1} \times \mathbb{R}$ [58]. In particular, this correspondence is often used in the characterization of $1 + 1$-dimensional quantum critical points, the scaling dimensions of

which are then mapped to the energy eigenstates of a Hamiltonian on a circle. In higher dimensions $d > 2$ the correspondence is less practical, because the mapping involves a Hamiltonian which is defined on a curved surface geometry. However, numerical simulations are typically performed on lattices with periodic boundary conditions, which results in a flat torus rather than a curved spherical geometry.

Even though the eigenstates of the torus Hamiltonian no longer directly correspond to the exact scaling dimensions of a conformal field theory, the structure of the critical torus spectrum has been shown to be universal for Wilson-Fisher and selected topological phase transitions [49, 59, 60]. More precisely, the low-energy excitation at the critical point are expected to scale as

$$\Delta_i = E_i - E_0 = v\frac{\xi_i}{L^z}, \tag{4.5}$$

where E_i labels the energy of the i-th excited state, E_0 is the ground state energy, v is a non-universal constant, the ξ_i define a set of universal constants which are the torus equivalents of the scaling dimensions, L is the linear extent of the lattice and z is the dynamical exponent. In the special case of (emergent) Lorentz invariance at the critical point, the constant v takes on the meaning of an effective speed of light, and the dynamical exponent is fixed to $z = 1$. Importantly, the universal numbers $\{\xi_i\}$ are accessible by both numerical and analytic approaches, similar to the conventional critical exponents.

In the following, we will investigate the spectrum of the $t - V$ model, defined on regular finite-size tori, and determine its evolution when the Hamiltonian parameters are tuned to their critical values. Using the universal relation (4.5), we determine the universal torus spectrum for the free Dirac and chiral Ising fixed points of the Gross-Neveu-Yukawa theory, which are both realized by tuning the interaction of the $t - V$ model. The set of $\{\xi_i\}$ then provide a quantitative characterization of the universality classes, whereas the quantum numbers and degeneracies of the low-energy excitations allow for a more qualitative distinction. Combining both aspects, we propose the torus spectrum as a universal fingerprint of the universality class that underlies the critical point. As a side product of Eq. (4.5), we may use the dependence of the excitation energies on the effective velocity to compute the Fermi velocity renormalization, which will be the subject of section 4.6.

4.2 Models and torus compactification

We simulate the previously introduced $t-V$ model of spinless fermions on the honeycomb lattice at half-filling

$$H_{hc} = -t \sum_{\langle i,j \rangle} \left(c_i^\dagger c_j + \text{h.c.} \right) + V \sum_{\langle i,j \rangle} \left(n_i - \frac{1}{2} \right) \left(n_j - \frac{1}{2} \right), \tag{4.6}$$

where $\langle i,j \rangle$ denotes nearest neighbor bonds, $c_i^{(\dagger)}$ are fermionic annihilation (creation) operators at site i, and $n_i = c_i^\dagger c_i$ is the fermionic number operator. As discussed in previous chapters, this lattice models is described by a free Dirac semi-metal in the weak coupling regime, and may be tuned to a charge ordered insulator through a quantum phase transition of the chiral Ising kind. Alternatively, one may study spinless fermions on the π-flux square lattice at half-filling,

$$H_{sq} = -t \sum_{\langle i,j \rangle} \left(\mathrm{e}^{\mathrm{i}\theta_{ij}} c_i^\dagger c_j + \text{h.c.} \right) + V \sum_{\langle i,j \rangle} \left(n_i - \frac{1}{2} \right) \left(n_j - \frac{1}{2} \right), \tag{4.7}$$

where the flux per plaquette is given by $\phi = \sum_{\langle i,j \rangle \in \square} \theta_{ij} = \pi$. At criticality, this model also implements the chiral Ising universality class, and may be studied complementary to the $t-V$ model on the honeycomb lattice. In the following I will focus the discussion on the model in Eq. (4.6), and for the discussion of the π-flux model I refer to Ref. [3].

Both the free Dirac and the chiral Ising scaling can be understood as different fixed points of the Gross-Neveu-Yukawa (GNY) theory with a $n = 4$-component spinor (fermionic) field ψ coupled to a $\mathbb{Z}_2$ scalar field ϕ [8–10]. Its Lagrangian is given by

$$\mathcal{L}_{\text{GNY}} = -\overline{\Psi}^j \left(\not{\partial} + g_{\text{Y}}\, \phi \right) \Psi^j + \frac{1}{2} \phi \left(s - \partial^2 \right) \phi + \frac{\lambda}{4!} \phi^4 , \tag{4.8}$$

where Ψ^j is an n_{D}-component Dirac spinor with $j = 1, ..., N_f$ flavors, such that the total number of fermionic degrees of freedom is $N = n_{\text{D}} N_f$. The real scalar field is denoted by ϕ, and g_{Y} is the Yukawa coupling strength between the spinor and scalar fields. For more details on the Gross-Neveu-Yukawa field theory I refer to section 1.4.

The numerical simulations are performed on rhombic finite size clusters of linear extent L, which preserve the six-fold rotational symmetry C_6 of the honeycomb lattice. The torus structure arises from choosing periodic boundary conditions for the lattice clusters. The shape of the two-dimensional torus may be defined using complex coordinates, which is more convenient when working in the continuum limit. In the complex notation, the torus

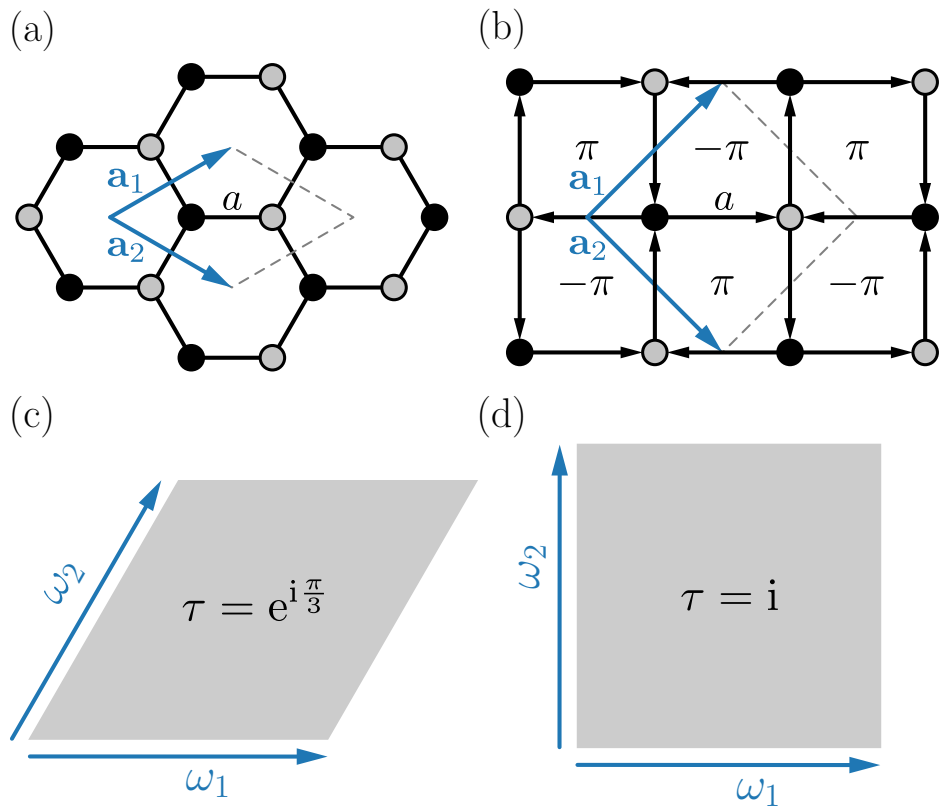

Figure 4.1: Illustration of (a) the honeycomb lattice, (b) the π-flux square lattice, and the two torus geometries with sixfold (c) and fourfold (d) rotational symmetry. The two sublattices A and B are indicated by black and gray points respectively. The lattice constant a is given by the distance between nearest neighbors, the lattice vectors $\boldsymbol{a}_1$ and $\boldsymbol{a}_2$ are indicated by the blue arrows, and the unit cell is traced by the grey dotted lines. Finite clusters with $N_s = 2L^2$ sites span L unit cells in the direction of $\boldsymbol{a}_1$ and $\boldsymbol{a}_2$ respectively, i.e., $|\omega_1| = |\boldsymbol{a}_1|L$, $|\omega_2| = |\boldsymbol{a}_2|L$. In (b) we have chosen a specific gauge where the thick bonds denote a phase of $\theta_{ij} = \pi$, whereas thin bonds denote $\theta_{ij} = 0$. Figure reprinted from [3].

coordinates are given by

$$x = x_1 + \mathrm{i}x_2, \tag{4.9}$$

and the periodic boundary conditions are encoded by complex periods ω_1 and ω_2, such the equivalence

$$x \sim x + n\omega_1 + m\omega_2 \tag{4.10}$$

holds for all $n, m \in \mathbb{Z}_2$. Then the torus is characterized by its modulus parameter

$$\tau = \frac{\omega_2}{\omega_1} = \tau_1 + \mathrm{i}\tau_2, \tag{4.11}$$

which for the honeycomb lattice is given by $\tau = \exp(\mathrm{i}\frac{\pi}{3})$ (see Fig. 4.1). The torus shape remains relevant in the thermodynamic limit and if properly taken into account, the universal numbers ξ will be a function of the torus modulus τ. However, in practice this dependence seems to be rather small (see Ref. [3] for further comparison between the results for the honeycomb lattice and square lattice).

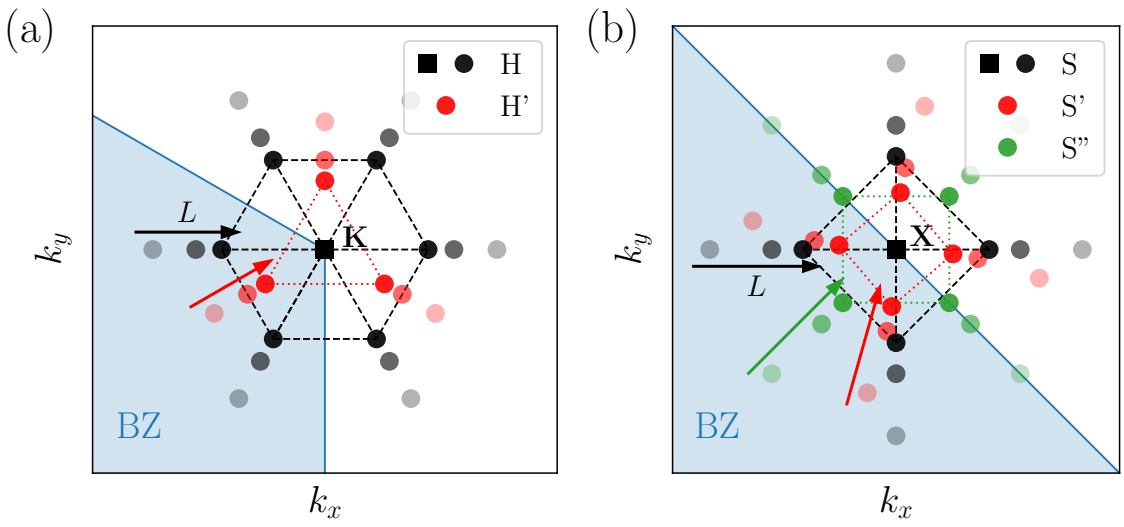

Figure 4.2: Illustration of the different finite-size cluster families for the (a) honeycomb, (b) square lattice. Shown is a zoom into the momentum space around one of the Dirac points $\mathbf{K}/\mathbf{X}$. The closest momentum points are plotted for clusters of different linear size L, and, as a guide to the eye, we have connected them by lines for the largest L shown. The Dirac points are (not) part of the momentum space for cluster families H/S (H'/S'/S"). See text and Ref. [3] for further details. Figure reprinted from [3].

Furthermore, one has to distinguish between different finite-size cluster families, which each have a different momentum structure around the Dirac points. For the honeycomb lattice, the cluster families are rather simple – one only has to distinguish between clusters that do (H) or do not (H') contain the Dirac point in their momentum discretization. The Dirac points $\boldsymbol{K}$ and $\boldsymbol{K}'$ are present if and only if the linear dimension of the lattice is divisible by three, i.e. $L \bmod 3 = 0$. For $L \bmod 3 = 1, 2$ the momenta next to the Dirac points form a triangle, and the Dirac points are located in its center (see Fig. 4.2). For the π-flux model on the square lattice the classification is more complicated because it depends on the chosen gauge of the flux. However, fundamentally the torus families can again be separation into one

that features the Dirac points, and others that do not. In quantum Monte Carlo simulations for graphene-like this distinction is already routinely made to reduce finite-size effects.

For our application, we are interested in the excitation gaps scaled with the linear lattice dimension according to Eq. (4.5), and taken in the thermodynamic limit. To clarify our notation, in the following we shall refer to the *finite size energy gap* of a system as the energy difference of an excited state to the ground state on a finite lattice of dimension L

$$\Delta_n(L) = E_n(L) - E_0(L). \tag{4.12}$$

where as the *energy gap* of a system refers to the same energy difference in the thermodynamic limit

$$\Delta_n = \lim_{L\to\infty} \left(E_n(L) - E_0(L)\right). \tag{4.13}$$

The torus spectrum is then defined by Eq. (4.5), and a *gap in the torus spectrum* is defined as

$$\xi_n = \lim_{L\to\infty} \frac{E_n(L)L}{v} > 0. \tag{4.14}$$

Going back to the different torus families, we find that the torus spectrum qualitatively changes if the cluster contains the Dirac points. In particular, the clusters without the Dirac point show a large gap in the half-filled sector of the torus spectrum for all values of the interaction – this even holds true for $V = 0$. In contrast, the clusters with the Dirac points display an interesting doubling of the energy levels – i.e. all levels in the torus spectrum are appear as degenerate or at least quasi-degenerate pairs.

4.3 Torus spectrum of the $t - V$ model

In this section I will present the results of the torus spectroscopy for the based on the methodology presented in section 4.5. In particular, the focus will be on the analysis of the torus spectrum of the $t - V$ model, which has been obtained from finite lattices. The connection between the torus spectrum of the lattice models and the torus spectrum of the fixed points of the underlying Gross-Neveu-Yukawa field theory is then subject of section 4.4.

We start our discussion with a detailed analysis of the spinless fermion $t - V$ model on the honeycomb lattice at half-filling, described by Eq. (4.6) (see section 1.2 for more details). As mentioned in the previous introduction of the torus spectrum, we are interested in the energy levels of the Hamiltonian, when it is defined on finite-size lattices. The torus spectrum is then obtained according to Eq. (4.5) by an appropriate rescaling with the linear dimension

$L = \sqrt{N_s/2}$ of the lattice cluster (assuming periodic boundary conditions). At this point we do not know the effective speed of light, i.e. in this case the renormalized Fermi velocity, and therefore we begin with an investigation of the quantity $\Delta_i \times L$. At a later point, we will provide an estimate for the Fermi velocity at the critical point, which will enable us to also determine the set of universal numbers $\{\xi_i\}$ for the chiral Ising fixed point.

4.3.1 Evolution with V

To provide a first insight into the structure of the torus spectrum, we perform an exact diagonlization (ED) of the Hamiltonian for small lattices. Because the dimension of the Hilbert space scales exponentially with the number of lattice sites, this method is limited to clusters of about 40 sites. As mentioned in section 4.2, the torus spectrum is sensitive to the lattice family, and in particular to the inclusion of the Dirac points. To increase the number of clusters, which both contain the Dirac points and are small enough to be accessible by ED, we study so called tilted clusters [61] in addition to the standard $L \times L$-type clusters. In these tilted clusters, we define the linear dimension as $L = \sqrt{N_s/2}$. The advantage of employing the exact diagonalization is that we have easy access to the full quantum numbers and degeneracies of the low-lying energy eigen states. Furthermore, the qualitative difference between the various cluster families can already be seen very clearly in the spectrum of small lattices.

While the quantitative values of the energy eigenstates are subject to substantial finite-size corrections in the thermodynamic limit, the typical spectral features of the respective cluster types are already present on these small lattices. In the following analysis we investigate in particular the spectrum of the free system ($V = 0$), at the critical point ($V_c \approx 1.355t$), and the evolution of the spectrum between these two points. For interactions $V > V_c$, the system becomes a charge-density-wave in the thermodynamic limit and develops a finite gap above its two-fold degenerate ground state. We therefore expect the scaled torus spectrum to contain two degenerate ground states and otherwise divergent excited states in the Z_2 symmetry-broken phase.

The torus spectrum as a function of the interaction V is illustrated in Fig. 4.3, in which the left panel (a) shows the spectrum of a honeycomb cluster of type H (tilted with Dirac points), while the right panel (b) shows the spectrum of a honeycomb cluster of type H' (no Dirac points). The labels of the energy levels are chosen in analogy to the naming convention of operators in conformal field theories, in this case the Gross-Neveu-Yukawa field theory. In this sense, the we label with σ_T and ϵ_T the torus analogues of the lowest Z_2 odd and even scalar fields, and the lowest single-fermion excitation ψ_T is the torus analogue of the lowest vector field. The torus analogue of the fermionic descendent field, i.e. the lowest fermionic

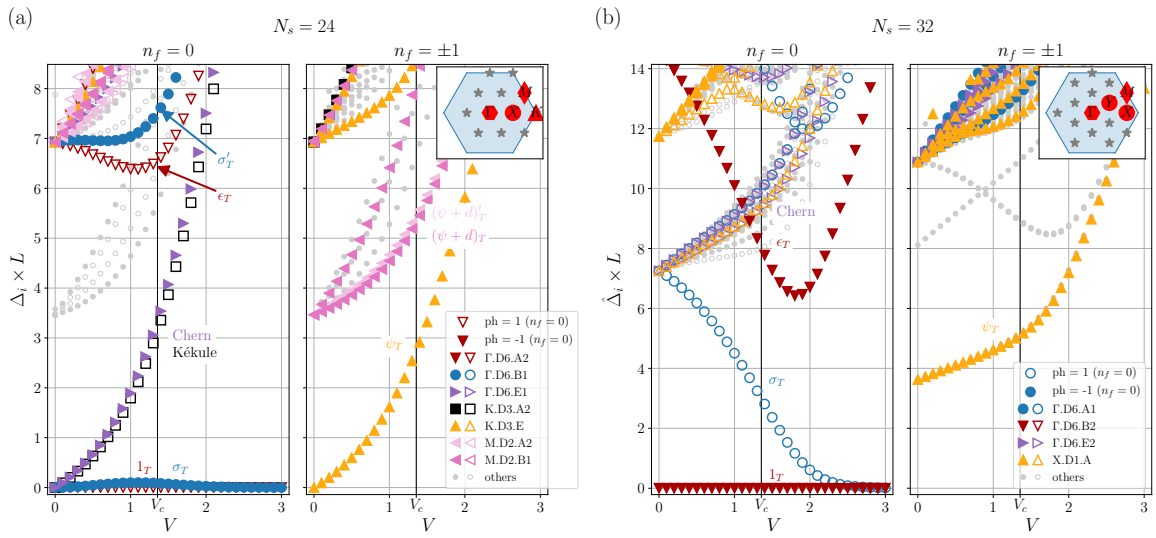

Figure 4.3: Low-energy spectra of the model Eq. (4.6) as a function of V for clusters of size (a) $N_s = 24$, (b) $N_s = 32$. The left panels show the half-filled sector $n_f = 0$, the right panels show the sectors with one additional fermion/hole $n_f = \pm 1$. The black vertical line indicates the critical point $V_c \approx 1.355t$ [22, 52]. The cluster in (a) has the Dirac point in its momentum space (family H) and the fermionic excitation (right panel) is gapless for $V = 0$. The cluster in (b) does not feature the Dirac point (family H') and the fermionic excitation is always gapped. This influences the spectrum at criticality such that different families of clusters have to be distinguished in the extrapolation to the TDL. We have also, in the corresponding colors, indicated the labels for the most important low-energy spectral levels: 1, σ_T, ϵ_T, ψ_T, Chern, Kekulé (see text). Empty (filled) symbols for $n_f = 0$ represent even (odd) levels under particle-hole inversion. Figure reprinted from [3].

excitation at $\mathbf{k}_{\text{min}}$, is denoted as $(\psi + d)_T$. Finally, primed levels refer to the next higher excitation in the symmetry sector of the unprimed level (in particular $\epsilon_T := 1'_T$).

Let us first focus on the cluster type H in the left panel. It shows the scaled low energy spectrum for the $n_f = 0$ (half-filled) and $n_f = \pm 1$ (one particle added/removed from half-filling). The spectrum for the particle-number sectors $|n_f| > 1$ can be obtained analogously, and due to the particle-hole symmetry of the Hamiltonian the spectrum of the $\pm n_f$ sectors are identical.

For the free Hamiltonian, we find that the $n_f = 0$ sector contains a 6-fold degenerate ground state. In Fig. 4.3(a) they are labeled as 1_T, σ_T, Kekulé (2-fold) and Chern (2-fold). These labels are chosen to relate the energy states to the known instabilities of the Dirac phase – a mass term for spinless Dirac fermions can be generated by breaking the sublattice symmetry (σ_T), by breaking the time-reversal symmetry with zero net magnetic flux through the honeycomb unit cell (Chern), or by a Kekulé dimerization which creates two distinct real masses [62–65]. In the single particle basis of the free system, these six states correspond

Levels	PH	I_x	n_f	$\mathbf{k}$	κ
$1_T, \epsilon_T$	1	1	0	0	0
σ_T, σ'_T	-1	-1	0	0	0
Kekulé	1	1	0	$\mathbf{K}$	0
Chern	-1	-1	0	0	0
ψ_T	–	–	± 1	$\mathbf{K}$	0
$(\psi + d)_T, (\psi + d)'_T$	–	–	± 1	$\mathbf{k}_{\min}$	1
$(2\psi)_T$	–	–	± 2	0	0

Table 4.1: Quantum numbers of the most relevant energy levels in the torus spectrum of the chiral Ising CFT. The table denotes the particle-hole quantum number PH, the fermion sector relative to half filling n_f, the momentum $\mathbf{k}$, and the reduced momentum κ [3]. For simplicity, we here omit showing the irreducible representations under the lattice point-group symmetry.

to the $\binom{4}{2}$ many-body states that occupy 2 of the 4 degenerate Dirac single particle levels. Similarly, we find an 8-fold degenerate ground state in the $n_f = \pm 1$ sector (ψ_T). In the single-particle picture, they are constructed by occupying either 3 ($n_f = 1$) or 1 ($n_f = -1$) of the Dirac levels, such that the total number of permutations is $\binom{4}{3} + \binom{4}{1} = 8$. Finally, the $n_f = \pm 2$ sector contains a two-fold degenerate ground state ($(2\psi)_T$, not shown in Fig. 4.3), which is constructed by occupying all Dirac levels ($n_f = 2$) or none ($n_f = -2$). The total degeneracy of the free ground state is therefore $6 + 8 + 2 = 16$.

For $V > 0$, the torus spectrum develops a gap – i.e. $\Delta_i \times L > 0$, however the system is still gapless in the sense that $\lim_{L\to\infty} \Delta_i = 0$ in the semi-metallic phase for $V < V_c$. However, the σ_T remains only slightly above the 1_T ground state – together they form a two-fold quasi-degenerate ground state manifold. For $V \gg V_c$ these are the states that form the classical charge-density-wave ground states. The charge-density-wave breaks both the Z_2 particle-hole and the Z_2 reflection symmetry I_x (cf. section 1.2) – we may therefore use either one to distinguish between the Z_2 odd (σ_T) and Z_2 even (1_T) ground state. Another interesting level is denoted by ϵ_T – it corresponds to the first excited state in the symmetry sector of the ground state (1_T). It corresponds to the detuning from the quantum critical point and exhibits characteristic minimum around the critical interaction. The quantum numbers of the various levels are summarized in Table 4.1.

Finally, let us briefly discuss the torus spectrum of H'-type clusters, i.e. clusters without Dirac points. Fig. 4.3(b) shows the torus spectrum for a small cluster of $N_s = 32$ sites. We find that the structure of the spectrum is significantly altered by the fact that fermionic excitations are gapped out already for $V = 0$ on finite lattices. Similarly, the σ_T level is gapped out at $V = 0$, and takes on a finite at $V = V_c$. It only decreases for $V > V_c$ to form the anticipated two-fold degenerate ground state manifold of the charge-density-wave phase.

In contrast, the ϵ_T is level behaves similar to the one of the H-type clusters and exhibits a minimum around the critical interaction.

4.3.2 Critical torus spectrum

We now proceed with a closer analysis of the critical torus spectrum, i.e. a snapshot of the torus spectrum at the critical interaction strength $V_c \approx 1.355t$ (honeycomb lattice). In the thermodynamic limit it is related to the torus spectrum of the chiral Ising fixed point. The critical torus spectrum in the thermodynamic limit is obtained by performing a standard finite-size extrapolation of the scaled gaps $\Delta_i \times L$, taking into account the results of both exact diagonalization and quantum Monte Carlo simulations. The outcome of the $N_s \to \infty$ extrapolation is illustrated in Fig. 4.4. Remarkably, the overall structure of the torus spectrum is already present in the small clusters which are accessible to exact diagonalization.

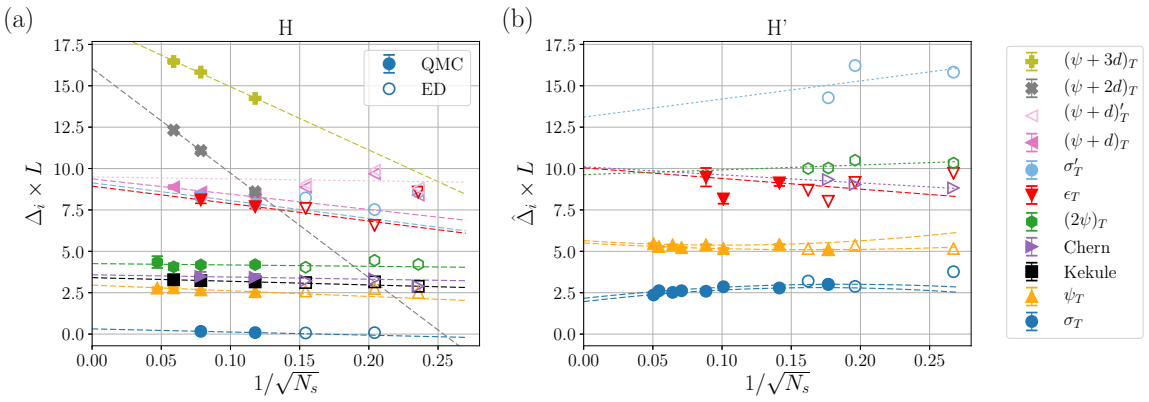

Figure 4.4: Extrapolation of the critical energy spectrum on the honeycomb lattice. We use second or first order polynomial functions (depending on the number of available data points) in $1/\sqrt{N_s}$ to extrapolate the gaps to $N_s \to \infty$. Open symbols denote ED data, while full symbols show QMC data, and we use the same labeling for the levels as in Fig. 4.3. Dashed (dotted) lines show extrapolations of QMC (ED) data. (a) shows clusters that contain the Dirac points, (b) shows clusters that do not. In (b) we extrapolate $L \mod 3 = 1$ and $L \mod 3 = 2$ clusters separately, where possible. With exception of the ϵ_T level, the extrapolations of ED/QMC data are in rather good agreement. Figure reprinted from [3].

The extrapolated critical torus spectrum is shown in Fig. 4.5. In anticipation of a comparison with an analytic ϵ-expansion, we have renormalized the scaled gaps $\Delta_i \times L$ by the critical Fermi velocity v_{F}^c. In general, the Fermi velocity is a model dependent parameter, which is renormalized by the interaction V. Using the universal relation Eq. (4.5) in the semi-metallic regime and at the critical point, we are able to obtain an estimate for v_{F}^c. The details of the Fermi velocity renormalization are topic of the following section 4.6, and at

this point we may treat it as a simple normalization constant. Furthermore, Fig. 4.5 includes results for the torus spectrum of the π-flux square, the details of which can be found in Ref. [3].

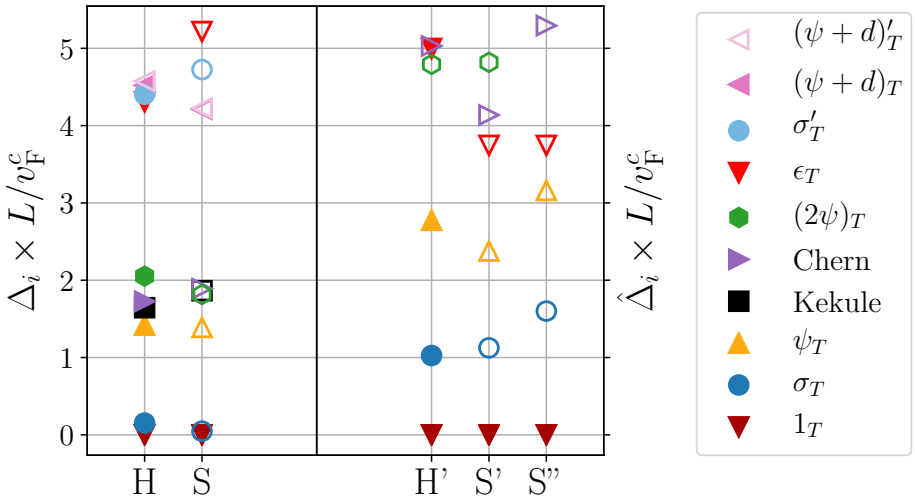

Figure 4.5: Critical torus spectrum of the $N = 4$ chiral Ising theory for the honeycomb and square models. Shown are the most prominent low-energy levels after finite-size extrapolation [cf. Fig. 4.4]. The left panel shows the extrapolated levels from tori that contain the Dirac points, while the right panel those that do not contain the Dirac points. The spectrum has been normalized by the critical Fermi velocities v_{F}^c for the different geometries [cf. Fig. 4.14]. Full symbols show levels extrapolated from QMC data, empty symbols denote levels extrapolated from ED data alone. Figure reprinted from [3].

From Fig. 4.5, we observe the following characteristic features of clusters that include the Dirac points (H-type clusters):

1. The σ_T level appears to have a very small gap, and may potentially form a 2-fold degenerate ground state manifold with the vacuum level 1_T in the thermodynamic limit.

2. The next lowest excited states in the same symmetry sectors, which correspond to the σ'_T and ϵ_T levels respectively, are also (quasi-)degenerate when one accounts for finite-size corrections. This doubling effect appears to be characteristic of the chiral Ising universality class, as it does not appear in the convectional Wilson-Fisher spectrum [49].

3. The lowest level above the (quasi-)degenerate vacuum levels is given by the 8-fold degenerate fermion mode ψ_T.

4. We find that the 2-fermion mode $(2\psi)_T$, the Kekulé and the Chern levels are each two-fold degenerate and appear close to each other in the spectrum. In the ϵ-expansion these levels are exactly degenerate in first order, and their small splitting on the lattice could potentially be attributed to remaining finite-size effects.

5. The two single-fermion levels $(\psi + d)_T^{(\prime)}$ with minimum momentum $\mathbf{k}_{\text{min}}$ are again found to be (quasi-)degenerate, alluding to the aforementioned level doubling. Their energy is similar to the (ϵ_T, σ_T') pair.

In contrast, for clusters of type H', i.e. without the Dirac points, we find different characteristics:

1. The σ_T level has a significant gap to the vacuum level 1_T. Consequently, we do not find the previous level doubling in the torus spectrum, and the higher levels ϵ_T and σ_T' are similarly separated.

2. The value of the ϵ_T seems to not be strongly affected by the torus geometry.

3. The lowest level above the (quasi-)degenerate vacuum levels is again given by the 8-fold degenerate fermion mode ψ_T.

4. The 2-fermion mode $(2\psi)_T$, the Kekulé and the Chern levels are again close to other in the spectrum.

4.4 Torus spectrum of the Gross-Neveu-Yukawa theory

After the discussion of the $t - V$ model torus spectrum on finite lattices, we will now focus on the continuum limit, and discuss the torus spectrum of the free Dirac and Gross-Neveu-Yukawa fixed points of the Gross-Neveu-Yukawa field theory. Finally, we compare the numerical results of the previous section with analytic results from an ϵ-expansion up to first order.

4.4.1 Free Dirac fixed point

In the semi-metallic phase, i.e. for $V < V_c$, the $t - V$ model realizes a lattice implementation of the massless Dirac conformal field theory (CFT), whose Lagrangian is given by

$$\mathcal{L}_{\text{D}} = -\overline{\Psi}^j \not{\partial} \Psi^j, \tag{4.15}$$

which corresponds to the effective theory of Eq. (4.8) for $s > s_c$. Because this theory is non-interacting, its excitation energies can be calculated exactly. Following the general form of Eq. (4.5), the torus spectrum in the semi-metallic phase is given by

$$\Delta_i = \frac{v_{\mathrm{F}}(V)}{L}\xi_i^{\mathrm{D}}, \tag{4.16}$$

where Δ_i, $i = 1, 2, ...$ denotes the set of excitation energies relative to the ground state energy, $v_{\mathrm{F}}(V)$ is the renormalized Fermi velocity at interaction strength V, and $\{\xi^{\mathrm{D}}\}$ is a set of universal numbers that characterize the free Dirac CFT [49, 59, 60]. Note that in the lattice implementation, the effective speed of light is realized by the Fermi velocity of the Dirac fermions. In general, this effective excitation speed is non-universal and will depend on the microscopic parameters of the model, in this case the ratio V/t. However, in the CFT description the speed of light itself becomes a microscopic parameter and is typically set to unity. This effectively rescales the excitation energies, but the universal numbers $\{\xi^{\mathrm{D}}\}$ remain invariant.

The values ξ_i^{D} for the lowest energy levels are shown in Fig. 4.6(a). Due to the particle-number conservation and translation invariance of the free Dirac Hamiltonian, we label the eigenstates by their particle-number n_f (relative to half-filling) and momentum $\boldsymbol{k}$. At half-filling, the low-energy many-body eigenstates may either have momentum $\boldsymbol{k} = \boldsymbol{K}$, $\boldsymbol{k} = \boldsymbol{K}'$ or $\boldsymbol{k} = \mathbf{0}$. To parametrize all states by a single variable, we introduce the reduced momentum variable

$$\kappa = \frac{3}{4\pi}L\left|\mathbf{k} \mod \mathbf{K}^{(\prime)}\right|, \tag{4.17}$$

which includes the modulo operation with respect to $\boldsymbol{K}$ and $\boldsymbol{K}'$. Small values of κ then map to the low-energy sector described by the free Dirac CFT. The normalization is chosen such that momenta closest to the Dirac points correspond to a value of $\kappa = 1$ (for lattice constant $a = 1$). The universal numbers $\{\xi^{\mathrm{D}}\}$, together with the quantum numbers and degeneracies of the corresponding levels, provide a characteristic fingerprint of the Dirac CFT.

4.4.2 Chiral Ising fixed point

At its critical point $V = V_c \approx 1.355t$ [52], the $t - V$ model is described by the strongly interacting chiral Ising conformal field theory. Similarly, the chiral Ising CFT corresponds to the interacting fixed point of the Gross-Neveu-Yukawa theory for $s = s_c$ in Eq. (4.8). This theory is then found to be characterized by a different torus spectrum,

$$\Delta_i = \frac{v_{\mathrm{F}}^c}{L}\xi_i^{\mathrm{CI}}, \tag{4.18}$$

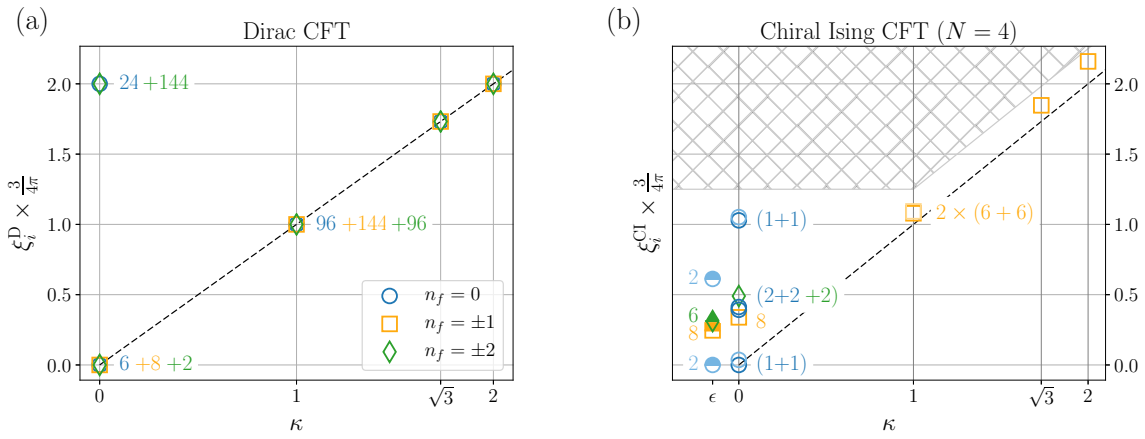

Figure 4.6: Critical torus low-energy spectrum for (a) the free, massless Dirac CFT, and (b) the four-component chiral Ising GNY theory, as a function of the reduced momentum κ on the honeycomb lattice with $\delta_k = 0$. Different symbols and colors indicate the fermion number sectors n_f. The numbers in the plots indicate the degeneracy of the levels, while the parenthesis in (b) indicate the nearly degenerate levels described previously. The spectrum in (a) is computed exactly analytically, the spectrum in (b) is the extrapolated data from the $\delta_k = 0$ honeycomb lattices. The black, dashed lines show a linear dispersion according to the Fermi velocity v_{F} [see also Fig. 4.14]. In (b), the $N_f = 0$ levels at $\kappa = 0$ from bottom to top correspond to the levels 1, σ_T, Kekulé, Chern, ϵ_T, σ_T', the $n_f = 1(2)$ levels denote the $(2\psi)_T$ levels. The $n_f = 1$ levels at $\kappa = 1$ correspond to the $(\psi_T + d)^{(\prime)}$ levels. Figure reprinted from [3].

where v_{F}^c is the renormalized Fermi velocity at the critical point, and the universal numbers $\{\xi^{\mathrm{CI}}\}$ are distinct from the ones of the Dirac theory. The determination of v_{F}^c is non-trivial, and requires a careful analysis which is covered in section 4.6. In the following, we will compare the torus spectrum of the lattice model with the results of an analytic ϵ-expansion up to first order, the details of which can be found in Ref. [3].

In we show Fig. 4.6(b) the universal numbers $\{\xi^{\mathrm{CI}}\}$ and their multiplicities for the low-energy levels of the chiral Ising torus spectrum, which have been obtained by the finite size extrapolations of the critical torus spectrum. The normalization and reduced momentum variable κ is defined analogously to the free Dirac spectrum. In addition, the leftmost column indicates the analytic results of the ϵ-expansion for the lowest levels in the $\kappa = 0$ sector.

Compared to the Dirac spectrum, we find that the chiral Ising spectrum is characterized by the splitting various low-energy states. Note that at criticality, the system remains gapless, however the scaled gaps $\Delta_i \times L$ in the torus spectrum may still take on a finite value in the thermodynamic limit. Overall, the 16-fold degeneracy of the Dirac spectrum is reduced to the 2-fold (quasi-)degeneracy in the chiral Ising spectrum. The remaining large degeneracies of the higher levels in the Dirac CFT are also expected to split up in the chiral Ising spectrum,

although we have not calculated and depicted all of them in Fig. 4.6(b). Furthermore, the energies of the lowest $\kappa = 1$ level is pushed slightly above the purely linear dispersion relation of the Dirac spectrum.

Interestingly, the ϵ-expansion predicts an exact 2-fold ground state degeneracy. The same holds true for the excited levels ϵ_T and σ'. The $n_f = \pm 1$ fermion modes exhibit an 8-fold degeneracy in the chiral Ising spectrum, which is confirmed by both numerical and analytic results. Conversely, in the ϵ-expansion we find a 6-fold degenerate level, which corresponds to a tensor representation of the chiral Ising CFT operator content. It is not too surprising that we do not find this exact degeneracy in the lattice spectrum, because the tensor representation requires the existence of an emergent $SU(2)$ symmetry [3]. We therefore expect the two-fermion mode $(2\psi)_T$, the Kekulé level and the Chern level, each of which is 2-fold degenerate, to form a 6-fold degenerate level in the continuum limit.

To summarize, we find that the level order, the multiplicities of the chiral Ising spectrum, as well as the action under the fundamental Z_2 symmetry (this is the symmetry that is spontaneously broken), is consistent in both numerical and analytic approaches. The exact mapping of the symmetry representations is more difficult, because the emergence of additional symmetries in the continuum limit. The universal numbers $\{\xi^{\mathrm{CI}}\}$ do show deviations, especially for the highest level. This may be caused either by remaining finite-size effects on the lattice side, or by the crude first order expansion on the analytic side.

4.4.3 Crossover effects

In the continuum limit, the effective theory for the $t - V$ lattice model will flow towards the free Dirac fixed point for all $V < V_c$. In this case the system is characterized by the dynamics of non-interacting massless Dirac fermions with a linear dispersion, and the torus spectrum is defined by the universal numbers ξ^{D}. Only at the critical interaction $V = V_c$ will the effective theory flow toward the interacting chiral Ising fixed point, in which case the dynamics become non-trivial and the torus spectrum is defined by the universal numbers ξ^{CI}. However, on finite clusters the energy spectrum is affected by crossover effects in the vicinity of the critical point. The renormalization group flow of the effective low-energy theory is first attracted by the chiral Ising fixed point on intermediate length scales, and then crosses over to the free Dirac fixed point beyond a crossover scale $L_c(V)$. Upon approaching the critical point, the crossover scale $L_c(V)$ diverges, and the true free Dirac spectrum can only be reached asymptotically for $L \gg L_c$.

This continuous crossover between the free Dirac spectrum and the chiral Ising spectrum particularly affects levels, for which the universal numbers ξ_i^{D} and ξ_i^{CI} differ strongly. Most notably, this is the case for levels which are gapless in the free Dirac theory, i.e. where

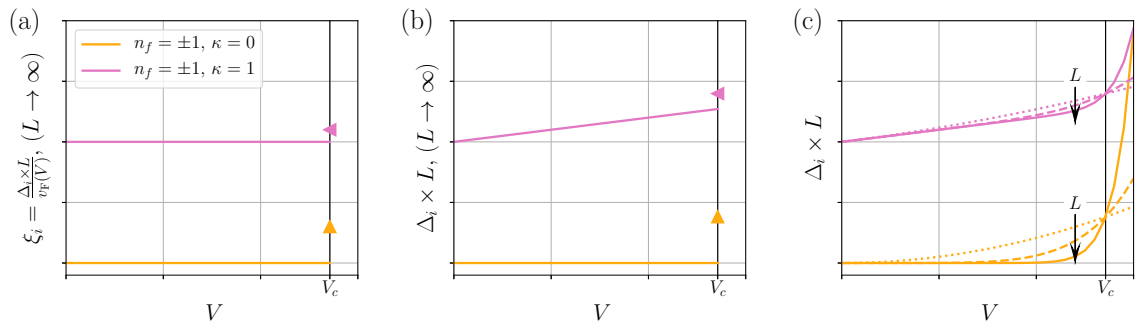

Figure 4.7: Sketch of crossover effects in the torus spectrum near the chiral Ising CFT. In (a) we show the universal numbers ξ_i for two different levels within the SM phase and at the QCP. (b) shows the scaled energy gaps $\Delta_i \times L \propto v_{\mathrm{F}}(V)\xi_i$ in the thermodynamic limit $L \to \infty$, assuming a linear Fermi velocity renormalization $v_{\mathrm{F}}(V)$, while (c) illustrates the scaled energy gaps measured from finite size systems with linear size L. Figure reprinted from [3].

$\xi^{\mathrm{D}} = 0$, but which acquire a finite gap in the chiral Ising theory, $\xi^{\mathrm{CI}} > 0$. The crossover effect is sketched in Fig. 4.7, which shows the torus spectrum in terms of the universal number ξ^{D} and ξ^{CI} in panel (a), the expected form of the scaled gaps $\Delta_i \times L$ in the thermodynamic limit in (b), and finally the scaled gaps as they are measured on finite lattices in (c). The latter case corresponds to the numerical data shown in Fig. 4.8, which displays the scaled one-fermion gap $\Delta(\psi_T) \times \sqrt{N_s}$ for different cluster sizes.

4.5 Numerical implementation of the spectroscopy analysis

In this section, I present the details of the spectroscopy analysis from the numerical side of things. First, I give an overview of the conceptual procedure in exact diagonalization, in which the torus spectrum is naturally obtained from the eigenstates of the Hamiltonian matrix. Then I will focus on the implementation of the quantum Monte Carlo simulation and the corresponding numerical energy gap extraction. The details of the exact diagonalization and the analytic ϵ-expansion can both be found in Ref. [3]. The section concludes with some remarks on finite size warping effects, and how we account for them when we calculate the energy gaps.

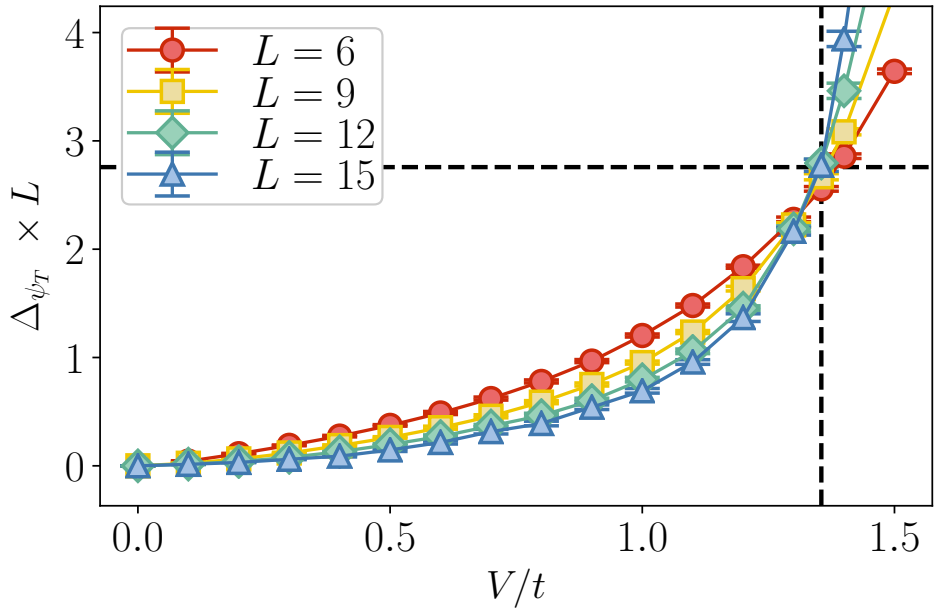

Figure 4.8: Scaled excitation gaps of the single fermion mode ψ_T for different system sizes. The location of the critical point is indicated by the dashed lines. in the semi-metallic regime, $V < V_c$, the scaled gaps trend toward zero because this level is gapless in the Dirac spectrum. Close to the critical interaction $V_c \approx 1.355t$, the scaled gap crosses over the finite value of the chiral Ising spectrum, which is indicated by the crossing point.

4.5.1 Exact Diagonalization

Exact diagonalization (ED) [66, 67] is a natural choice to perform the spectroscopy analysis because it has full access to the low-energy spectrum of the Hamiltonian. The Lanczos algorithm outputs all low-energy eigenstates, their degeneracies, and using a symmetry adapted basis, one may obtain all respective quantum numbers, which are imposed by translational symmetry, particle-hole symmetry and lattice symmetries. To be more concrete, we categorize the eigenstates according to their particle-number n_f (taken relative to half-filling), their particle-hole quantum number C, their crystal momentum $\boldsymbol{k}$ and their irreducible representation of the lattice point-group. Note that while of of these symmetries operations commute with the Hamiltonian, they do not necessarily commute with each other. For example, at half-filling, i.e. $n_f = 0$, states may have a well-defined particle-hole charge. However, in general eigenstates of the particle-hole operator will be a superposition of states from the $+n_f$ and $-n_f$ sectors. Similarly, finite momentum states transform according to a reduced symmetry group, rather than the full point group symmetry of the lattice. The classification of the low-energy states in terms of their symmetry is important because it not only provides qualitative features of the torus spectrum, but also because it allows us to construct operators, which connect the ground state to these excited states. That is, these

operators have a finite overlap with both the ground state and the targeted excited state, which means that one may extract the energy gaps from the decay of their imaginary-time correlation function. This is precisely the methodology we plan to use in the quantum Monte Carlo simulations, the details of which are described in the following sections.

4.5.2 Quantum Monte Carlo

To determine the torus spectrum on larger lattice clusters, we employ the projector lattice continuous-time quantum Monte Carlo algorithm (LCT-INT) detailed in [18]. In this formulation, the ground state expectation value of an observable $\hat{O}$ is accessed upon time-evolving a trial wave function $|\Psi_T\rangle$ in imaginary time,

$$\frac{\langle\Psi_0|\,\hat{O}\,|\Psi_0\rangle}{\langle\Psi_0|\Psi_0\rangle} = \lim_{\Theta\to\infty} \frac{\langle\Psi_T|\,\mathrm{e}^{-\frac{\Theta}{2}H}\hat{O}\,\mathrm{e}^{-\frac{\Theta}{2}H}\,|\Psi_T\rangle}{\langle\Psi_T|\,\mathrm{e}^{-\Theta H}\,|\Psi_T\rangle}\,, \tag{4.19}$$

where $|\Psi_0\rangle$ denotes the ground state of the Hamiltonian H. The systematic deviation from the true ground state expectation values typically decreases exponentially with the projection length Θ, and the decay rate will depend on the smallest energy scale in the system. For the $t-V$ model, we found that values of up to $\Theta = 160/t$ are required to ensure convergence within the statistical uncertainty. Note that for clusters that do not contain the Dirac point the convergence is much faster due to the gapped out torus spectrum (cf. the discussion above). Importantly, the LCT-INT formulation does not rely on a Trotter decomposition, but instead decomposes the projection operator using an interaction expansion directly in continuous time, thus eliminating the Trotter error completely.

The lowest energy gaps $\Delta_{\hat{O}}$ are extracted from the asymptotic decay of imaginary-time correlation functions, whose leading contribution is given by

$$\left\langle \hat{O}(\tau)\hat{O}^\dagger \right\rangle \sim \left|\left\langle \Psi_0|\hat{O}|\Psi_{\Delta_{\hat{O}}}\right\rangle\right|^2 \exp(-\Delta_{\hat{O}}\tau)\,, \tag{4.20}$$

where for sufficiently large τ, with $1 \ll \tau \ll \Theta/2$, the decay is dominated by the smallest finite-size gap $\Delta_{\hat{O}}$ accessible by the operator $\hat{O}$. As mentioned in the discussion of exact diagonalization, the relevant low-energy gaps correspond to excited states in different symmetry sectors, which are determined by their fermion-number, momentum, particle-hole symmetry, and an irreducible representation of the lattice point-group. For the operators $\hat{O}$ to connect the ground state $|\Psi_0\rangle$ to the desired excited state $|\Psi_{\Delta_{\hat{O}}}\rangle$, they must be constructed such that the overlap $|\langle\Psi_0|\hat{O}|\Psi_{\Delta_{\hat{O}}}\rangle|$ is finite. Using the insights about the structure of the torus spectrum from exact diagonalization, feasible operators $\hat{O}$ can be found and categorized by their action under the various symmetry operations. For instance, operators which anti-commute with

the reflection operator I_x (cf. section 1.2), provide finite overlap between states of opposing parity. Similarly, the creation operator $\hat{O} = c^\dagger_{\boldsymbol{K}}$ connects the ground-state of the half-filled sector, with $\boldsymbol{k} = \boldsymbol{\Gamma}$ and $n_f = 0$, to the lowest excited state with momentum $\boldsymbol{k} = \boldsymbol{K}$ in the $n_f = 1$ sector. A detailed list of the symmetry properties of the operators connecting the ground state to the various relevant excited states can be found in Table 4.2. The explicit expressions of possible operator implementations are further discussed in Section 4.5.4.

4.5.3 Choice of the trial-wave-function

The trial wave function required for the projection in Eq. (4.19) is chosen as a zero momentum, particle-hole (anti-)symmetric ground state of the free Hamiltonian, and is represented by a Slater determinant

$$|\Psi_T\rangle = \sum_{y=1}^{N_p} \left(\sum_x c_x^\dagger P_{x,y} \right) |0\rangle = \sum_{y=1}^{N_p} \left(\boldsymbol{c}^\dagger P \right)_y |0\rangle \,, \tag{4.21}$$

such that P is a $N_s \times N_p$ matrix (N_s number of sites, N_p number of particles). To circumvent the sign-problem in this model the trial wave function must be chosen such that it corresponds to an eigenstate of the many-particle particle-hole operator

$$\hat{S}_{\text{PH}} |\Psi_T\rangle = \pm |\Psi_T\rangle \,. \tag{4.22}$$

Reflection Symmetry

The invariance of the Hamiltonian under the reflection symmetry I_x can be used to separate the two quasi-degenerate ground states of the interacting system. We therefore consider trial wave functions $|\Psi_T\rangle_\pm$ with I_x-eigenvalue ± 1 in order to project onto the ground state of the corresponding symmetry sectors. This particularly useful for the $t - V$ model, because we can use this eigenvalue to discriminate the two quasi-degenerate ground states.

To construct the symmetrized trial-wave-functions

$$I_x |\Psi_T\rangle_\pm = \pm |\Psi_T\rangle_\pm, \tag{4.23}$$

we need to adjust the P matrices of the Slater determinants such that Eq. (4.23) is fulfilled. In the following we use the fact that for one-dimensional representations of the symmetry group, the many-particle property of Eq. (4.23) effectively reduces to a single-particle problem. To be more precise, we perform the following steps to obtain $|\Psi_T\rangle_\pm$:

1. Build the Hamiltonian matrix of the non-interaction system H_t in the single-particle basis in real space and perform a matrix diagonalization

$$H_t = U^\dagger D U \ . \tag{4.24}$$

Due to the particle-hole symmetry of H_t the energy spectrum is symmetric about the eigenvalue $E = 0$, which itself is 4-fold degenerate from the two Dirac points with two orbitals.

2. The single-particle states $\boldsymbol{u}_n,\ n = 1, ..., N_s$ are given by the column vectors of the U matrix in equation (4.24). The reflection operation on the single-particle level is defined by the permutation matrix

$$(P_{I_x})_{n,I_x(n)} = 1 \ , \tag{4.25}$$

where $I_x(n)$ is the site n after reflection. For each eigenspace of H_t we can now (anti-) symmetrize the eigenstates

$$\boldsymbol{u}_m^\pm = \boldsymbol{u}_m \pm P_{I_x}\boldsymbol{u}_m \ . \tag{4.26}$$

Afterwards we apply a QR factorization on the set of $\{\hat{\boldsymbol{u}}_m^\pm\}$ column vectors to obtain a set of orthonormal eigenstates of both H_t and I_x.

3. Finally, we choose $N_p = \frac{N_s}{2}$ of the lowest lying single particle states such that the Slater determinant is given by

$$P = (\hat{\boldsymbol{u}}_{n_1}^{p_1}, \ldots, \hat{\boldsymbol{u}}_{n_{N_p}}^{p_{N_p}}). \tag{4.27}$$

Then the eigenvalue of the many-particle trial wave function is given by the product of the single-particle eigenvalues

$$p_{\text{total}} = \prod_i^{N_p} p_i \ . \tag{4.28}$$

Particle-Hole Symmetry

As previously mentioned, the trial-wave-function being an eigenfunction of the particle-hole transformation

$$c_{\boldsymbol{i}}^{\dagger} \to \begin{cases} c_{\boldsymbol{i}} & , \ \boldsymbol{i} \in \text{sublattice A} \\ -c_{\boldsymbol{i}} & , \ \boldsymbol{i} \in \text{sublattice B} \end{cases} \tag{4.29}$$

is crucial to ensure a numerically stable and sign-problem-free QMC simulation. The construction of the required P matrix is similar to the previous case of reflection symmetry, however since the particle-hole transformation connects states of different particle numbers, it must be treated directly on a many-body level. As a consequence, the total eigenvalue of the trial-wave-function cannot simply be obtained by its single-particle constituents in a particular single-particle basis, as was the case in Eq. (4.28). Note, however, that in the case of closed shells, that is if N_p is chosen such that the lowest eigen spaces of H_t are filled completely, the trial wave function is already (anti-)symmetric under particle-hole transformation and we can simply chose P as the N_p lowest column vectors $\{\boldsymbol{u}_m\}$. If $N_p = \frac{N_s}{2}$. If the Dirac points are present, this is however not the case and we have to teat the half-filled $E = 0$ shell as follows:

1. We can start once again by diagonalizing the non-interaction Hamiltonian H_t according to equation (4.24) or we can use a single-particle basis that is already symmetrized with regards to inversion symmetry. Neglecting the eigenstates of closed shells, we can construct 6 two-particle states from the 4-fold degenerate $E = 0$ shell, which must be paired up such that they map to each other under particle-hole transformation.

2. We first construct the following permutation matrix in the single-particle basis

$$(P_{PH})_{n,n} = \begin{cases} 1 & , \ \boldsymbol{i} \in \text{sublattice A} \\ -1 & , \ \boldsymbol{i} \in \text{sublattice B} \end{cases} , \tag{4.30}$$

   and use it to (anti-)symmetrize the eigenstates

$$\boldsymbol{u}_m^{\pm} = \boldsymbol{u}_m \pm P_{PH}\boldsymbol{u}_m \ , \tag{4.31}$$

   after which we apply the Gram-Schmidt procedure to obtain 4 orthonormal single-particle states $\hat{\boldsymbol{u}}_{1/2}^{+}$ and $\hat{\boldsymbol{u}}_{1/2}^{-}$, which we use to construct 4 single-particle states that are

related by particle-hole transformation

$$c_1^\dagger|0\rangle \mathrel{\widehat{=}} \frac{\hat{\boldsymbol{u}}_1^+ + \hat{\boldsymbol{u}}_1^-}{\sqrt{2}} = \boldsymbol{c}_1 \tag{4.32}$$

$$c_2^\dagger|0\rangle \mathrel{\widehat{=}} \frac{\hat{\boldsymbol{u}}_2^+ + \hat{\boldsymbol{u}}_2^-}{\sqrt{2}} = \boldsymbol{c}_2 \tag{4.33}$$

$$c_3^\dagger|0\rangle \mathrel{\widehat{=}} \frac{\hat{\boldsymbol{u}}_1^+ - \hat{\boldsymbol{u}}_1^-}{\sqrt{2}} = \boldsymbol{c}_3 \tag{4.34}$$

$$c_4^\dagger|0\rangle \mathrel{\widehat{=}} \frac{\hat{\boldsymbol{u}}_2^+ - \hat{\boldsymbol{u}}_2^-}{\sqrt{2}} = \boldsymbol{c}_4\ , \tag{4.35}$$

such that $\hat{S}_{PH}\ c_1^\dagger\ (\hat{S}_{PH})^{-1} = c_3$ and $\hat{S}_{PH}\ c_2^\dagger\ (\hat{S}_{PH})^{-1} = c_4$.

3. If we define $\hat{S}_{PH}|0\rangle = c_1^\dagger c_2^\dagger c_3^\dagger c_4^\dagger|0\rangle$ we find the 6 particle-hole (anti-)symmetric two-particle states to be:

$$|1\rangle^+ = c_1^\dagger c_4^\dagger|0\rangle \tag{4.36}$$

$$|2\rangle^+ = c_2^\dagger c_3^\dagger|0\rangle \tag{4.37}$$

$$|3\rangle^+ = \frac{c_1^\dagger c_3^\dagger|0\rangle - c_2^\dagger c_4^\dagger|0\rangle}{\sqrt{2}} \tag{4.38}$$

$$|4\rangle^- = c_1^\dagger c_2^\dagger|0\rangle \tag{4.39}$$

$$|5\rangle^- = c_3^\dagger c_4^\dagger|0\rangle \tag{4.40}$$

$$|6\rangle^- = \frac{c_1^\dagger c_3^\dagger|0\rangle + c_2^\dagger c_4^\dagger|0\rangle}{\sqrt{2}}\ . \tag{4.41}$$

To express for example state $|1\rangle^+$ as a Slater determinant, the two relevant columns of the P matrix are given by $(..., \boldsymbol{c}_1, \boldsymbol{c}_4)$. This construction is not possible for states $|3\rangle^+$ and $|6\rangle^-$, which cannot be expressed as Slater determinants in this basis. Also note that the total parity of the many-body wave function still depends on the neglected closed shells.

4.5.4 Operators for the gap estimation

The LCT-INT algorithm [18] used in this work makes explicit use of a weak coupling expansion of the partition function in terms of the interacting part of the Hamiltonian. As a result imaginary time displaced expectations values of the form in Eq. (4.20) can be expressed as expectation values of the free Hamiltonian. One can therefore employ the Wick theorem

Operator	PH	n_f	$\boldsymbol{k}$	C_6	C_3	C_2	I_x	I_y
O_{1_T}, O_{ϵ_T}	1	0	0	1	1	1	1	1
$O_{\sigma_T}, O_{\sigma'_T}$	-1	0	0	1	-1	-1	-1	1
$O_{\text{Kekulé}}$	1	0	$\boldsymbol{K}$	1	–	–	1	–
O_{Chern}	-1	0	0	–	–	-1	-1	1
O_{ψ_T}	–	1	$\boldsymbol{K}$	–	–	–	–	–
$O_{(2\psi)_T}$	–	2	0	–	–	–	–	–

Table 4.2: Symmetry properties of the operators connecting the ground state to the relevant excited states. Note that the operators do not transform the same as the actual levels. Rather they must break the symmetry that separates the ground state from the excited state. The tables denotes the action under particle-hole transformation PH, the fermion sector n_f and the momentum $\boldsymbol{k}$, as well as the action under rotations about $60°$ (C_6) and $120°$ (C_3), lattice inversion (C_2), and vertical (I_x) and horizontal (I_y) mirror reflection. 1 (-1) indicates a vanishing commutator (anti-commutator), and – corresponds to an otherwise broken symmetry. In the case of degenerate excited states operators with different symmetries can be allowed, which connect to superimposed states of the degenerate subspace.

to calculate a Monte Carlo estimator of Eq. (4.20) using Green functions of the form

$$G_{ij}(\tau) = \left\langle c_i(\tau)\, c_j^\dagger(0) \right\rangle , \tag{4.42}$$

which are calculated during the LCT-INT sampling process.

The 1_T level

The (quasi-)degenerate ground state manifold consists of one Z_2 even and one Z_2 odd state (under either particle-hole transformation or vertical reflection I_x). Both states have momentum $\boldsymbol{k} = 0$, and under the $D6$ point group of the honeycomb lattice, they transform according to the $A2$ and $B1$, respectively. On finite lattices we find a small gap between them. The association of these two states to the levels then depends on the number of lattice sites: If the linear dimension L of the lattice is an even number, the true ground-state is Z_2 even, otherwise it is Z_2 odd.

The σ_T level

The staggered density operator

$$\hat{O}_{\sigma_T} = \sum_i (-1)^i \left(n_i - \frac{1}{2} \right) \tag{4.43}$$

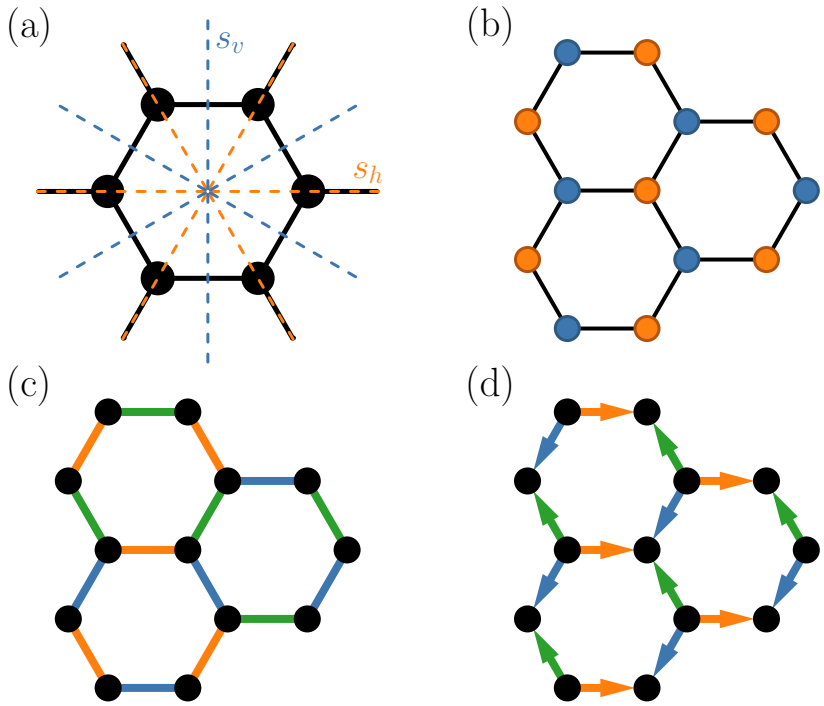

Figure 4.9: Real space illustration of the point group symmetry of the honeycomb lattice (A), as well as the operator representations used for the σ_T (B), Kekulé (C) and chern level (D). In panel (A) the fixed point of lattice rotations is denoted by the red point in the center of the hexagon, while the blue (orange) dotted lines denote the axes of vertical (horizontal) mirror reflection. Panel (B) shows the anti-symmetric sub-lattice modulation of Eq. (4.43) with the standard two-site unit cell of the honeycomb lattice. Panel (C) depicts the three distinct Kekulé patterns K_1, K_2 and K_3 of the honeycomb lattice, and panel (D) depicts the current pattern of the bonds N_1, N_2 and N_3 used in Eq. (4.52). Figure reprinted from [3].

corresponds to the order parameter of the commensurate charge-density-wave of the bipartite lattice. The operator is anti-symmetric under particle-hole transformation and connects the Z_2-even and -odd quasi-degenerate lowest energy states with each other. Furthermore, this operator provides an overlap of the ground state with the energetically higher σ_T' level.

The ψ_T and $(\Psi + d)_T$ levels

The $n_f = 0$ sector can be connected to the $n_f = 1$ ($n_f = -1$) sector by operators that create (annihilate) a fermion with a certain momentum. For lattice clusters that contain the Dirac point, the lowest excited state of the $n_f = 1$ sector is connected to the $n_f = 0$ ground state by the operator

$$\hat{O}_{\psi_T} = c^\dagger_{\mathbf{K}} = \sum_i \mathrm{e}^{\mathrm{i}\mathbf{K}\cdot\boldsymbol{r}_i} c^\dagger_i, \tag{4.44}$$

which creates a fermion at the Dirac point $\mathbf{K}$. Note that the eight-fold degeneracy of the σ_T level follows from the valley, orbital and particle-hole degeneracy, $2_{\text{valley}} \times 2_{\text{orbital}} \times 2_{\text{PH}} = 8$.

Overlap to higher excited states can then be achieved by creating a fermion with the n-th closest momentum to the Dirac point,

$$\hat{O}_{(\psi+nd)_T} = c^\dagger_{\mathbf{K}+\boldsymbol{q}} = \sum_i \mathrm{e}^{\mathrm{i}(\mathbf{K}+\boldsymbol{q})\cdot\boldsymbol{r_i}} c_i^\dagger \,, \tag{4.45}$$

where the momentum $\boldsymbol{q}$ is chosen accordingly on the lattice cluster.

The $(2\psi)_T$ level

The $(2\psi)_T$ level corresponds to the lowest excited state in the $n_f = \pm 2$ sectors. The ground state can be connected to them by operators that create two fermions, one with momentum $\mathbf{K}$ and one with $-\mathbf{K}$,

$$\hat{O}_{2\psi_T} = c^\dagger_{\mathbf{K}} c^\dagger_{-\boldsymbol{K}} = \sum_{ij} \mathrm{e}^{\mathrm{i}\mathbf{K}\cdot(\boldsymbol{r_i}-\boldsymbol{r_j})} c_i^\dagger c_j^\dagger \,. \tag{4.46}$$

Note that the total momentum is zero. In this case, the valley and orbital degeneracies become redundant, and the two-fold degeneracy of the $(2\psi)_T$ level follows directly from particle-hole symmetry.

The ϵ_T level

The ϵ_T level corresponds to the first excited state with identical symmetries as the ground state. In order to connect states within the same symmetry sector, possible operators must commute with all symmetry operations. A suitable choice is therefore given by either part of the Hamiltonian,

$$\hat{O}^{(t)}_{\epsilon_T} = -t \sum_{\langle i,j \rangle} \left(c_i^\dagger c_j + c_j^\dagger c_i \right) , \tag{4.47}$$

$$\hat{O}^{(V)}_{\epsilon_T} = V \sum_{\langle i,j \rangle} \left(\hat{n}_i - \frac{1}{2} \right) \left(\hat{n}_j - \frac{1}{2} \right) . \tag{4.48}$$

Since both operators have a finite ground state expectation value, one has to extract the gap Δ_{ϵ_T} using the formula

$$\left\langle \hat{O}_{\epsilon_T}(\tau) \hat{O}^\dagger_{\epsilon_T} \right\rangle \sim \left| \langle \Psi_0 | \, \hat{O}_{\epsilon_T} \, | \Psi_{\epsilon_T} \rangle \right|^2 \mathrm{e}^{-\Delta_{\epsilon_T}\tau} + \left| \langle \Psi_0 | \, \hat{O}_{\epsilon_T} \, | \Psi_0 \rangle \right|^2 . \tag{4.49}$$

Note that the operator $\hat{O}^{(V)}_{\epsilon_T}$ is related to the weak coupling expansion used in LCT-INT. One can therefore calculate its correlation function, as well as the fidelity susceptibility, from the distribution of interaction vertices during the Monte Carlo sampling [31].

The σ'_T level

The σ'_T level corresponds to the second level in the same symmetry sector as σ_T. In analogy to the doubling of the ground state, i.e. the 1 and σ_T levels, the next highest levels of the respective symmetry sectors also form a pair consistent of the ϵ_T and σ'_T level. The σ'_T is therefore connected to the σ_T in the same way in which the 1 level couples to the ϵ_T level. For this reason, we can use the same operators $\hat{O}^{(t)}_{\epsilon_T}$ and $\hat{O}^{(V)}_{\epsilon_T}$ to connect to the σ'_T level, as long as we chose a trial-wave-function that projects onto the σ_T level as the ground state.

The Kekulé level

The Kekulé level corresponds to the lowest excited states in the $n_f = 0$ sector with momentum $\mathbf{K}$ and identical particle-hole parity as the ground state. This level is two-fold degenerate due to the valley degeneracy. Possible operators can be constructed from the Kekulé bond pattern, which itself is 3-fold degenerate on the honeycomb lattice (K_1, K_2 and K_3). The Kekulé pattern features an enlarged unit cell, which in reciprocal space corresponds to the momentum at the Dirac point. Because of the reduced lattice symmetry at finite momenta, states with momentum $\mathbf{K}$ do not have a well defined inversion parity. Nevertheless, one can choose to construct the Kekulé operators such that they are (anti-)symmetric under lattice inversion. In this case the operators do not have well defined momenta, and provide overlap of the ground state with states of momentum $\mathbf{K}$ as well as $-\mathbf{K}$,

$$\begin{aligned}\hat{O}^{(+)}_{\text{Kekulé}} = &\sum_{\langle i,j\rangle\in K_1}\left(c_i^\dagger c_j + c_j^\dagger c_i\right) + \sum_{\langle i,j\rangle\in K_2}\left(c_i^\dagger c_j + c_j^\dagger c_i\right)\\ &-2\sum_{\langle i,j\rangle\in K_3}\left(c_i^\dagger c_j + c_j^\dagger c_i\right), \qquad (4.50)\\ \hat{O}^{(-)}_{\text{Kekulé}} = &\sum_{\langle i,j\rangle\in K_1}\left(c_i^\dagger c_j + c_j^\dagger c_i\right) + \sum_{\langle i,j\rangle\in K_2}\left(c_i^\dagger c_j + c_j^\dagger c_i\right). \qquad (4.51)\end{aligned}$$

Note that both $\hat{O}^{(+)}_{\text{Kekulé}}$ and $\hat{O}^{(-)}_{\text{Kekulé}}$ transform symmetric under the Z_2 particle-hole transformation.

The Chern level

The Chern level denotes the lowest excited states in the $n_f = 0$ sector with zero momentum and opposite particle-hole parity as the ground state. These states are two-fold degenerate and transform according to a two-dimensional irreducible representation of the point group. They can be connected to the ground state by current operators that are anti-symmetric under particle-hole transformation and break rotational symmetry, such as

$$\hat{O}_{\text{Chern}} = \mathrm{i} \sum_{\langle i,j\rangle \in N_1} \left(c_i^\dagger c_j - c_j^\dagger c_i\right) + \frac{1}{2}\mathrm{i} \sum_{\langle i,j\rangle \in N_2} \left(c_i^\dagger c_j - c_j^\dagger c_i\right) + \frac{1}{2}\mathrm{i} \sum_{\langle i,j\rangle \in N_3} \left(c_i^\dagger c_j - c_j^\dagger c_i\right). \tag{4.52}$$

4.5.5 Extracting energy gaps from imaginary time decay

In general, the leading contribution to the imaginary time decay of the gap operator correlation function is given by

$$\left\langle \hat{O}(\tau)\hat{O}^\dagger \right\rangle \sim \left| \left\langle \Psi_0 | \hat{O} | \Psi_{\Delta_{\hat{O}}} \right\rangle \right|^2 \exp(-\Delta_{\hat{O}}\tau) + \left| \langle \Psi_0 | \hat{O} | \Psi_0 \rangle \right|^2, \tag{4.53}$$

where $\hat{O}$ is one of the aforementioned operators that connect the the ground state $|\Psi_0\rangle$ to the lowest excited state $|\Psi_{\Delta_{\hat{O}}}\rangle$.

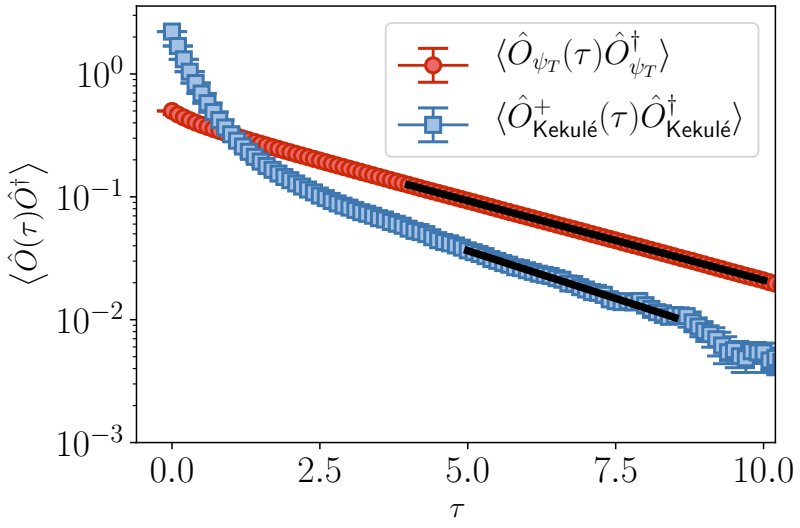

Figure 4.10: Imaginary time displaced correlation functions of $\hat{O}_{\psi_T}$ and $\hat{O}_{\text{Kekulé}}$ at the critical point $V = 1.355t$. The black lines denote fits to functions of the form $f(\tau) = a\exp(-\Delta\tau)$, which yield $\Delta_{\psi_T} = 0.297(3)$ and $\Delta_{\text{Kekulé}} = 0.359(16)$, respectively.

Higher energy states with energy gaps of $\Delta^n_{\hat{O}} > \Delta_{\hat{O}} > 0$ give corrections of the form $\left|\left\langle \Psi_0|\hat{O}|\Psi_{\Delta^n_{\hat{O}}}\right\rangle\right|^2 \exp(-\Delta^n_{\hat{O}}\tau)$, and are therefore exponentially supressed for $\tau \gg 0$. Nevertheless, the minimum τ required for a stable fit to Eq. (4.53) strongly varies depending on the operator $\hat{O}$. On the one hand, one therefore wishes to choose the starting point of the fitting range as large as possible. On the other hand, the quality of the data points declines for very large values of τ. Because of the measurement procedure in the quantum Monte Carlo algorithm (see section 2.4.3), data points at a certain τ_2 are correlated with data points at τ_1 if $\tau_1 < \tau_2$. In other words, the larger τ is, the more statistical samples are required to obtain decorrelated measurements. Since the number of measurements is fixed, the data quality declines with τ. One therefore has to balance both effects to find the optimal fitting range. To estimate the error on the fitting parameters, varying fitting ranges can be chosen.

Figure 4.10 shows an exemplary analysis of the ψ_T and Kekulé energy gaps for $L = 9$ at the critical point, $V = 1.355t$. Clearly, the fitting range for the Kekulé correlation function is more restricted compared to the one for ψ_T, which in constrast exhibits only minimal higher order corrections. Note that the $L = 9$ lattice contains an uneven number of unit cells in each lattice direction, which means that the ground state 1_T is antisymmetric with regards to the x-reflection operation, $I_x = -1$ (Z_2 odd). Conversely, the quasi-degenerate state σ_T corresponds to $I_x = 1$ (Z_2 even). Since Δ_{ψ_T} and $\Delta_{\text{Kekulé}}$ are measured with regards to the ground state, the trial-wave-function is chosen accordingly with $I_x = -1$.

In contrast, figure 4.11 illustrates the measurement of the σ'_T level. Here, we measure the gap of the $\hat{O}_{\epsilon_T}$ operator with regards to the σ_T level rather than 1_T, which is achieved by using a Z_2 even trial-wave-function with $I_x = 1$. To improve the measurement statistics, we use an operator $\hat{O}_{\epsilon_T} \sim \hat{O}^{(V)}_{\epsilon_T}$, and use the measurement technique outline in [68]. As an additional complication, the state σ_T itself has a finite overlap with $\hat{O}_{\epsilon_T}$, such that the imaginary time correlations decay to a finite value. To finally obtain the correct gap estimation, the difference between the 1_T and σ_T levels, which is defined as Δ_{σ_T}, must be added to the extracted gap.

4.5.6 Warping corrections

The linear dispersion around the Dirac points that emerges in the low-energy description of graphene-like models is found to be asymmetrical at small, but finite distances to $\boldsymbol{K}$ and $\boldsymbol{K}'$. These distortions are known as warping effects of the dispersion relation. As a result, large lattice sizes are required to obtain the fine momentum resolution that is required to probe the uniformly linear linear dispersion, which is reached in the asymptotic limit. Furthermore, the free dispersion, i.e. at $V = 0$, is already effected by warping corrections. We therefore propose an unwarping correction to the finite-size energy gaps by dividing out the warped

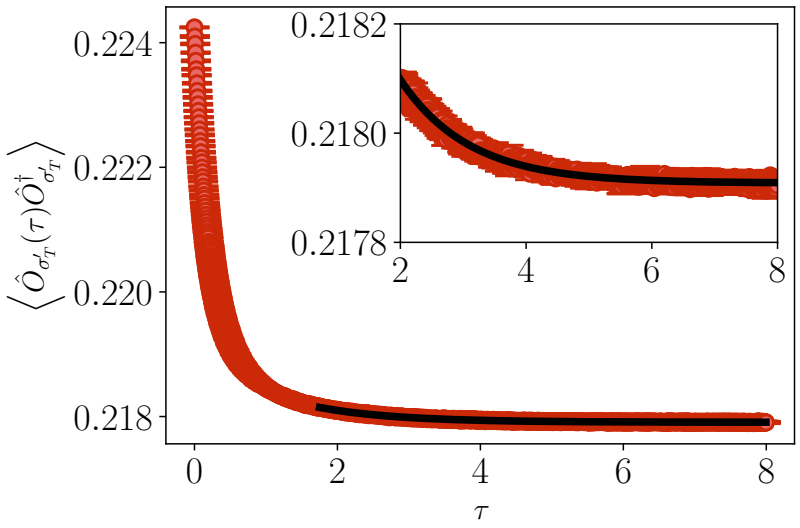

Figure 4.11: Imaginary time displaced correlation function of $\hat{O}_{\sigma'_T} = \hat{O}_{\epsilon_T}$ with respect to the σ_T level. The black line denotes a fit to the function $f(\tau) = a \exp(-\Delta\tau) + b$, which yields a gap of $\Delta = 0.903(20)$. The estimate for the σ'_T energy gap therefore corresponds to $\Delta_{\sigma'_T} = \Delta + \Delta_{\sigma_T} = 0.921(22)$. The inset shows a closeup of the fitting region.

free dispersion according to

$$\Delta_i \to \hat{\Delta}_i = \frac{v_{\mathrm{F}}^0 \left|\mathbf{K} - \mathbf{k}_{\mathrm{min}}\right|}{\varepsilon^0\left(\mathbf{k}_{\mathrm{min}}\right)} \Delta_i \,, \tag{4.54}$$

where $v_{\mathrm{F}}^0 = \frac{3t}{2a}$ denotes the Fermi velocity for $V = 0$, $\varepsilon^0(\mathbf{k})$ the dispersion relation of the non-interacting system, and $\mathbf{K}$ is the Dirac point. The goal of this correction to reduce the finite-size effects on the torus spectrum of clusters without Dirac points, where the energies at the smallest momenta are influenced strongly by the warping effect. Note that in the thermodynamic limit the unwarping factor tends to one,

$$\lim_{L\to\infty} \left(\frac{v_{\mathrm{F}}^0 \left|\mathbf{K} - \mathbf{k}_{\mathrm{min}}\right|}{\varepsilon^0\left(\mathbf{k}_{\mathrm{min}}\right)} \right) = \lim_{\boldsymbol{k}_{\mathrm{min}}\to 0} \left(\frac{v_{\mathrm{F}}^0 \left|\mathbf{K} - \mathbf{k}_{\mathrm{min}}\right|}{\varepsilon^0\left(\mathbf{k}_{\mathrm{min}}\right)} \right) = 1. \tag{4.55}$$

Figure Fig. 4.12 illustrates the unwarping of the energy dispersion, and in the following sections, we denote with $\hat{\Delta}_i$ energy gaps that have been unwarped according to Eq. (4.54).

4.6 Renormalization of the Fermi velocity

We have seen that the Fermi velocity appears as a parameter in the torus spectrum because it determines the speed of the massless fermionic excitations. However, contrary to the universal

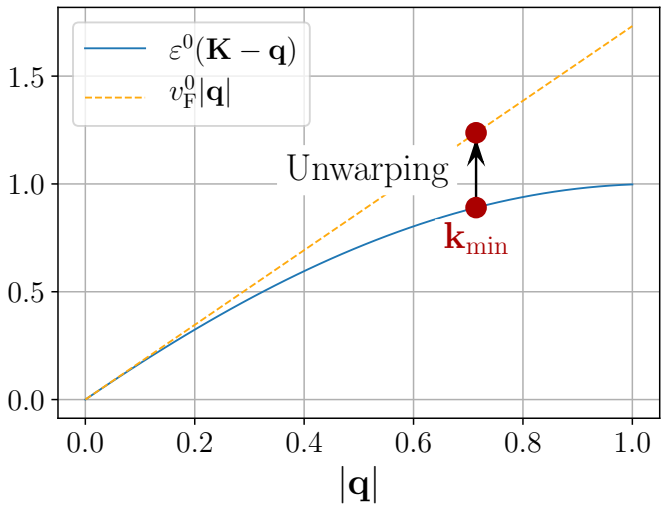

Figure 4.12: Unwarping of the energy spectrum for clusters that do not contain the Dirac points in order to reduce finite-size effects. The finite-size spectrum for all interaction strengths V is multiplied by a (N_s-dependent) constant such that the non-interacting fermion dispersion aligns with the (effective) linear Dirac cone with velocity v_F^0 at $\mathbf{k} = \mathbf{k}_\mathrm{min}$. Figure reprinted from [3].

numbers $\{\xi\}$ and the level degeneracies, the Fermi velocity is non-universal and will depend on the microscopic details of the lattice implementation. Hence, it gets renormalized already in the semi-metallic phase of Dirac systems, and we denote this renormalized Fermi velocity with $v_\mathrm{F}(V)$. Of course, ultimately we are interested in the universal features of the torus spectrum – we therefore require an estimate of the Fermi velocity to obtain the set of universal numbers $\{\xi\}$ from the physically accessible energy gaps $\{\Delta\}$. To do so, our strategy is the following: First, we make use of the fact that the torus spectrum of the free Dirac theory is known exactly. This allows us to compute the Fermi velocity renormalization in the semi-metallic regime, and assuming a non-singular functional dependence, we then extrapolate $v_\mathrm{F}(V)$ up to the critical interaction strength to obtain $v_\mathrm{F}^c = \lim_{V\to V_c}[v_\mathrm{F}(V)]$.

To conclude our analysis of the chiral Ising torus spectrum, the proper estimation of the Fermi velocity renormalization is first demonstrated for the $t-V$ model. Afterwards, we follow up on a recent work [69], which investigates the Fermi velocity renormalization in the Hubbard model on the honeycomb lattice. We apply the insights of the torus spectroscopy to point out flaws in the finite-size extrapolation of this work, which has led the authors to significantly underestimate the Fermi velocity in the vicinity of the quantum critical point of this model.

4.6.1 The Fermi velocity in the $t - V$ model

As we have discussed in section 4.4.3, the RG flow of the effective low-energy theory of the lattice model is attracted towards the free Dirac fixed point for all values of $V < V_c$, and only directly at the critical interaction will the system flow towards the interacting chiral Ising fixed point. Hence, the renormalized Fermi velocity in the semi-metallic regime is determined completely by

$$v_{\mathrm{F}}(V) = \lim_{L\to\infty} \frac{\Delta_i L}{\xi_i^{\mathrm{D}}}, \quad (V < V_c), \tag{4.56}$$

where the values for ξ_i^{D} do not depend on V and may be computed exactly, and the energy gaps Δ_i are accessible by numerics. Note that Eq. (4.56) holds true for all levels, as long as they have a finite gap in the torus spectrum, i.e. $\xi_i^{\mathrm{D}} > 0$. We can therefore optimize our Fermi velocity estimation by choosing a level with minimum finite-size corrections.

To determine $v_{\mathrm{F}}(V)$ for the $t - V$ model we have found that the lowest single-fermion mode at the smallest finite momentum $\boldsymbol{k}_{\mathrm{min}}$ away from the Dirac point, exhibits small finite-size effects and is therefore a suitable candidate to calculate the Fermi velocity. For H-type clusters the lowest mode away from the Dirac point is given by $(\psi + d)_T$, because the ψ_T level does not have a finite gap in the torus spectrum ($\xi_{\psi_T}^{\mathrm{D}} = 0$), while for H'-type clusters the ψ_T level itself is already gapped ($\xi_{\psi_T}^{\mathrm{D}} > 0$). The momentum $\boldsymbol{k}_{\mathrm{min}}$ corresponds to a reduced momentum $\kappa = 1$ ($\kappa = \frac{1}{\sqrt{3}}$) for H-type clusters (H'-type clusters) [cf. Fig. 4.6(a)], and the value for $\xi_{(\psi+d)_T}^{\mathrm{D}}$ ($\xi_{\psi_T}^{\mathrm{D}}$) is exactly known for the free Dirac theory. In contrast, the same levels $\xi_{(\psi+d)_T}^{\mathrm{CI}}$ and $\xi_{\psi_T}^{\mathrm{CI}}$ for the chiral Ising field theory are not known a priori, and cannot be extracted from the scaled gap $\Delta \times L$ without the knowledge of v_{F}^c itself.

The results for the renormalized Fermi velocity, based on Eq. (4.56) and the aforementioned single-fermion mode in the semi-metallic regime, are shown in Fig. 4.13. We find that the functional dependence of $v_{\mathrm{F}}(V)$ is captured very well by a simple linear approximation, and the slope is almost identical for both cluster types. To extract the critical Fermi velocity, we perform a linear regression on the data points up to $V = 0.8t$ (cf. grey area in Fig. 4.13), which we then extend up to the critical interaction strength V_c. This results in a critical Fermi velocity of about $v_{\mathrm{F}}^c \approx 1.35 v_0$. Note that the universal numbers of $\{\xi^{\mathrm{CI}}\}$ for the chiral Ising torus spectrum in Fig. 4.6(b) haven been calculated with this value.

To conclude our analysis of the Fermi velocity renormalization in the $t - V$ model, we show in Fig. 4.14 the Fermi velocity based on Eq. (4.56) using various energy levels and system sizes. In (a) we show the renormalization based on the levels σ_T, ψ_T and $(2\psi)_T$ for cluster of type H' (not containing the Dirac points). As mentioned previously noted, the $n_f = \pm 1$ fermion mode (ψ_T) in the second panel exhibits the smallest finite-size effects, and

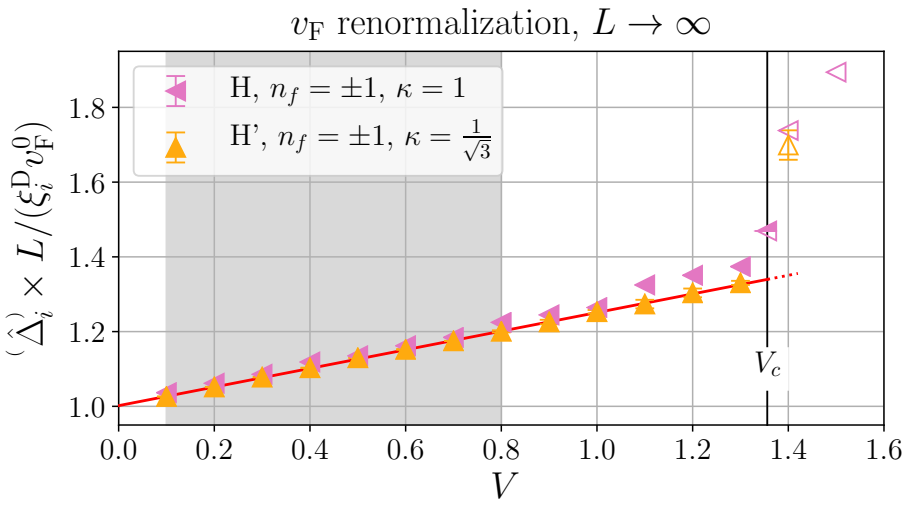

Figure 4.13: Renormalized Fermi velocity $v_\mathrm{F}(V)$ of the honeycomb lattice model H_h, based on the energy gap to the single-particle excitation $n_f = \pm 1$ at the momentum closest to the Dirac points $\kappa = 1$, as obtained after an extrapolation to the TDL. The red line indicates a linear regression of the data points within the shaded region and is an estimator for $v_\mathrm{F}(V)/v_\mathrm{F}^0$ within the SM phase. Based on the data we assume a continous behaviour of $v_\mathrm{F}(V)$ up to the critical point V_c to estimate a critical velocity v_F^c which is approximately 35% larger than v_F^0. Figure reprinted from [3].

is therefore the used for the best linear regression. The remaining $n_f = 0$ and $n_F = \pm 2$ are subject to larger finite-size corrections, but they are still consistent with the approximated linear renormalization. Most notable, for the σ_T level the Fermi velocity appears to rapidly decrease close to the critical point – this is a finite-size effect that is caused by the crossover between the Dirac and chiral Ising torus spectrum, as discussed in section 4.4.3. We would expect that the Fermi velocity only follows the linear approximation (red dotted line in the first panel of Fig. 4.14(a)) for system sizes larger than the crossover length scale, $L \gg L_\mathrm{cross}$. Because L_cross diverges upon approaching the critical point, the torus spectrum of finite clusters is significantly impacted by the chiral Ising spectrum already for $V < V_c$. For the ψ_T level this effect is minimized because the universal constants of the torus spectrum are similar for both theories, i.e. $\xi_{\psi_T}^\mathrm{D} \approx \xi_{\psi_T}^\mathrm{CI}$.

For the H-type clusters (cf. Fig. 4.14(b)), we only include the $(\psi + d)_T$ level, because many other levels, such as the levels depicted in Fig. 4.14(a), vanish faster than $1/L$ in the semi-metallic phase (cf. Fig. 4.8). This results in vanishing universal numbers $\xi_{\psi_T}^\mathrm{D} = 0$, which reduces the number of suitable levels to calculate $v_\mathrm{F}(V)$.

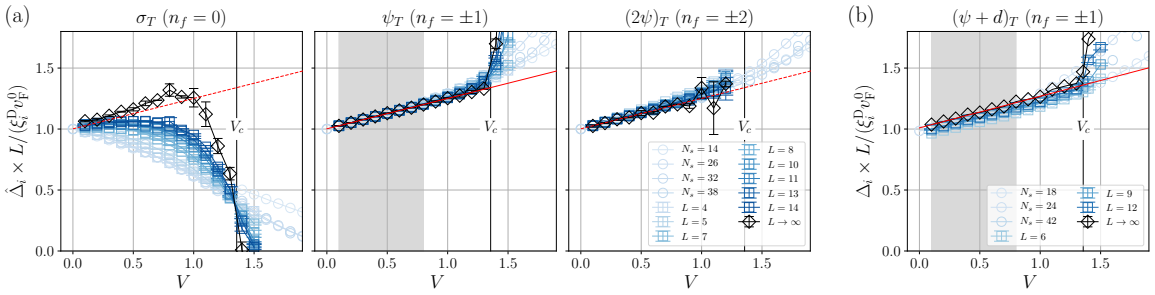

Figure 4.14: Renormalization of the Fermi velocity in the SM phase for the honeycomb lattice model. In (a) the energy gaps $\Delta' \times \sqrt{N_s}$ of low-lying levels for clusters without Dirac points as a function of the interaction strength V are shown. The gaps are normalized to one at $V = 0$ for easier comparison. Blue square (circle) symbols show finite-size data from QMC (ED), while the black diamonds are the finite-size extrapolated values for each V. The extrapolated data for the fermion excitation $n_f = 1$ (center panel) is fitted by a linear function (full red line), showing the Fermi velocity renormalization. This fit is included in the other panels by a dashed line as a comparison. (b) shows the gap of the single fermion excitation at $\mathbf{k}_{\text{min}}$ for clusters that contain the Dirac points, together with a fit describing the v_{F} renormalization. Note, that the gaps for levels shown in (a) would vanish in the SM phase for these clusters. Figure reprinted from [3].

4.6.2 The Fermi velocity in the Hubbard model

Recently, the Fermi velocity renormalization in the Hubbard model on a honeycomb lattice at half-filling has been investigated [69]. In contrast to the $t - V$ model, it contains additional spin degrees of freedom, and the nearest-neighbor V repulsion is replaced by an on-site U repulsion. The quantum critical point in this model has been studied extensively, and it belongs to the chiral Heisenberg universality class. It is characterized by an $O(3)$ spontaneous symmetry breaking (as opposed to a Z_2 symmetry breaking for the chiral Ising class), and the quantum critical point separates a semi-metallic phase and an anti-ferromagnetic phase. For a detailed discussion of the Hubbard model on the honeycomb lattice I refer to Ref. [48].

In Ref. [69], the authors claim to observe a significant decrease of the Fermi velocity of up to 40% in the vicinity of the critical point. Here, we use the insights on our previous discussion about the torus spectroscopy to refute this claim, and show that the original data provided by the authors of Ref. [69] is not consistent with a substantial decreases of the Fermi velocity. Instead, we argue that the alleged drop of the Fermi velocity is caused by an improper finite-size extrapolation, which does not take the crossover of the energy levels from the Dirac to chiral Heisenberg torus spectrum into consideration.

A naive approach to calculate the Fermi velocity would consider simply the slope between the single particle energy at the Dirac point $\boldsymbol{K}$ and its neighboring momentum $\boldsymbol{k}_{\text{min}}$, such that

$$v_{\text{F}}^{\text{slope}} = \lim_{L\to\infty} \frac{\Delta(\boldsymbol{k}_{\text{min}}) - \Delta(\mathbf{K})}{|\boldsymbol{k}_{\text{min}} - \mathbf{K}|}. \tag{4.57}$$

Here, the denominator contains the smallest momentum difference on a finite lattice, which is given by the reciprocal lattice unit vector $\boldsymbol{b}$ divided by the linear lattice dimension L,

$$\boldsymbol{k}_{\text{min}} - \mathbf{K} = \boldsymbol{b}\frac{1}{L}. \tag{4.58}$$

These two levels correspond to the lowest energy excitations in the $n_f = \pm 1$ sector, and for clusters containing the Dirac points, we denoted them with $\Delta(\boldsymbol{k}_{\text{min}}) \cong (\psi + d)_T$ with $\kappa = 1$ and $\Delta(\boldsymbol{K}) \cong \psi_T$ with $\kappa = 0$, respectively [cf. section 4.3].

We insert Eq. (4.16) and Eq. (4.58) into Eq. (4.57) and find (assuming a honeycomb lattice with lattice constant $a = 1$)

$$\begin{aligned} v_{\text{F}}^{\text{slope}} &= \frac{v_{\text{F}}\xi^{\text{D}}_{(\psi+d)_T}}{L}\frac{L}{|\boldsymbol{b}|} - \frac{v_{\text{F}}\xi^{\text{D}}_{\psi_T}}{L}\frac{L}{|\boldsymbol{b}|} \\ &= v_{\text{F}}\left(\frac{3}{4\pi}\xi^{\text{D}}_{(\psi+d)_T} - \frac{3}{4\pi}\xi^{\text{D}}_{\psi_T}\right). \end{aligned} \tag{4.59}$$

Finally, after inserting the values for the universal numbers ξ^{D} for the free Dirac theory [1], we conclude that indeed $v_{\text{F}}^{\text{slope}} = v_{\text{F}}$ in the semi-metallic regime.

Upon further inspection of Eq. (4.59), we find that only the first term contributes to $v_{\text{F}}^{\text{slope}}$, and the second term vanishes in the thermodynamic limit due to the fact that the ψ_T level is gapped in the torus spectrum (cf. Fig. 4.8). Nonetheless, the ψ_T level may contribute significant finite-size effects to $v_{\text{F}}^{\text{slope}}$ due to the crossover between $\xi^{\text{D}}_{\psi_T} = 0$ and $\xi^{\text{CH}}_{\psi_T} > 0$, as discussed in section 4.4.3. Note that directly at the critical point, the slope estimator for the Fermi velocity yields

$$\begin{aligned} v_{\text{F}}^{\text{slope}} &= \frac{v_{\text{F}}\xi^{\text{CH}}_{(\psi+d)_T}}{L}\frac{L}{|\boldsymbol{b}|} - \frac{v_{\text{F}}\xi^{\text{CH}}_{\psi_T}}{L}\frac{L}{|\boldsymbol{b}|} \\ &= v_{\text{F}}\left(\frac{3}{4\pi}\xi^{\text{CH}}_{(\psi+d)_T} - \frac{3}{4\pi}\xi^{\text{CH}}_{\psi_T}\right), \end{aligned} \tag{4.60}$$

[1] Cf. Fig. 4.6, the additional spin degree of freedom only adds additional multiplicities to the torus spectrum of the free Dirac theory.

where the universal numbers $\xi^{\mathrm{CH}}_{(\psi+d)_T}$ and $\xi^{\mathrm{CH}}_{\psi_T}$ of the chiral Heisenberg class are non-trivial, and therefore the naive estimator $v_{\mathrm{F}}^{\mathrm{slope}}$ does not reproduce v_{F} even in the thermodynamic limit.

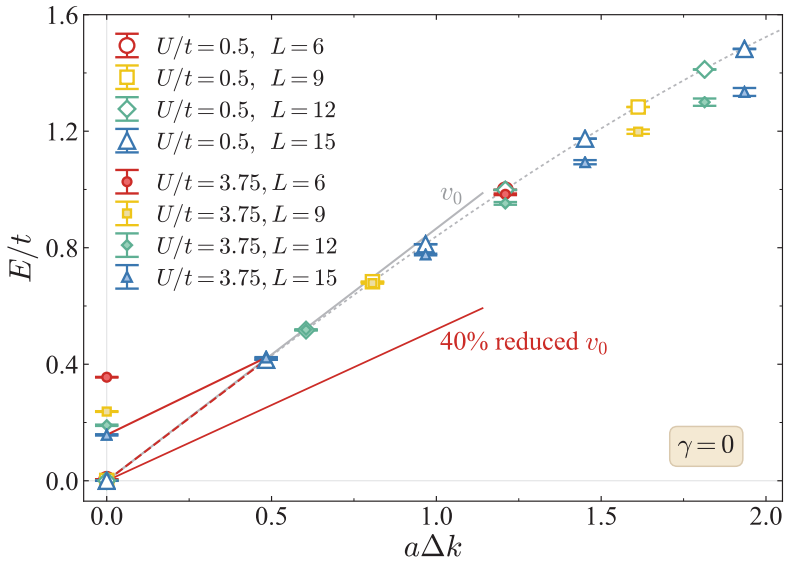

Figure 4.15: Low-energy dispersions for the Hubbard model (corresponds to $\gamma = 0$ in Ref. [69]) on the honeycomb lattice at different interaction strengths. Dependence of the lowest particle-excitation energy E on the distance $a\Delta k$ to the Dirac point for the Hubbard model on the honeycomb lattice at $U/t = 0.5$, and $U/t = 3.75$. E is deduced from the imaginary-time slope of the Green's function at the corresponding momenta for different linear lattice sizes L of the system. The dashed gray line traces the lattice dispersion relation for the tight-binding model of non-interacting fermions ($U/t = 0$). Also indicated are a linear dispersion corresponding to v_0 (gray solid line) and to the 40% decrease with respect to v_0 reported in Ref. [69] (lower red solid line), and lines that connect the excitation energy at the Dirac point to its value at the nearest neighbor momenta on the $L = 15$ lattice for $U/t = 0.5$ (dashed red line), and for $U/t = 3.75$ (upper solid red line). Figure reprinted from [4].

The overestimation of the Fermi velocity renormalization in Ref. [69] can be easily seen by plotting the single-particle energies E/t against their dependence on the distance to the Dirac points $a\Delta k$. Fig. 4.15 illustrates this fact using the published data taken from Ref. [69] (here we also switch to the notation used by Tang et al.). We observe that the energy dispersion essentially traces the free dispersion relation with only small deviations for larger momenta, both far away ($U/t = 0.5$) and in close proximity ($U/t = 3.75$) to the critical interaction strength ($U_c/t \approx 3.85$). In contrast, the claimed 40% reduction of the Fermi velocity emerges from the slope between the energy at $a\Delta k = 0$ and $a\Delta k = 0.48$, which for $U/t = 3.75$ is significantly impacted by the large finite-size effect on $E(a\Delta = 0)$.

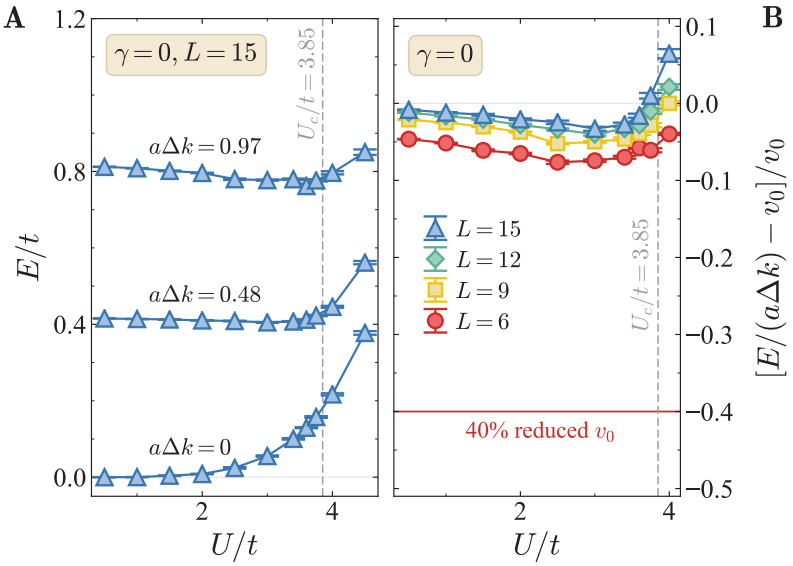

Figure 4.16: Interaction effects on the low-energy excitations for the Hubbard model on the honeycomb lattice. (A) Dependence of the lowest particle-excitation energy E on the strength of the Hubbard interaction U at the Dirac point ($a\Delta k = 0$) and at two different distances $a\Delta k = 0.48$ and 0.97 to the Dirac point for the largest accessed linear system size $L = 15$ of Ref. [69]. (B) Relative difference between v_0 and the rescaled lowest particle-excitation energy $E/(a\Delta k)$ at the closest momentum to the Dirac point on each finite lattice, as a function of the strength of the Hubbard interaction U for different system sizes L. The red solid line indicates the 40% decrease with respect to v_0 reported in Ref. [69]. In both panels the dashed vertical line gives the position of the Gross-Neveu quantum critical point from Ref. [69]. Figure reprinted from [4].

Additionally, the left panel of Fig. 4.16 shows the renormalization of the lowest energy levels as a function of the interaction U/t. We confirm that the energy at the Dirac point $E/t(a\Delta k = 0)$ is altered substantially in the vicinity of the critical point, which is related to the aforementioned crossover effect. Moreover, the next higher levels $E/t(a\Delta k = 0)$ exhibit only a small renormalization, which is indicative of a small renormalization of the Fermi velocity itself. In the right panel of Fig. 4.16 we provide a more suitable estimation of the Fermi velocity based on Eq. (4.56), which does not take the unnecessary Dirac level into account. Unsurprisingly, we find only a small decrease of the Fermi velocity of up to $v_F \approx 0.95 v_F^0$ for the investigated system sizes, which is fully consistent with the dispersion relation in Fig. 4.15. We conclude, that possible estimators for the Fermi velocity have to be taken with great care, especially in the vicinity of quantum critical points that alter the torus spectrum of the underlying field theory.

Chapter 5

Bond-ordered states and f-wave pairing of spinless fermions

Spinless fermions on the honeycomb lattice with short-range repulsive interactions feature a quantum critical point at half-filling, which separates a semi-metallic phase in the weak coupling regime from a commensurate charge-density-wave phase in the strong coupling regime. The characteristics of this quantum critical point are described by the chiral Ising fixed point of the Gross-Neveu-Yukawa field theory. In chapter 3, we investigated the thermal phase diagram close to the critical point at half-filling, and discussed its critical exponents. In chapter 4, we closely examined the torus spectrum of the same quantum critical point, which functions as a universal fingerprint of the critical theory. In this chapter, we study the same $t-V$ honeycomb model but with a finite chemical potential. Away from half-filling, the phase diagram of this model is less well established. In particular, the quantum Monte Carlo schemes described in chapter 2 rely on the particle-hole symmetry of the Hamiltonian to alleviate the sign-problem for the $t-V$ model. However, the finite chemical potential term explicitly breaks the particle-hole symmetry, and therefore the scaling of the quantum Monte Carlo simulations becomes exponential in the number of lattice sites. In this chapter, we therefore employ the functional renormalization group method [70–72] with a basic Fermi surface patching scheme to analyze the possible many-body instabilities, which emerge in this model away from half-filling. The results of this chapter have been published in Ref. [2]. I performed the functional renormalization group calculations and created the figures, while Daniel Scherer and Michael Scherer contributed parts of the code. Stefan Wessel directed the investigation.

5.1 Model definition and single-particle bases

We again consider the $t-V$ model of spinless fermions on a honeycomb lattice with nearest-neighbor interactions, but here we include a chemical potential term to tune the system beyond half-filling. The free part of the Hamiltonian then reads

$$H_0 = -t \sum_{\langle \boldsymbol{i},\boldsymbol{j}\rangle} \left(c_{\boldsymbol{i}}^\dagger c_{\boldsymbol{j}} + c_{\boldsymbol{j}}^\dagger c_{\boldsymbol{i}} \right) - \mu \sum_{\boldsymbol{i}} c_{\boldsymbol{i}}^\dagger c_{\boldsymbol{i}}. \tag{5.1}$$

The sum $\langle \boldsymbol{i}, \boldsymbol{j} \rangle$ is restricted to nearest neighbors on the honeycomb lattice. The two sublattices A and B of the honeycomb lattice generate a two-valued orbitals index. To perform a Fourier transform in this orbital basis, we define the transformed operators

$$c_{\boldsymbol{k},A} = \frac{1}{\sqrt{\mathcal{N}}} \sum_{\boldsymbol{i}\in A} \mathrm{e}^{\mathrm{i}\boldsymbol{k}\cdot\boldsymbol{i}} c_{\boldsymbol{i}}, \quad c_{\boldsymbol{k},B} = \frac{1}{\sqrt{\mathcal{N}}} \sum_{\boldsymbol{i}\in B} \mathrm{e}^{\mathrm{i}\boldsymbol{k}\cdot\boldsymbol{i}} c_{\boldsymbol{i}}, \tag{5.2}$$

where $\mathcal{N}$ is the number of two-atom unit cells, as well as the corresponding transformations for $c_{\boldsymbol{k},A/B}^\dagger = (c_{\boldsymbol{k},A/B})^\dagger$. The transformed Hamiltonian is then given by

$$H_0 = \sum_{\boldsymbol{k}} \begin{pmatrix} c_{\boldsymbol{k},A}^\dagger & c_{\boldsymbol{k},B}^\dagger \end{pmatrix} \hat{h}(\boldsymbol{k}) \begin{pmatrix} c_{\boldsymbol{k},A} \\ c_{\boldsymbol{k},B} \end{pmatrix}, \tag{5.3}$$

with the Bloch Hamiltonian

$$\hat{h}(\boldsymbol{k}) = -\begin{pmatrix} \mu & t d_{\boldsymbol{k}} \\ t d_{\boldsymbol{k}}^* & \mu \end{pmatrix}, \tag{5.4}$$

where $d_{\boldsymbol{k}} = \sum_i \mathrm{e}^{\mathrm{i}\boldsymbol{k}\cdot\boldsymbol{\delta}_i}$ and $\boldsymbol{\delta}_i$, $i = 1, 2, 3$ are the three nearest-neighbor vectors pointing from the A to the B sublattice as shown in Fig. 5.1. Note that the definition of the lattice here is rotated by 90° compared to the definition of chapters 3 and 4, and was chosen for legacy reasons. In this orbital basis, the operators $c_{\boldsymbol{k},o}, c_{\boldsymbol{k},o}^\dagger$ correspond to single-particle basis-states with Bloch momentum $\boldsymbol{k}$ and orbital index $o \in \{A, B\}$. The band basis is defined by the diagonalization of the free Hamiltonian by a unitary transformation $c_{\boldsymbol{k},o} = \sum_b u_{o,b}(\boldsymbol{k}) c_{\boldsymbol{k},b}$, such that

$$H_0 = \sum_{\boldsymbol{k}} \sum_b \left(\epsilon_b(\boldsymbol{k}) - \mu \right) c_{\boldsymbol{k},b}^\dagger c_{\boldsymbol{k},b}\,, \tag{5.5}$$

where we have defined the band index $b \in \{+, -\}$ and $\epsilon_b(\boldsymbol{k})$ is the tight-binding energy dispersion of free fermions on the honeycomb lattice.

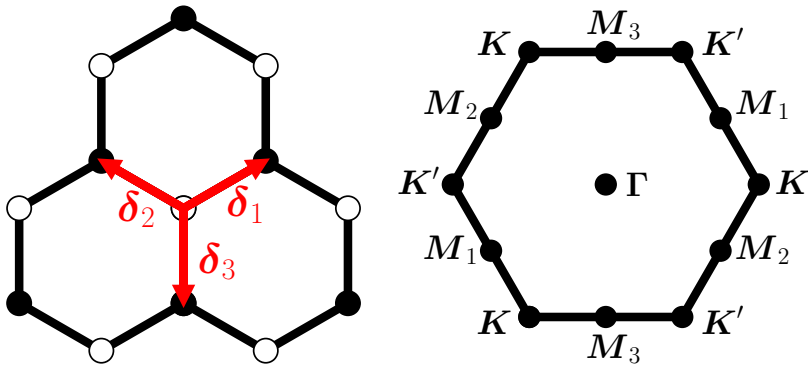

Figure 5.1: Left panel: honeycomb lattice with the two sublattices A and B indicated by white and black circles, respectively. Next-nearest neighbors are connected by the three vectors $\boldsymbol{\delta}_i$, $i = 1, 2, 3$. Right panel: Brillouin zone, with the nonequivalent high-symmetry points $\boldsymbol{\Gamma}$, $\boldsymbol{K}$, and $\boldsymbol{K}'$, as well as $\boldsymbol{M}_1$, $\boldsymbol{M}_2$, and $\boldsymbol{M}_3$ indicated as labeled. Figure reprinted from [2].

The interacting part of the Hamiltonian is given by

$$H_{\text{int}} = V \sum_{\langle \boldsymbol{i},\boldsymbol{j} \rangle} \left(c_{\boldsymbol{i}}^\dagger c_{\boldsymbol{i}} - \frac{1}{2} \right) \left(c_{\boldsymbol{j}}^\dagger c_{\boldsymbol{j}} - \frac{1}{2} \right) , \tag{5.6}$$

and it drives a continuous quantum phase transition through a fermionic quantum critical point, which has been the focus in previous chapters. Inserting the unitary transformation $c_{\boldsymbol{k},o} = \sum_b u_{o,b}(\boldsymbol{k}) c_{\boldsymbol{k},b}$ into Eq. (5.6) yields a momentum dependent interaction

$$H_{\text{int}} = \frac{1}{4} \sum_{\{b_i\}} \sum_{\{\boldsymbol{k}_i\}} V_{b_1,b_2,b_3,b_4}(\boldsymbol{k}_1, \boldsymbol{k}_2, \boldsymbol{k}_3, \boldsymbol{k}_4) \times \tag{5.7}$$
$$c_{\boldsymbol{k}_1,b_1}^\dagger c_{\boldsymbol{k}_2,b_2}^\dagger c_{\boldsymbol{k}_3,b_3} c_{\boldsymbol{k}_4,b_4} ,$$

where V_{b_1,b_2,b_3,b_4} includes anti-symmetric combinations of the $\boldsymbol{k}$-dependent interaction as well as a momentum-conserving δ-function. Further single-particle terms in Eq. (5.6) are absorbed into a chemical potential term.

Since the full Hamiltonian H is point-symmetric about the half-filled case $\mu = 0$, we can limit the fRG analysis to the regime with a negative chemical potential, $\mu < 0$, which corresponds to fermion densities below half-filling. The corresponding case of $\mu > 0$ then follows from a particle-hole transformation. It also follows directly from the analysis of the single particle (hole) problem, that the lattice is empty (full) for $\mu < -3/2V - 3t$ ($\mu > 3/2V + 3t$).

5.2 Derivation of flow equations

The basic idea of this approach is to investigate the vertex function as a function of an renormalization group flow parameter. The flow parameter represents an effective energy scale in the system, and can be implemented by a momentum or frequency cutoff in the fermionic Green function. When a Fermi surface instability arises, the renormalization group flow breaks down and the vertex function flows to the strong coupling limit, indicating a spontaneous breaking of symmetry in the system. The working principle of such an instability analysis is similar to diagrammatic ladder resummation techniques such as the random phase approximation (RPA), however, the fRG goes beyond such schemes because particle-hole and particle-particle channels are treated on an equal footing. It therefore provides an unbiased investigation of the electronic instabilities of the system. Importantly, the fRG is not restricted by the minus-sign problem, and may be employed in a broader parameter regime than the previously described quantum Monte Carlo techniques.

To detect the instabilities, we study the renormalization of the one-particle irreducible vertex function with an energy cutoff. In this approach, the energy cutoff is implemented by a infrared regulator at energy scale Λ, which is introduced into the bare propagator. The renormalization-group flow is then generated by successively integrating out fermionic degrees of freedom, starting at an initial Λ on the scale of the electronic hopping, down toward $\Lambda \to 0$. As mentioned, the fRG approach is unbiased towards any leading instability, because the RG flow includes equal contributions as well as mixing between indirect and direct particle-hole channels and the particle-particle channel. In the following, we briefly review a general formulation of fRG with Fermi surface patching, and discuss the approximations that are later used in the investigation of the $t - V$ model.

To derive the fRG flow equations, we switch from the Hamiltonian formulation to an action-based formulation of the quantum many-body system. Furthermore, we carry out the RG flow in the band basis of the original Hamiltonian. The general fermionic imaginary-time action of an interacting system is given by

$$\mathcal{S}[\Psi, \bar{\Psi}] = -\left(\bar{\Psi}, \mathcal{G}_0^{-1}\Psi\right) + \mathcal{V}[\Psi, \bar{\Psi}], \tag{5.8}$$

where $\Psi(\xi), \bar{\Psi}(\xi)$ are Grassmann fields, $\mathcal{G}_0(\xi, \xi')$ is the propagator of the non-interacting system, and $\xi = (\omega_n, \boldsymbol{k}, b)$ is a multi-index carrying the Matsubara frequency ω_n, momentum $\boldsymbol{k}$ and band index b. Writing out the scalar product of the quadratic part gives

$$\left(\bar{\Psi}, \mathcal{G}_0^{-1}\Psi\right) = \sum_{\xi,\xi'} \bar{\Psi}(\xi)[\mathcal{G}_0^{-1}](\xi, \xi')\Psi(\xi), \tag{5.9}$$

where the free propagator is diagonal with respect to the multi-index ξ, and can be expressed as

$$\mathcal{G}_0(\xi,\xi') = \mathcal{G}_0(\omega_n,\boldsymbol{k},b)\delta_{\xi,\xi'}, \tag{5.10}$$

with

$$\mathcal{G}_0(\omega_n,\boldsymbol{k},b) = \frac{1}{i\omega_n - \epsilon_b(\boldsymbol{k}) + \mu}. \tag{5.11}$$

The quartic interaction functional $\mathcal{V}$,

$$\mathcal{V}[\Psi,\bar{\Psi}] = \frac{1}{4}\sum_{\{\xi_i\}} V(\xi_1,\xi_2,\xi_3,\xi_4)\bar{\Psi}(\xi_1)\bar{\Psi}(\xi_2)\Psi(\xi_3)\Psi(\xi_4),$$

contains the bare interaction vertex in the band picture $V(\xi_1,\xi_2,\xi_3,\xi_4)$, which is obtained from Eq. (5.7) after multiplying by a δ-function for all Matsubara frequencies due to the static nature of the original interaction. One then introduces Grassmann-valued source fields $\bar{\eta}$ and η into the action and performs the functional integral, thus obtaining the generating functional for connected correlation functions,

$$G[\eta,\bar{\eta}] = -\ln\int \mathcal{D}[\bar{\Psi},\Psi]\mathrm{e}^{-\mathcal{S}[\Psi,\bar{\Psi}]+(\bar{\eta},\Psi)+(\bar{\Psi},\eta)}. \tag{5.12}$$

The generating functional Γ for one-particle irreducible (1-PI) vertices is then obtained by taking the Legendre transform with respect to the source fields,

$$\Gamma[\phi,\bar{\phi}] = (\bar{\eta},\phi) + (\bar{\phi},\eta) + G[\eta,\bar{\eta}], \tag{5.13}$$

where $\phi = -\frac{\delta}{\delta\bar{\eta}}G[\eta,\bar{\eta}]$, $\bar{\phi} = \frac{\delta}{\delta\eta}G[\eta,\bar{\eta}]$. Further, the 1-PI vertices $\Gamma^{(2n)}$ appear as the coefficients of an expansion of $\Gamma[\phi,\bar{\phi}]$ in the fields ϕ, $\bar{\phi}$.

At this point, we introduce the scale parameter Λ as an energy cutoff into the propagator, such that

$$\mathcal{G}_0(\omega_n,\boldsymbol{k},b) \to \mathcal{G}_0^{\Lambda}(\omega_n,\boldsymbol{k},b) = \frac{\Theta_\epsilon(\epsilon_b(\boldsymbol{k})-\mu)}{i\omega_n - \epsilon_b(\boldsymbol{k}) + \mu}, \tag{5.14}$$

where Θ_ϵ is taken as a smoothed Fermi function that cuts off modes with energies $|\epsilon_b(\boldsymbol{k}) - \mu| \lesssim \Lambda$. In the implementation of the code Θ_ϵ is realized by Fermi function with a very small temperature. The Λ dependence then propagates via the functional integral to the effective action $\Gamma^{\Lambda}[\phi,\bar{\phi}]$, which now generates the scale-dependent 1-PI vertex functions

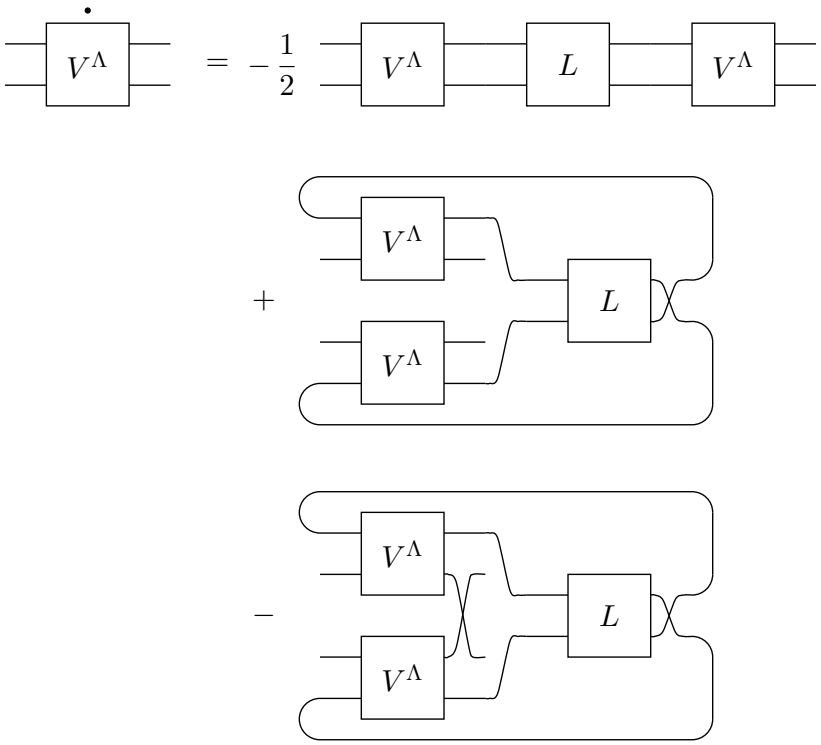

Figure 5.2: Pictorial representation of the fRG flow equation for the four-point vertex function V^Λ using Feynman diagrams. The boxes represent V^Λ and the loop kernel L, while the black dot on the left hand side indicates the scale-derivative $d/d\Lambda V^\Lambda$. Internal variables are contracted according to the connected lines, see Eq. Eq. (5.17) for the algebraic expression. The first diagram on the right hand side represents the particle-particle channel, the other two show the direct and the crossed particle-hole channel, respectively. A detailed derivation of the diagrammatic rules can be found in Ref. [73]. Figure reprinted from [2].

$\Gamma^{(2n),\Lambda}$. Taking the variation with respect to Λ generates a hierarchy of coupled flow equations for $\Gamma^{(2n),\Lambda}$, the solution of which continuously connect the bare vertices $\Gamma^{(2n),\Lambda_0}$ to the full effective vertices that emerge as $\Lambda \to 0$. The vertex functions $\Gamma^{(2n),\Lambda}$ are therefore the central objects that are monitored during the course of the renormalization-group flow.

To solve the hierarchy of flow equations numerically, they have to be significally truncated. Here, we follow the approach from Ref. [74], focusing on the flow of the 4-point vertex function $\Gamma^{(4),\Lambda}$, which is related to physical susceptibilities and is therefore suitable to detect phase transitions. We furthermore neglect the feedback of the self-energy flow $\Sigma^\Lambda = \Gamma^{(2),\Lambda}$, as well as higher order vertex functions $\Gamma^{(2n),\Lambda}$ with $n \geq 3$. At each step, we compute the vertex function $\Gamma^{(4),\Lambda}$ at some intermediate scale $0 < \Lambda < \Lambda^0$. We then check for divergences by monitoring the absolute value of the largest component, V_{max}. The flow is terminated if $V_{\text{max}} \gg \Lambda^0$, at which point we fit the last data points of $V_{\text{max}}(\Lambda)$ to determine the critical scale $\Lambda_c > 0$. The divergent structure of the critical vertex function can then be used to

analyse the type of symmetry-broken state. This truncation scheme has been shown to allow for the competition of different fluctuation channels that drive phase transitions, and has been used successfully to study instabilities in various two-dimensional fermion systems [71, 72].

Within this truncation scheme, the resulting flow equation for the four-point vertex function $V^\Lambda \equiv \Gamma^{(4),\Lambda}$ is given by

$$\frac{d}{d\Lambda} V^\Lambda = \Phi^\Lambda_{\text{pp}} + \Phi^\Lambda_{\text{ph,d}} + \Phi^\Lambda_{\text{ph,cr}}, \tag{5.15}$$

where the contributions to the right hand side are given by the particle-particle bubble Φ_{pp} as well as the direct and crossed particle-hole bubbles $\Phi_{\text{ph, d}}$ and $\Phi_{\text{ph, cr}}$. The diagrammatic representation of the flow equation Eq. (5.15) is illustrated in Fig. 5.2. Writing out all contractions, the loop contributions for the particle-particle and the direct particle-hole channel are given by

$$\begin{aligned}\Phi_{\text{pp}}(\xi_1,\xi_2,\xi_3,\xi_4) = -\frac{1}{2}\prod_{\nu=1}^{4}\int d\eta_\nu\, L(\eta_2,\eta_1,\eta_3,\eta_4) \\ \times V^\Lambda(\xi_2,\xi_1,\eta_2,\eta_3) V^\Lambda(\eta_4,\eta_1,\xi_3,\xi_4),\end{aligned} \tag{5.16}$$

$$\begin{aligned}\Phi_{\text{ph,d}}(\xi_1,\xi_2,\xi_3,\xi_4) = \prod_{\nu=1}^{4}\int d\eta_\nu\, L(\eta_1,\eta_2,\eta_3,\eta_4) \\ \times V^\Lambda(\eta_4,\xi_2,\xi_3,\eta_1) V^\Lambda(\xi_1,\eta_2,\eta_3,\xi_4),\end{aligned} \tag{5.17}$$

and the crossed particle-hole contribution is given through

$$\Phi_{\text{ph,cr}}(\xi_1,\xi_2,\xi_3,\xi_4) = -\Phi_{\text{ph,d}}(\xi_1,\xi_2,\xi_4,\xi_3)\,, \tag{5.18}$$

where the loop kernel $L = S^\Lambda \mathcal{G}_0^\Lambda + \mathcal{G}_0^\Lambda S^\Lambda$ is composed out of the bare scale-dependent propagator $\mathcal{G}_0^\Lambda$ and the single-scale propagator $S^\Lambda = -d/d\Lambda\, \mathcal{G}_0^\Lambda$, cf. Ref. [74]. Furthermore, we introduced the shorthand notation $\int d\eta$ for the integration/summation over the various loop variables. For simplicity, we focus on the static part of the vertex function $V^\Lambda(\xi_1,\xi_2,\xi_3,\xi_4)|_{\{\omega_i=0\}}$, which is expected to provide the most singular contribution at the critical scale [74]. Similar to the previous hierarchy truncation, the static approximation has been widely used to study the phase diagram of similar models [71, 72].

What remains to be done is the solution of the flow equation in Eq. (5.15). For this purpose, we perform a numerical integration for which we discretize the momentum dependence of the vertex function $V^\Lambda(\xi_1,\xi_2,\xi_3,\xi_4)$. Our goal is to project the momentum dependence of the vertex functions onto the most relevant momenta. For this reason, we employ a complete patching scheme of the first Brillouin zone, which projects the momenta $\boldsymbol{k}_1, \boldsymbol{k}_2$, and $\boldsymbol{k}_3$

onto points along the Fermi surface. This mapping can be expressed in terms of integer numbers $\pi(\boldsymbol{k}) \in [0, N-1]$, which are associated with each momentum $\boldsymbol{k}$, cf. Fig. 5.3. Here, N denotes the total number of patches. The fourth momentum $\boldsymbol{k}_4$ is given by momentum conservation and is projected onto the closest momentum patch $\pi(\boldsymbol{k}_4)$.

For the case of the $t-V$ model, the topology of the Fermi surface depends on the chemical potential μ. It changes at the Van Hove singularity point ($|\mu| = t$) from being K-point centered to Γ-point centered. Hence, we also change the evaluation of the loop kernels from being K-point centered for $|\mu| < t$ to Γ-point centered for $|\mu| > t$. Note that directly at the Van Hove singularity point, both discretization schemes can be used and provide consistent results. A pictorial representation of the patching scheme for different μ is provided in Fig. 5.3. Note that for the actual calculations, we used up to $N = 120$ patches.

As mentioned above, the integration of the flow equation is performed in the band basis. Nevertheless, the orbital basis often lends itself to an easier physical interpretation of the divergent vertex structure. After the end of the flow, we thus revert back to the original orbital basis denoted by the sublattice index $o = A, B$ via the inverse of the unitary transformation $u_{o,b}(\boldsymbol{k})$. Thereby, we obtain the static vertex function in the orbital basis as

$$V^{\Lambda}_{o_1 o_2 o_3 o_4}(\boldsymbol{k}_1, \boldsymbol{k}_2, \boldsymbol{k}_3, \boldsymbol{k}_4) = \sum_{\{b_i\},\{\boldsymbol{k}_i\}} V^{\Lambda}(\xi_1, \xi_2, \xi_3, \xi_4)|_{\{\omega_i=0\}} \times u_{o_1,b_1}(\boldsymbol{k}_1) u_{o_2,b_2}(\boldsymbol{k}_2) u^*_{o_3,b_3}(\boldsymbol{k}_3) u^*_{o_4,b_4}(\boldsymbol{k}_4).$$

Finally, it should be noted that our approach corresponds to a treatment in the grand canonical ensemble, which is appropriate in systems for which phase separation may emerge at strong interactions. Furthermore, since in the truncated flow equations self-energy feedback is absent, the chemical potential μ does not get adjusted to a constant filling, and instead it defines the filling in terms of the initial bare system.

5.3 Analysis of many-body instabilities

To establish the phase diagram of the model, we perform a scan in the $V-\mu$ space and vary the initial conditions of the RG flow accordingly. In particular, the intial condition of Eq. (5.15) is defined at the ultraviolet scale Λ_0 by the bare interaction Eq. (5.7), which depends on V, while the μ dependence is included via the propagator. In the following we analyze in detail the divergent structure of the vertex function that emerge when the RG reaches the critical scale Λ_c. Effectively ignoring all non-divergent terms, we are particularly interested in the intricate momentum structure of the remaining components. This interaction describes an

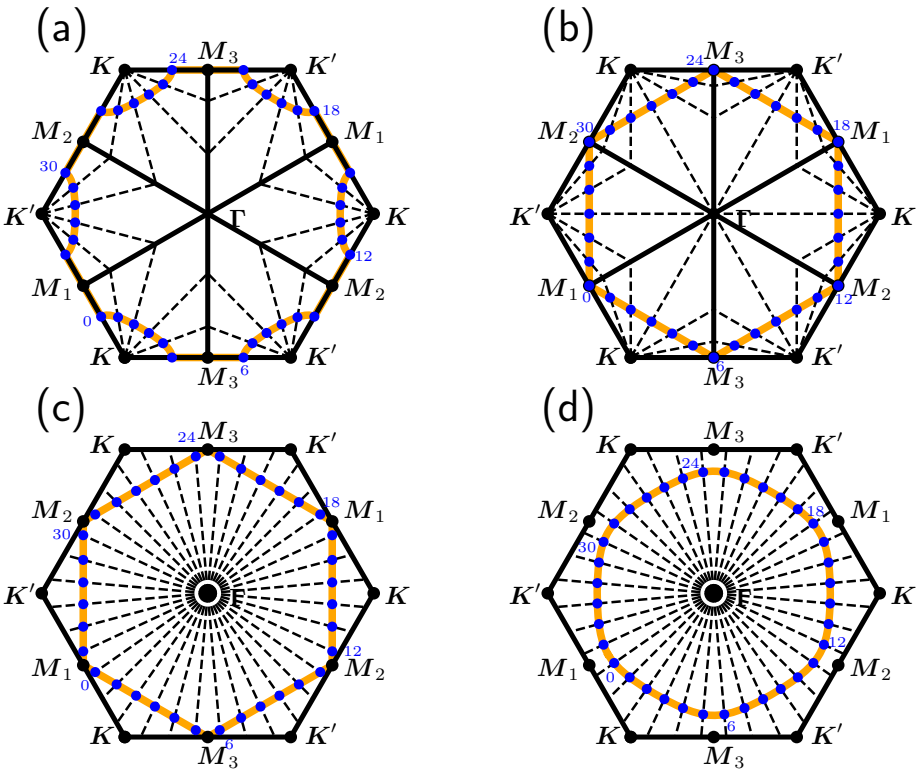

Figure 5.3: Momentum discretization schemes of the BZ for different values of the chemical potential, $\mu/t = -0.8$ (a), $\mu/t = -1$ (b,c), $\mu/t = -1.2$ (d). For better visualization, the discretization scheme is plotted here only for $N = 36$ patch points, while the actual calculations were performed with up to $N = 120$ patch points. The free Fermi surface is indicated by the orange line, and the blue points represent the projected momentum patch points. They are enumerated by the index function $\pi(\boldsymbol{k})$ in the order denoted by the blue numbers. The dashed line indicates the directions along which the numerical integration of the loop kernels are performed. In panels (a) and (b), these originate from the K and K' points and in panels (c) and (d) from the Γ point. Figure reprinted from [2].

effective low-energy Hamiltonian, which can be used to identify the leading order parameter of the symmetry broken phase. It should be noted that in the following analysis we focus only on the real part of the vertex function, while the imaginary part develops either subleading instabilities or vanishes completely. For the case of the $t - V$ model, we identify three regimes with distinguished momentum structures, which are presented in the subsequent sections.

5.3.1 Charge-density-wave instability

We begin our investigation with an instability of the (semi-)metallic ground state towards a charge-density-wave, which is already present in the case of half-filling. We find that the

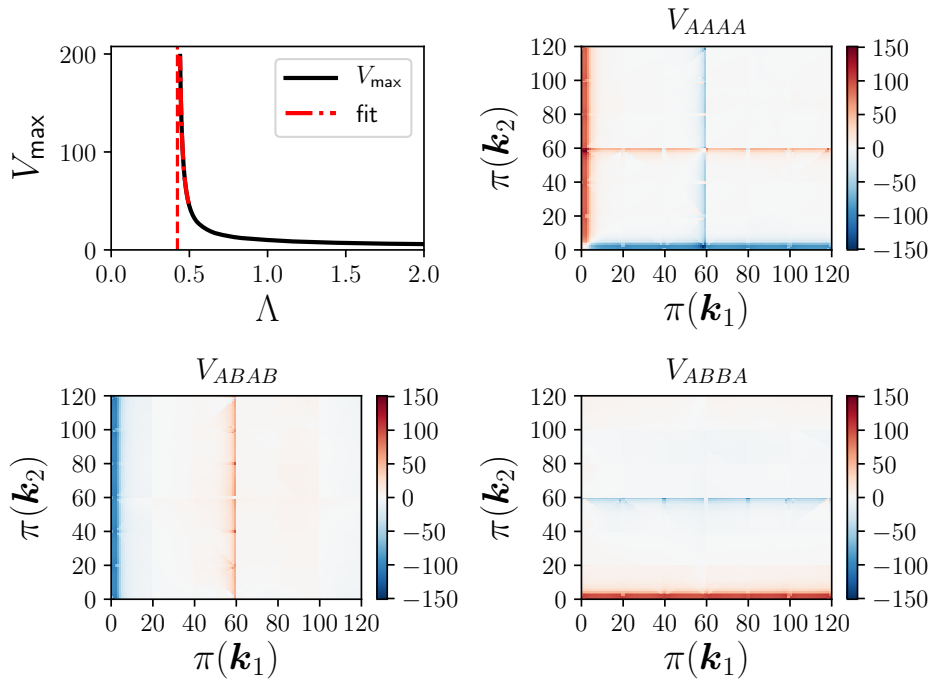

Figure 5.4: Upper left panel: Largest vertex component V_{max} as a function of the RG scale Λ for $\mu/t = -0.6$ and $V/t = 1.8$. We identify the critical scale at $\Lambda_c/t \approx 0.424$. Upper right panel and bottom panels: Vertex structure for the divergent CDW correlations for the sublattice combinations $V^{\Lambda_c}_{AAAA}$, $V^{\Lambda_c}_{ABAB}$, and $V^{\Lambda_c}_{ABBA}$, respectively. Here, we have chosen $N = 120$ patch points following the scheme indicated in Fig. 5.3 (a) and $\pi(\boldsymbol{k}_3)$ is fixed to the first patch point. The divergent wave-vector structure can be translated to the effective Hamiltonian in Eq. (5.19). Figure reprinted from [2].

same type of instability also emerges for finite values of the chemical potential beyond a critical value of the interaction, $V(\mu)$, which depends on μ. The diverging structure in the orbital basis, after a projection of the momenta onto the patch points, is shown in Fig. 5.4 for the case of $\mu = -0.6t$ and $V = 1.8t$. We identify the relevant features as (i) a vanishing momentum transfer, which is indicated by the location of the vertical/horizontal bars, and (ii) a momentum-independent structure factor. Together, these features correspond to a commensurate charge-density-wave instability, cf. also Ref. [75]. Note that the feature for $\pi(\boldsymbol{k}_1) \approx 60$ and $\pi(\boldsymbol{k}_2) \approx 60$ does not correspond to any further finite momentum transfer, it only appears as such because of the patch projection scheme. From the analysis of the vertex structure, we can reverse-engineer the effective interaction Hamiltonian close to the charge-density-wave instability as

$$H^{\Lambda_c}_{\mathrm{eff}} = -\frac{1}{\mathcal{N}} \sum_{o,o'} V_{o,o'} \epsilon_o \epsilon_{o'} N^o_{\mathbf{0}} N^{o'}_{\mathbf{0}}, \tag{5.19}$$

where $V_{o,o'} > 0$ is a constant, $\mathcal{N}$ is the number of unit cells and $\epsilon_A = +1$, $\epsilon_B = -1$ parametrize the sublattice modulation, as shown in Fig. 5.4 and previously described in Ref. [75]. Here, we introduced density operators with a general momentum transfer of $\boldsymbol{q}$, i.e. $N^o_{\boldsymbol{q}} = \sum_{\boldsymbol{k}} c^\dagger_{\boldsymbol{k}+\boldsymbol{q},o} c_{\boldsymbol{k},o}$, and the zero momentum transfer of the charge-density-wave then corresponds to $\boldsymbol{q} = \boldsymbol{0}$ for both density operators. Physically, this charge-density-wave corresponds to long-ranged density fluctuations that favors the occupation of one of the two sublattices. The unit cell of the ordering pattern is identical to the unit cell of the honeycomb lattice, as is expected from the momentum transfer. As mentioned above, the same type of instability is found in the half-filled case, where the commensurate charge-density-wave emerges at a critical value of the interaction, $V_c \approx 1.36t$.

5.3.2 Bond-order instability

When the chemical potential crosses the value of $\mu/t = -1$, the Fermi surface of the free system changes its topology from hole-like to electron-like, cf. Fig. 5.3, while directly at $\mu/t = -1$, the Fermi surface consists of straight lines that induce a perfect nesting condition. At the same time, at $\mu/t = -1$ a Van Hove singularity emerges in the density of states, which is generically found to enhance fluctuations and favor electronic instabilities over the metallic state.

Consequently, we obverse a particle-hole instability at $\mu/t = -1$ for all $V > 0$. Contrary to the commensurate charge-density-wave, the divergent part of the vertex function (cf. Fig. 5.5) indicates a finite momentum transfer of $\boldsymbol{q} = \boldsymbol{M}_i$, i.e. the three in-equivalent $\boldsymbol{M}$ points in the Brillouin zone (cf. Fig. 5.1). Furthermore, the three $\boldsymbol{M}$ points are equivalent to the three nesting vectors of the tight-binding Fermi surface up to unit vectors of the reciprocal lattice, for instance,

$$\boldsymbol{M}_2 + \boldsymbol{M}_3 \sim \boldsymbol{M}_1 \tag{5.20}$$

$$\boldsymbol{M}_1 + \boldsymbol{M}_3 \sim \boldsymbol{M}_2 \tag{5.21}$$

$$\boldsymbol{M}_1 - \boldsymbol{M}_2 \sim \boldsymbol{M}_3. \tag{5.22}$$

Based on the momentum transfer and the orbital structure of the divergent vertex function, we can express the effective interaction Hamiltonian as

$$H^{\Lambda_c}_{\text{eff}} = -\frac{1}{\mathcal{N}} \sum_{i=1}^{3} V_i \, \chi^\dagger_{\boldsymbol{M}_i} \chi_{\boldsymbol{M}_i} \tag{5.23}$$

with

$$\chi_{\boldsymbol{M}_i} = \sum_{\boldsymbol{k}} \sum_{o} f_{\boldsymbol{M}_i}(\boldsymbol{k}) c^{\dagger}_{\boldsymbol{k},o} c_{\boldsymbol{k}-\boldsymbol{M}_i,\bar{o}}, \tag{5.24}$$

and where $V_i > 0$, and $f_{\boldsymbol{M}_i}(\boldsymbol{k})$ is a non-trivial form factor that encodes the $\boldsymbol{k}$ modulation shown in Fig. 5.5.

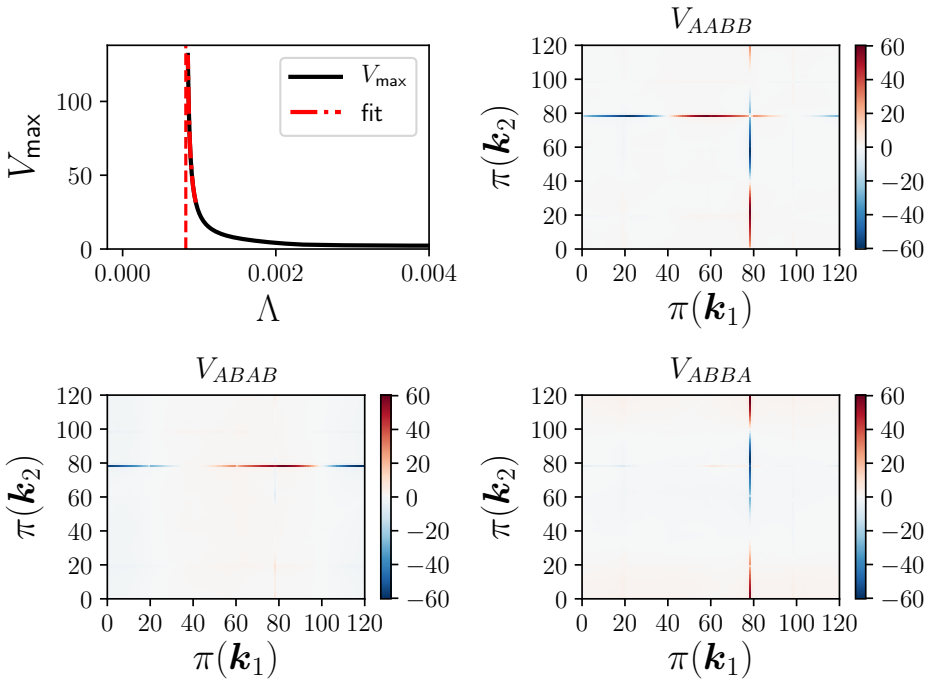

Figure 5.5: Upper left panel: Largest vertex component V_{max} as a function of the RG scale Λ for $\mu/t = -1.0$ and $V/t = 0.4$. We identify the critical scale at $\Lambda_c/t \approx 0.0008$. Upper right panel and bottom panels: Vertex structure for the divergent bond-order correlations for sublattice combinations $V^{\Lambda_c}_{AABB}$, $V^{\Lambda_c}_{ABAB}$, and $V^{\Lambda_c}_{ABBA}$, respectively. Here, we have chosen $N = 120$ patch points following the scheme indicated in Fig. 5.3 (c) and $\pi(\boldsymbol{k}_3)$ is fixed to the first patch point. The divergent wave-vector structure can be translated to the effective Hamiltonian in Eq. (5.23). Figure reprinted from [2].

The observed momentum transfer $\boldsymbol{M}_i$ is consistent with previously observed bond order phases [76], however, to investigate the instability in more details it becomes necessary to resolve the momentum dependence of the form factor $f(\boldsymbol{k})$. For this reason, we perform a projection of the form factor onto its most relevant components. This procedure is complicated by the fact Eq. (5.23) contains contributions of three different $\boldsymbol{M}$ points, as well as a limited momentum resolution due to the Fermi patch projection. We therefore simplify the component analysis by parametrizing the divergent vertex components into matrix form,

such that

$$V_{ABAB}(\mathbf{k},\mathbf{k}') = V^{\Lambda_c}_{ABAB}(\mathbf{k},\mathbf{k}',\mathbf{k}'-\mathbf{q},\mathbf{k}+\mathbf{q}), \tag{5.25}$$

$$V_{ABBA}(\mathbf{k},\mathbf{k}') = V^{\Lambda_c}_{ABBA}(\mathbf{k},\mathbf{k}',\mathbf{k}+\mathbf{q},\mathbf{k}'-\mathbf{q}), \tag{5.26}$$

where $\boldsymbol{q}$ is one of the nesting vectors $\boldsymbol{M}_i$, and we restrict $\boldsymbol{k}$ and $\boldsymbol{k}'$ to patches that are connect by $\boldsymbol{q}$. Note that the parametrization for V_{AABB} is a combination of V_{ABAB} and V_{ABBA}, as indicated in Fig. 5.5.

We now employ a singular value decomposition on the matrices V_{ABAB} and V_{ABBA} to isolate the dominant eigenmodes. For both matrices, we find two dominant eigenmodes, whose singular values are several orders of magnitude larger than those of the remaining eigenmodes. Moreover, we observe that the eigenmodes of $V_{ABAB}(\boldsymbol{k},\boldsymbol{k}')$ and $V_{ABBA}(\boldsymbol{k},\boldsymbol{k}')$ respectively are related to each other by a sign factor due to fermionic exchange.

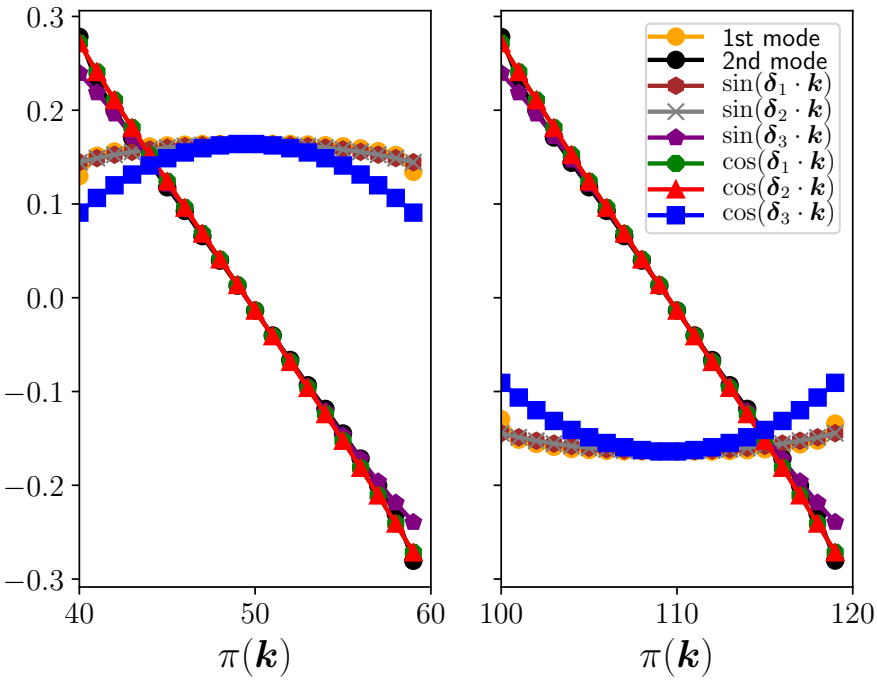

Figure 5.6: Comparison of the two dominant eigenmodes of $V_{ABBA}(\mathbf{k},\mathbf{k}')$ with the harmonic BO form factors. The functions are evaluated over points of the Fermi surface connected by the same nesting vector $\boldsymbol{q} = \boldsymbol{M}_3$, and the prefactor of the form factor was scaled to match the eigenmodes at the central momenta. Figure reprinted from [2].

We plot in Fig. 5.6 the two dominant eigenmodes $V_{ABBA}(\boldsymbol{k},\boldsymbol{k}')$ over the connected momentum patches for $\boldsymbol{q} = \boldsymbol{M}_3$. Additionally, we compare the eigenmodes to harmonic form factors proportional to $\sin(\boldsymbol{\delta}\cdot\mathbf{k})$ and $\cos(\boldsymbol{\delta}\cdot\mathbf{k})$, where the vector $\boldsymbol{\delta} = \boldsymbol{\delta}_i$, $i = 1,2,3$, connects nearest-neighbor bonds as illustrated in Fig. 5.1. We have performed a similar

comparisons for $\boldsymbol{q} = \boldsymbol{M}_1$ and $\boldsymbol{q} = \boldsymbol{M}_2$. The overall match between the eigenmodes and the lattice harmonics is satisfactory, which leads us to the conclusion that the form factors in Eq. (5.23) are primarily comprised of $\sin(\boldsymbol{\delta} \cdot \mathbf{k})$ and $\cos(\boldsymbol{\delta} \cdot \mathbf{k})$ terms. In accordance with our previous hypothesis, these same form factors have been established as characteristics of bond order instabilities in previous work [76].

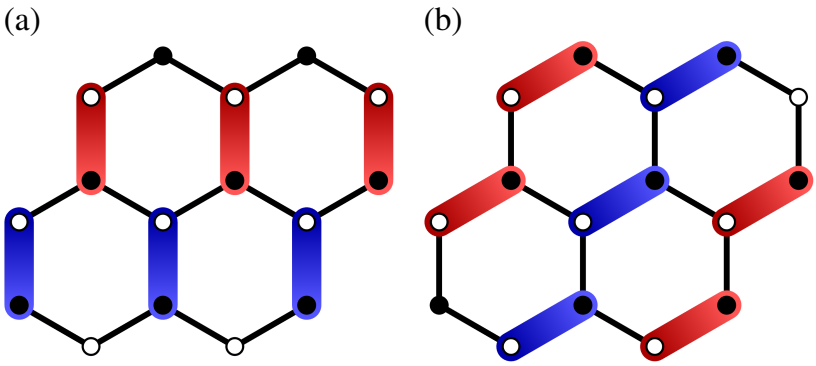

Figure 5.7: Schematic real-space hopping renormalization due to a finite bond-order parameter $\langle \chi_{\mathbf{M}_i} \rangle$. The white and black disks denote the lattice sites of the A and B sublattice, respectively. The bonds shown in red (blue) correspond to an increase (decrease) of the nearest-neighbor hopping amplitude along a given bond (pointing from the A to the B sublattice). If $\boldsymbol{q} = \boldsymbol{M}_i$ is parallel to $\boldsymbol{\delta}$, the resulting BO pattern corresponds to the one shown in panel (a). There are three such states, related by rotations. For $\boldsymbol{q} = \boldsymbol{M}_i$ not parallel to $\boldsymbol{\delta}$, a patten such as the one shown in panel (b) results instead. There are a total of six such states, related by rotations or reflections. Figure reprinted from [2].

We may now perform the Fourier transform of the form factors back to real space, which reveals a renormalization of the hopping amplitude with a doubled unit cell [76], as shown in Fig. 5.7. The doubling of the unit cell is caused by the momentum transfer of $\boldsymbol{q} = \boldsymbol{M}_i$. The comparison of the form factor terms still leaves some ambiguity about the nature of the bond order pattern. In particular, we find two different types of bond order patterns, which are distinguished by the scalar product $\boldsymbol{\delta} \cdot \boldsymbol{M}_i$ in the form factors. If $\boldsymbol{q}$ is parallel to δ, the resulting bond order pattern is characterized by equal amplitudes on parallel dimers across the hexagons, as illustrated in Fig. 5.7(a). This pattern is three-fold degenerate due to possible rotations of the lattice. Conversely, if $\boldsymbol{q}$ not parallel to $\boldsymbol{\delta}$, the bond order pattern exhibits zig-zag lines of equal amplitude bonds, as shown in Fig. 5.7 (b). This pattern is six-fold degenerate due to rotations and reflections of the lattice. Finally, we note that within our approach, we cannot determine which of these bond order patterns will form the true many-body ground state.

5.3.3 Superconducting f-wave instability

The final instability type we encounter in this model exhibits divergent features in the particle-particle channel, as opposed to the particle-hole channel, as was the case for the charge-density-wave and bond order phase. It only appears beyond the Van Hove singular, i.e. $\mu/t < -1$, where the Fermi surface is centered around the Γ point and becomes approximately circular. In the vertex function, a divergence in the particle-particle channels exhibits a characteristic diagonal structure, as depicted in Fig. 5.8. Physically, this corresponds to a coupling of two fermions with momenta $\boldsymbol{k}$ and $-\boldsymbol{k}$, which indicates the formation of Cooper pairs. This type of instability therefore corresponds a superconducting phase.

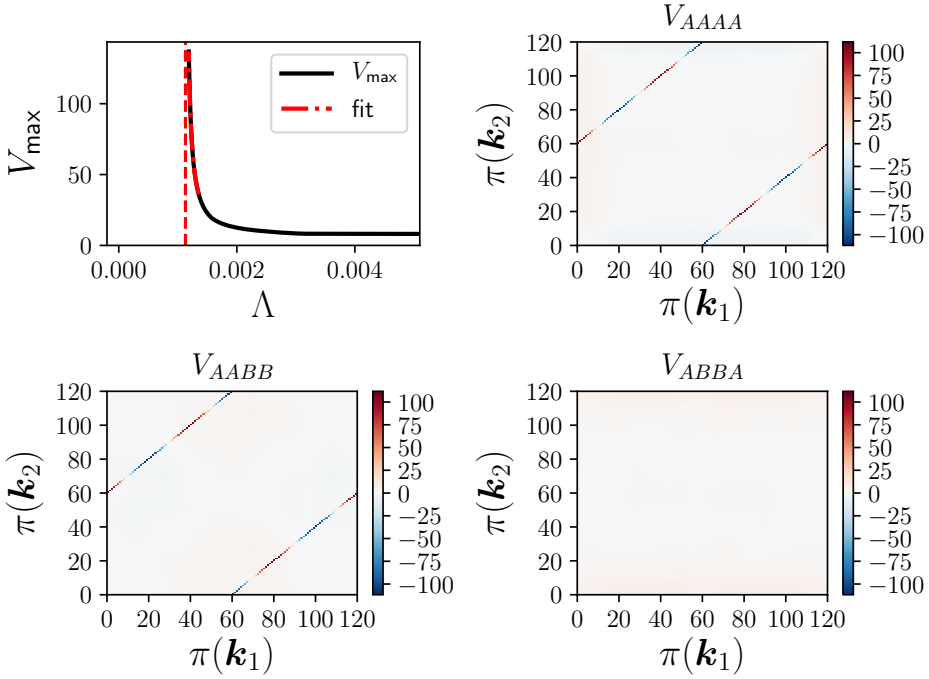

Figure 5.8: Upper left panel: Largest vertex component V_{max} as a function of the RG scale Λ for $\mu/t = -1.4$ and $V/t = 1.0$. We identify the critical scale at $\Lambda_c/t \approx 0.0011$. Upper right panel and bottom panels: Vertex structure for the divergent f-wave correlations for sublattice combinations $V^{\Lambda_c}_{AAAA}$, $V^{\Lambda_c}_{AABB}$, and $V^{\Lambda_c}_{ABBA}$, respectively. Here, we have chosen $N = 120$ patch points following the scheme indicated in Fig. 5.3 (d) and $\pi(\boldsymbol{k}_3)$ is fixed to the first patch point. The divergent wave-vector structure can be translated to the effective Hamiltonian in Eq. (5.27). Figure reprinted from [2].

The form of the effective interaction Hamiltonian can be reduced to

$$H^{\Lambda_c}_{\text{eff}} = -\frac{1}{\mathcal{N}} \sum_{o,o'} V_{oo'} \Phi^\dagger_o \Phi_{o'}, \tag{5.27}$$

with the superconducting order parameter

$$\Phi_o = \sum_{\boldsymbol{k}} f(\boldsymbol{k})\, c_{-\boldsymbol{k},o} c_{\boldsymbol{k},o}. \tag{5.28}$$

Superconducting phases can be further categorized by the spatial symmetry properties of the order parameter. In Eq. (5.27) this symmetry property is encoded in orbital dependence as well as the form factor $f(\boldsymbol{k})$. We note that the vertex function only shows divergent features in the intra-sublattice components, while inter-sublattice components remain finite. This is consistent with a suppression of pairing correlations within the unit cell due to the nearest-neighbor repulsion. To determine the form factor up to a constant prefactor, we trace the momentum dependence of the diagonal in Fig. 5.8. The result is shown in left panel of Fig. 5.9. We observe that the form factor changes its sign at momenta where the $\Gamma - K$ lines cross the Fermi surface. From this sign structure, we conclude a f-wave symmetry of the order parameter. To be more precise, we fit the form factor to the lattice harmonic

$$f_{B_{1u}}(\boldsymbol{k}) \sim \sin(3k_y) - 2\sin\left(\frac{3}{2}k_y\right)\cos\left(\frac{3\sqrt{3}}{2}k_x\right), \tag{5.29}$$

which corresponds to the B_{1u} irreducible representation of the D_{6h} symmetry [77]. After determining the momentum dependence of the form factor $f(\boldsymbol{k})$ we can again perform the Fourier transform back to real space. This yields a pattern of phase factors between second-nearest neighbors within the same sublattice, which is depicted in Fig. 5.9.

To summarize, we find that the instability in the particle-particle channel corresponds to an f-wave superconducting phase. In principle, the form factor could also include harmonic contributions of different symmetry. Note however, that due to the spinless nature of the fermions only superconducting triplet states are permitted by symmetry, which includes both p-wave f-wave symmetries. Empirically, we observe that all p-wave contributions vanish and only the B_{1u} term is present in the form factor. We attribute the suppression of the p-wave components to the fact the repulsive bare interaction potentially suppresses the formation of nearest-neighbor pairing, which are dominant terms in the p-wave form factors. Regarding the nature of the f-wave form factor, we attribute the formation of the extended $f_{B_{1u}}$ over the more compact $f_{B_{2u}}$ pairing state to a potential instability towards the competing the charge-density-wave state. The enhanced pairing between 2nd-nearest neighbor bonds in the $f_{B_{2u}}$ state would also favor the formation of the charge-density-wave, which is overall a more robust state and should lead to the breaking of the Cooper pairs. In contrast, the more spatially extended wave-function of the $f_{B_{1u}}$ pairing state should be less prone to pair breaking due to repulsive interactions.

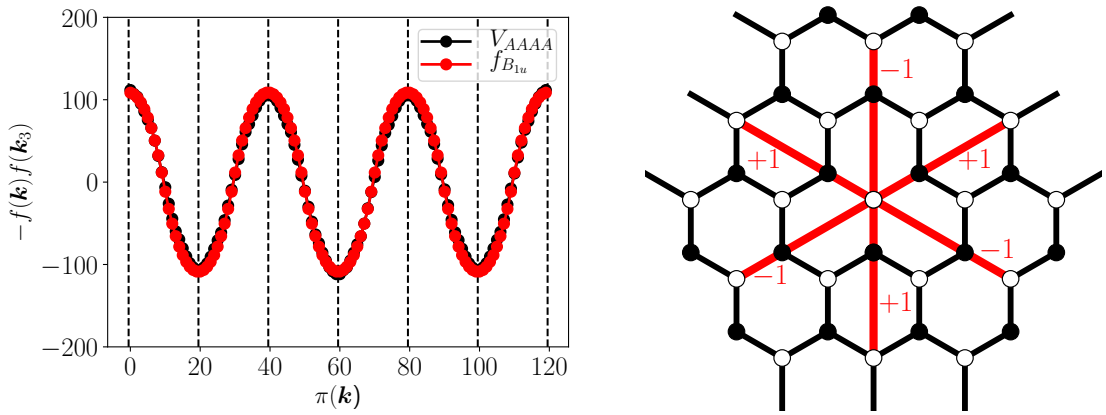

Figure 5.9: Left panel: Diagonal $V^{\Lambda_c}_{AAAA}$ vertex structure along the Fermi surface. We fix the third momentum to $\pi(\boldsymbol{k}_3) = 1$ and perform a fit to the B_{1u} lattice harmonic function $f_{B_{1u}}(\boldsymbol{k}) \sim \sin(3k_y) - 2\sin(\frac{3}{2}k_y)\cos(\frac{3\sqrt{3}}{2}k_x)$. Right panel: Real-space pairing form factor corresponding to the lattice harmonic function B_{1u} on the honeycomb lattice, with the two sublattices A and B indicated by blue and green circles, respectively. The numbers ± 1 along the (red) lines to the second-nearest equal-sublattice neighbors of the central site denote phase factors of the corresponding B_{1u} pairing state. Figure reprinted from [2].

To understand the formation of the f-wave instability in more detail, we track the evolution of the vertex function during the flow, cf. Fig. 5.10, features snapshots of V_{AAAA} from $\Lambda = \Lambda^0$ down to $\Lambda \approx \Lambda_c$. We find that during the flow, the vertex function develops first features similar those of the charge-density-wave. The repulsive interaction of these features then meditate an effective attractive interaction in the particle-particle channel, which grows large upon approaching the critical scale. Eventually, the pairing instability becomes dominant, and the charge-density-wave type features become sub-leading. Interestingly, the phase of the pairing state is pinned to the sign structure of the effective intermediate vertex, such that is matches the B_{1u} form factor.

Furthermore, we note that the charge fluctuations in the particle-hole channels are essential to obtain any type of instability. This can be demonstrated by excluding the particle-hole channels $\Phi_{\text{ph,d}}$ and $\Phi_{\text{ph,cr}}$ from the flow Eq. 5.15, which prevents the formation of the instability. Similarly, the feedback of the particle-particle channel is crucial to suppress the formation of the charge-density-wave instability. Upon excluding the particle-particle bubble Φ_{pp}, we find a charge-density-wave instability in place of the f-wave superconducting instability. The critical scales of the charge-density-wave without particle-particle bubble are always larger than the ones of the f-wave instability. The feedback of the particle-particle channel therefore leads to a competition between the two phases, which favors the superconducting phase in a parameter regime for $|\mu| > t$, while the charge-density-wave is favored for $|mu| < t$ and for large V.

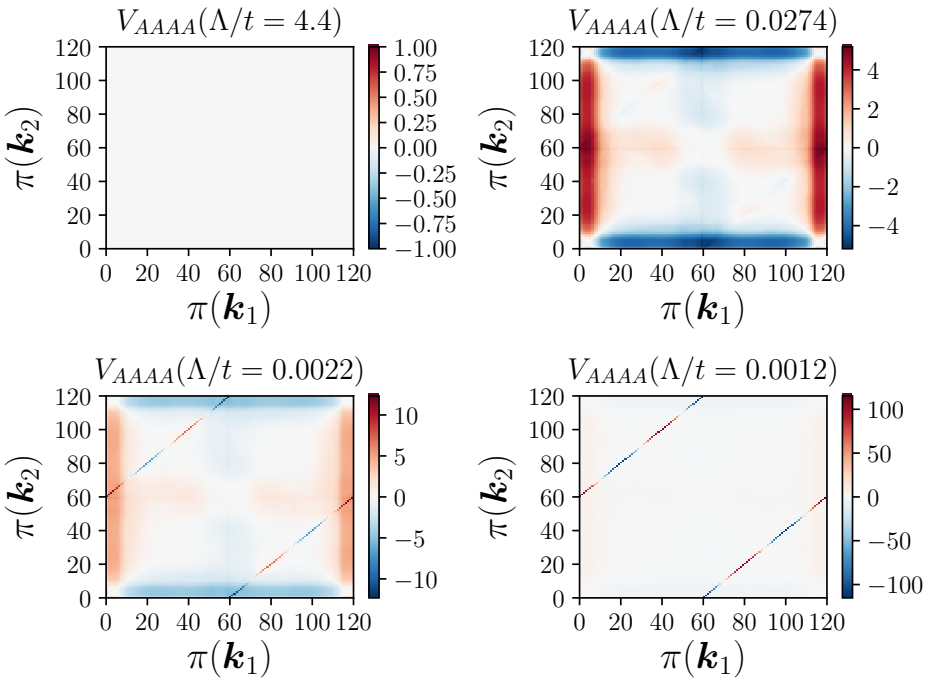

Figure 5.10: Evolution of the V_{AAAA} vertex component, shown at various values of the scale Λ during the flow. The model parameters are the same as in Fig. 5.8. Figure reprinted from [2].

5.4 Discussion of the phase diagram

We can summarize our findings of the instability analysis by the phase diagram shown in Fig. 5.11, which depicts the leading instabilities for the parameter ranges $|\mu|/t \leq 2$ and $V/t \leq 2$. The phase diagram is constructed by performing a uniform scan in this parameter regime, and then determining the leading instability as described in the previous sections. The mirror symmetry of the phase diagram about the half-filled case of $\mu = 0$ is enforced by the particle-hole symmetry of the $t - V$ model, which allows the mapping of $\mu \to -\mu$, and this is also recovered by our fRG scheme.

We note that for the half-filled case, the Fermi surface patching is not well-defined. That is because the Fermi surface only contains Fermi points, which are located at the Dirac cones. The momentum patches are then projected onto a circular pattern around the Dirac points, with a small but arbitrary radius. This Fermi point patching has to be performed carefully, and in Ref. [75] it has been reported that additional projection rings were required to obtain the correct critical behavior. At finite μ the Fermi surface becomes non-singular, such that this complication does not arise. Nevertheless, for $\mu = 0$ and a single projection ring, our fRG scheme essentially reproduces the mean-field result for the semi-metal to charge-density-wave transition.

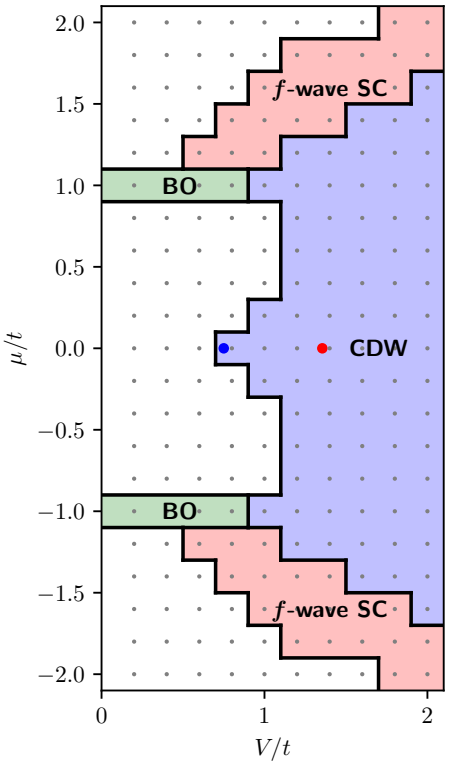

Figure 5.11: Tentative phase diagram of spinless fermions on the honeycomb lattice with nearest-neighbor repulsion V and chemical potential μ, given in units of the nearest-neighbor hopping amplitude t. At $\mu = 0$, the transition from the semi-metallic to the commensurate CDW phase in mean-field theory is given by $V_c^{\mathrm{MF}} \approx 0.75t$ (blue dot) and from quantum Monte Carlo simulations by $V_c^{\mathrm{QMC}} \approx 1.36t$ (red dot). For this phase diagram, we have evaluated the flow equations with the patching schemes from Fig. 5.3, resolving instabilities down to scale of $\Lambda/t = 10^{-7}$, and we have chosen a wave vector resolution of $N = 120$ patches in the Brillouin zone. The initial parameters of the flow are indicated by the grey dots. Figure reprinted from [2].

For $|\mu|/t < t$, we find again an instability towards the commensurate charge-density-wave, which has the same characteristics as the one found for half-filling. Moreover, we observe that any filling, the system is eventually driven towards the same charge-density-wave instability. This limiting behavior is also expected from the formal $V \gg t$ limit of the spinless $t - V$ model, which maps onto an antiferromagnetic Ising model,

$$H_I = J \sum_{\langle i,j \rangle} \sigma_i \sigma_j - h \sum_i \sigma_i, \tag{5.30}$$

with full (empty) sites represented by $\sigma_i = +1$ ($\sigma_i = -1$). After performing the large-V limit, the model parameters transform according to $J = V/4 > 0$ and $h = \mu/2$. As a function of the

field h, this Ising model hosts an anti-ferromagnetic ground state for $|h| < 3J$, and it is fully polarized up (down) for $h > 3J$ ($h < -3J$). This insight can be mapped back to the spinless $t - V$ model, which for $V \gg t$ permits either a fully occupied lattice, an empty lattice, or the commensurate charge-density-wave encountered at half-filling. Physically, this situation the system is then characterized by phase separation in the canonical ensemble. It is encouraging, that our fRG scheme reproduces this strong-coupling behavior correctly. Moreover, the same occurrence of the commensurate charge-density-wave at large interactions was also found in studies of hard-core bosons with nearest-neighbor repulsions on the honeycomb lattice [78, 79]. Finally, we note that in the (semi-)metallic region of the phase diagram, we can exclude a Kohn-Luttinger instability down to critical scales of $\Lambda/t = 10^{-7}$, where we stopped the integration of an otherwise regular flow.

As noted above, the bond-order instability only occurs in direct vicinity to the Van Hove filling, $|\mu| = 1$. This is consistent with the bond orders' dependence on the perfect nesting condition, which only occurs at this filling. Furthermore, the Van Hove singularity in the density of states boosts the particle-hole fluctuations, such that the instability already arises for infinitesimally small interactions. At $V/t \approx 1.0$ and $|\mu|/t \approx 1.0$ in the phase diagram, combined bond-order, charge-density-wave and superconducting fluctuations become relevant in the flow and compete with each other. Upon increasing V, the charge-density-wave fluctuations become dominant, while increasing $|\mu|$ degrades the nesting of the Fermi surface, which eventually leads to dominant fluctuations in the particle-particle channel. Overall, we find that the critical scales for the f-wave superconducting instability are significantly smaller compared to both the bond-order instability and the charge-density-wave instability. We would therefore expect the superconducting phase to be only stable up to small temperatures $T \ll t$, whereas both charge ordered phases should be stable up to larger temperatures $T \gtrsim t$.

Chapter 6

Conclusion

In this thesis I have set out to study various examples of quantum critical phenomena in two-dimensional fermion systems. The basis for this investigation has been a systems of spinless fermions on the honeycomb lattice. The honeycomb lattice has unique properties, which lead to a relativistic dispersion and hence the emergence of Dirac fermions in its effective description. These introductory details are the topic of chapter 1. The interesting physics that arise can then be described from different points of view.

Firstly, we construct the $t-V$ model of spinless fermions on the honeycomb lattice. This lattice model features a quantum critical point of the chiral Ising kind. The properties and characteristics of the associated quantum phase transition found in the $t-V$ model may be studied using different numerical techniques. In this thesis, I focused on two complimentary approaches.

On the one hand, chapter 2 details a variety of quantum Monte Carlo techniques, which are suitable to simulate the $t-V$ model. The most compelling advantage of these quantum Monte Carlo algorithms is that they are able to provide exact results up to a controlled statistical error. Depending on which physical quantities are of interest, one can use either a finite temperature formulation, or one can employ a projector scheme to simulate the system at zero temperature. Nevertheless, both of these methods are limited by finite system sizes, as well as the Monte Carlo sign-problem, which effectively limits the parameter regime which can be simulated efficiently. The case of the $t-V$ model is of particular interest in regards to the sign problem, because it was only relatively recently discovered how the sign problem can be circumvented in this model. This discovery has lead to further insights into possible solutions for the sign problem of other models. It will be interesting to see if similar advances in quantum Monte Carlo algorithms will open up even more models in the future.

I have employed different quantum Monte Carlo algorithms to study the distinct characteristics of the chiral Ising quantum critical point. Chapter 3 deals with the finite temperatures

phase transitions, which are found in the vicinity of said quantum critical point. The quantum phase transition, even though it takes place strictly at zero temperature, still impacts the nature of the temperature-interaction phase diagram. We have identified different scaling regimes, in which characteristic scaling behavior of both quantum and thermal phase transitions are found. Finally, we obtained estimates for the chiral Ising critical exponents. However, the exact values for some of these exponents have been a topic of debate for some time – unfortunately, we were not able to answer this question with definitive authority.

With the intend to overcome the problems of critical exponent calculations, chapter 4 contains a novel approach to characterize quantum critical points via torus spectrum spectroscopy, which may be used complementary to the traditional study of critical exponents. The torus spectroscopy approach is more closely related to the field theory description of the chiral Ising fixed point of the Gross-Neveu-Yukawa conformal field theory. The energy levels of the lattice system, which is defined on a torus, provide universal values characteristic of the critical theory. At the same time, the quantum numbers and multiplicities of the low-energy eigenstates yield qualitative characteristics dictated by the critical theory. The torus spectrum of the chiral Ising fixed point is an important extension of previously studied Wilson-Fisher torus spectrum. Further studies of critical field theories of interest, such as the QED_3-Gross-Neveu-Yukawa gauge theory, will benefit from the insights provided by the chiral Ising torus spectrum.

Another interesting prospect is the addition of an extended inter-unit-cell hopping t'' to the $t - V$ model. The hopping ratio t''/t can then be fine tuned such that the Dirac cones with linear dispersion become quadratic band touching points. The quadratic band touching point should boost quantum fluctuations because the density of states no longer vanishes at the Fermi points. Therefore, by conventional wisdom, one would expect to find an instability directly at infinitesimal interactions. Nevertheless, it seems that quadratic band touching points allow for stable phases afterall, as was first shown for the case of bilayer graphene [80, 81]. The $t - t'' - V$ is a favourable playground for such investigations because the quadratic dispersion can be created by simply adding another hopping parameter [82], whereas otherwise, such as in the case of the bilayer Hubbard model, the addition of a whole particle layer is required.

On the other hand, in chapter 5 the functional renormalization group method is used to classify possible phases of the $t - V$ model upon introducing a chemical potential μ. Going beyond half-filling, the particle-hole symmetry is explicitly broken and the quantum Monte Carlo algorithms can no longer be formulated sign-problem-free. Fortunately, the Fermi surface patching scheme of the fRG is more flexible, and allowed us to investigate the instability of the system towards possible symmetry broken phases. In addition to the

commensurate charge-density-wave of the half-filled system, we found evidence for an additional bond order phase, located at the Van Hove filling, as well as a superconducting phase with an f-wave symmetric order parameter. Even though we employed a rather basic fRG scheme with several approximations, the results are consistent with the known limits of the model. Currently, novel fRG formulations are being developed, which have the potential to provide also quantitative results comparable with those of numerical exact methods. In the future, it will be interesting to bridge the gap between fRG and quantum Monte Carlo simulations for the $t - V$ model and related lattice fermion models.

Bibliography

[1] S. Hesselmann and S. Wessel, Thermal Ising transitions in the vicinity of two-dimensional quantum critical points, Phys. Rev. B **93**, 155157 (2016).

[2] S. Hesselmann, D. D. Scherer, M. M. Scherer, and S. Wessel, Bond-ordered states and f-wave pairing of spinless fermions on the honeycomb lattice, Phys. Rev. B **98**, 045142 (2018).

[3] M. Schuler, S. Hesselmann, S. Whitsitt, T. C. Lang, S. Wessel, and A. M. Läuchli, Torus spectroscopy of the gross-neveu-yukawa quantum field theory: Free dirac versus chiral ising fixed point, arXiv:1907.05373 .

[4] S. Hesselmann, T. C. Lang, M. Schuler, S. Wessel, and A. M. Läuchli, Comment on "the role of electron-electron interactions in two-dimensional dirac fermions", Science **366** (2019).

[5] V. L. Ginzburg and L. D. Landau, On the Theory of superconductivity, Zh. Eksp. Teor. Fiz. **20**, 1064 (1950).

[6] S. Sachdev, *Quantum Phase Transitions* (Cambridge Univ. Press, 2011).

[7] A. H. Castro Neto, F. Guinea, N. M. R. Peres, K. S. Novoselov, and A. K. Geim, The electronic properties of graphene, Rev. Mod. Phys. **81**, 109 (2009).

[8] I. F. Herbut, Interactions and Phase Transitions on Graphene's Honeycomb Lattice, Phys. Rev. Lett. **97**, 146401 (2006).

[9] I. F. Herbut, V. Juričić, and B. Roy, Theory of interacting electrons on the honeycomb lattice, Phys. Rev. B **79**, 085116 (2009).

[10] B. Ihrig, L. N. Mihaila, and M. M. Scherer, Critical behavior of Dirac fermions from perturbative renormalization, Phys. Rev. B **98**, 125109 (2018).

[11] J. Zinn-Justin, Four-fermion interaction near four dimensions, Nucl. Phys. B **367**, 105 (1991).

[12] B. Rosenstein, H.-L. Yu, and A. Kovner, Critical exponents of new universality classes, Physics Letters B **314**, 381 (1993).

[13] A. N. Rubtsov, V. V. Savkin, and A. I. Lichtenstein, Continuous-time quantum monte carlo method for fermions, Phys. Rev. B **72**, 035122 (2005).

[14] R. Blankenbecler, D. J. Scalapino, and R. L. Sugar, Monte carlo calculations of coupled boson-fermion systems. i, Phys. Rev. D **24**, 2278 (1981).

[15] D. J. Scalapino and R. L. Sugar, Monte carlo calculations of coupled boson-fermion systems. ii, Phys. Rev. B **24**, 4295 (1981).

[16] S. R. White, D. J. Scalapino, R. L. Sugar, E. Y. Loh, J. E. Gubernatis, and R. T. Scalettar, Numerical study of the two-dimensional hubbard model, Phys. Rev. B **40**, 506 (1989).

[17] M. Iazzi and M. Troyer, Efficient continuous-time quantum monte carlo algorithm for fermionic lattice models, Phys. Rev. B **91**, 241118 (2015).

[18] L. Wang, M. Iazzi, P. Corboz, and M. Troyer, Efficient continuous-time quantum monte carlo method for the ground state of correlated fermions, Phys. Rev. B **91**, 235151 (2015).

[19] N. Metropolis, A. W. Rosenbluth, M. N. Rosenbluth, A. H. Teller, and E. Teller, Equations of state calculations by fast computing machines, J. Chem. Phys. **21**, 1087 (1953).

[20] H. F. Trotter, On the product of semi-groups of operators, Proc. Amer. Math. Soc. **10**, 545 (1959).

[21] M. Suzuki, Generalized trotter's formula and systematic approximants of exponential operators and inner derivations with applications to many-body problems, Communications in Mathematical Physics **51**, 183 (1976).

[22] L. Wang, P. Corboz, and M. Troyer, Fermionic quantum critical point of spinless fermions on a honeycomb lattice, New Journal of Physics **16**, 103008 (2014).

[23] E. F. Huffman and S. Chandrasekharan, Solution to sign problems in half-filled spin-polarized electronic systems, Phys. Rev. B **89**, 111101 (2014).

[24] R. R. d. Santos, Introduction to quantum Monte Carlo simulations for fermionic systems, Brazilian Journal of Physics **33**, 36 (2003).

[25] F. Assaad and H. Evertz, World-line and determinantal quantum monte carlo methods for spins, phonons and electrons, in *Computational Many-Particle Physics*, edited by H. Fehske, R. Schneider, and A. Weiße (Springer Berlin Heidelberg, Berlin, Heidelberg, 2008) pp. 277–356.

[26] M. Feldbacher and F. F. Assaad, Efficient calculation of imaginary-time-displaced correlation functions in the projector auxiliary-field quantum monte carlo algorithm, Phys. Rev. B **63**, 073105 (2001).

[27] P. K. V. V. Nukala, T. A. Maier, M. S. Summers, G. Alvarez, and T. C. Schulthess, Fast update algorithm for the quantum monte carlo simulation of the hubbard model, Phys. Rev. B **80**, 195111 (2009).

[28] K. Binder, Finite size scaling analysis of ising model block distribution functions, Zeitschrift für Physik B Condensed Matter **43**, 119 (1981).

[29] P. Gunacker, M. Wallerberger, E. Gull, A. Hausoel, G. Sangiovanni, and K. Held, Continuous-time quantum monte carlo using worm sampling, Phys. Rev. B **92**, 155102 (2015).

[30] J. E. Hirsch, Stable monte carlo algorithm for fermion lattice systems at low temperatures, Phys. Rev. B **38**, 12023 (1988).

[31] L. Wang, Y.-H. Liu, M. Iazzi, M. Troyer, and G. Harcos, Split orthogonal group: A guiding principle for sign-problem-free fermionic simulations, Phys. Rev. Lett. **115**, 250601 (2015).

[32] Z.-X. Li, Y.-F. Jiang, and H. Yao, Solving the fermion sign problem in quantum monte carlo simulations by majorana representation, Phys. Rev. B **91**, 241117 (2015).

[33] Z.-X. Li, Y.-F. Jiang, and H. Yao, Fermion-sign-free majarana-quantum-monte-carlo studies of quantum critical phenomena of dirac fermions in two dimensions, New Journal of Physics **17**, 085003 (2015).

[34] D. J. Gross and A. Neveu, Dynamical symmetry breaking in asymptotically free field theories, Phys. Rev. D **10**, 3235 (1974).

[35] I. F. Herbut, V. Juričić, and O. Vafek, Relativistic Mott criticality in graphene, Phys. Rev. B **80**, 075432 (2009).

[36] S. Hesselmann, Thermal phase transitions in the vicinity of two-dimensional quantum critical points, Master thesis (2015).

[37] M. A. Stephanov, Dimensional reduction and quantum-to-classical reduction at high temperatures, Phys. Rev. D **52**, 3746 (1995).

[38] L. Onsager, Crystal statistics. i. a two-dimensional model with an order-disorder transition, Phys. Rev. **65**, 117 (1944).

[39] G. Kamieniarz and H. W. J. Blote, The non-interacting hard-square lattice gas: Ising universality, Journal of Physics A: Mathematical and General **26**, 6679 (1993).

[40] W. Selke, The critical binder cumulant for isotropic ising models on square and triangular lattices, Journal of Statistical Mechanics: Theory and Experiment **2007**, P04008 (2007).

[41] M. E. Fisher, The theory of equilibrium critical phenomena, Reports on Progress in Physics **30**, 615 (1967).

[42] K. Harada, Bayesian inference in the scaling analysis of critical phenomena, Phys. Rev. E **84**, 056704 (2011).

[43] F. Höfling, C. Nowak, and C. Wetterich, Phase transition and critical behavior of the d=3 gross-neveu model, Phys. Rev. B **66**, 205111 (2002).

[44] L. Rosa, P. Vitale, and C. Wetterich, Critical exponents of the gross-neveu model from the effective average action, Phys. Rev. Lett. **86**, 958 (2001).

[45] G. P. Vacca and L. Zambelli, Multimeson yukawa interactions at criticality, Phys. Rev. D **91**, 125003 (2015).

[46] E. Huffman and S. Chandrasekharan, Fermion bag approach to Hamiltonian lattice field theories in continuous time, Phys. Rev. D **96**, 114502 (2017).

[47] F. Parisen Toldin, M. Hohenadler, F. F. Assaad, and I. F. Herbut, Fermionic quantum criticality in honeycomb and π-flux hubbard models: Finite-size scaling of renormalization-group-invariant observables from quantum monte carlo, Phys. Rev. B **91**, 165108 (2015).

[48] Y. Otsuka, S. Yunoki, and S. Sorella, Universal quantum criticality in the metal-insulator transition of two-dimensional interacting dirac electrons, Phys. Rev. X **6**, 011029 (2016).

[49] M. Schuler, S. Whitsitt, L.-P. Henry, S. Sachdev, and A. M. Läuchli, Universal Signatures of Quantum Critical Points from Finite-Size Torus Spectra: A Window into the Operator Content of Higher-Dimensional Conformal Field Theories, Phys. Rev. Lett. **117**, 210401 (2016).

[50] C. Holm and W. Janke, Critical exponents of the classical three-dimensional heisenberg model: A single-cluster monte carlo study, Phys. Rev. B **48**, 936 (1993).

[51] M. Campostrini, M. Hasenbusch, A. Pelissetto, P. Rossi, and E. Vicari, Critical exponents and equation of state of the three-dimensional heisenberg universality class, Phys. Rev. B **65**, 144520 (2002).

[52] Z.-X. Li, Y.-F. Jiang, and H. Yao, Fermion-sign-free Majarana-quantum-Monte-Carlo studies of quantum critical phenomena of Dirac fermions in two dimensions, New J. Phys. **17**, 085003 (2015).

[53] L. Iliesiu, F. Kos, D. Poland, S. S. Pufu, D. Simmons-Duffin, and R. Yacoby, Bootstrapping 3D fermions, J. High Energ. Phys. **2016**, 120 (2016), 1508.00012 .

[54] B. Knorr, Ising and Gross-Neveu model in next-to-leading order, Phys. Rev. B **94**, 245102 (2016).

[55] N. Zerf, L. N. Mihaila, P. Marquard, I. F. Herbut, and M. M. Scherer, Four-loop critical exponents for the Gross-Neveu-Yukawa models, Phys. Rev. D **96**, 096010 (2017).

[56] L. Iliesiu, F. Kos, D. Poland, S. S. Pufu, and D. Simmons-Duffin, Bootstrapping 3D fermions with global symmetries, J. High Energ. Phys. **2018**, 36 (2018).

[57] B. Knorr, Critical chiral Heisenberg model with the functional renormalization group, Phys. Rev. B **97**, 075129 (2018).

[58] J. L. Cardy, Conformal invariance and surface critical behavior, Nuclear Physics B **240**, 514 (1984).

[59] S. Whitsitt and S. Sachdev, Transition from the $\mathbb{Z}_2$ spin liquid to antiferromagnetic order: Spectrum on the torus, Phys. Rev. B **94**, 085134 (2016).

[60] S. Whitsitt, M. Schuler, L.-P. Henry, A. M. Läuchli, and S. Sachdev, Spectrum of the Wilson-Fisher conformal field theory on the torus, Phys. Rev. B **96**, 035142 (2017).

[61] S. Capponi and A. M. Läuchli, Phase diagram of interacting spinless fermions on the honeycomb lattice: A comprehensive exact diagonalization study, Phys. Rev. B **92**, 085146 (2015).

[62] G. W. Semenoff, Condensed-Matter Simulation of a Three-Dimensional Anomaly, Phys. Rev. Lett. **53**, 2449 (1984).

[63] F. D. M. Haldane, Model for a Quantum Hall Effect without Landau Levels: Condensed-Matter Realization of the "Parity Anomaly", Phys. Rev. Lett. **61**, 2015 (1988).

[64] C.-Y. Hou, C. Chamon, and C. Mudry, Electron Fractionalization in Two-Dimensional Graphenelike Structures, Phys. Rev. Lett. **98**, 186809 (2007).

[65] S. Ryu, C. Mudry, C.-Y. Hou, and C. Chamon, Masses in graphenelike two-dimensional electronic systems: Topological defects in order parameters and their fractional exchange statistics, Phys. Rev. B **80**, 205319 (2009).

[66] A. M. Läuchli, Numerical simulations of frustrated systems, in *Introduction to Frustrated Magnetism* (Springer, 2011) pp. 481–511.

[67] A. Wietek and A. M. Läuchli, Sublattice coding algorithm and distributed memory parallelization for large-scale exact diagonalizations of quantum many-body systems, Phys. Rev. E **98**, 033309 (2018).

[68] L. Wang, Y.-H. Liu, J. Imriška, P. N. Ma, and M. Troyer, Fidelity Susceptibility Made Simple: A Unified Quantum Monte Carlo Approach, Phys. Rev. X **5**, 031007 (2015).

[69] H.-K. Tang, J. N. Leaw, J. N. B. Rodrigues, I. F. Herbut, P. Sengupta, F. F. Assaad, and S. Adam, The role of electron-electron interactions in two-dimensional Dirac fermions, Science **361**, 570 (2018).

[70] C. Wetterich, Exact evolution equation for the effective potential, Phys. Lett. **B301**, 90 (1993).

[71] W. Metzner, M. Salmhofer, C. Honerkamp, V. Meden, and K. Schönhammer, Functional renormalization group approach to correlated fermion systems, Rev. Mod. Phys. **84**, 299 (2012).

[72] C. Platt, W. Hanke, and R. Thomale, Functional renormalization group for multi-orbital Fermi surface instabilities, Advances in Physics **62**, 453 (2013).

[73] G. A. H. Schober, K.-U. Giering, M. M. Scherer, C. Honerkamp, and M. Salmhofer, Functional renormalization and mean-field approach to multiband systems with spin-orbit coupling: Application to the Rashba model with attractive interaction, Phys. Rev. B **93**, 115111 (2016).

[74] M. Salmhofer and C. Honerkamp, Fermionic Renormalization Group Flows: Technique and Theory, Progress of Theoretical Physics **105**, 1 (2001).

[75] D. D. Scherer, M. M. Scherer, and C. Honerkamp, Correlated spinless fermions on the honeycomb lattice revisited, Phys. Rev. B **92**, 155137 (2015).

[76] D. D. Scherer, M. M. Scherer, G. Khaliullin, C. Honerkamp, and B. Rosenow, Unconventional pairing and electronic dimerization instabilities in the doped Kitaev-Heisenberg model, Phys. Rev. B **90**, 045135 (2014).

[77] A. M. Black-Schaffer and C. Honerkamp, Chiral d -wave superconductivity in doped graphene, Journal of Physics: Condensed Matter **26**, 423201 (2014).

[78] S. Wessel, Phase diagram of interacting bosons on the honeycomb lattice, Phys. Rev. B **75**, 174301 (2007).

[79] J. Y. Gan, Y. C. Wen, J. Ye, T. Li, S.-J. Yang, and Y. Yu, Extended bose-hubbard model on a honeycomb lattice, Phys. Rev. B **75**, 214509 (2007).

[80] S. Pujari, T. C. Lang, G. Murthy, and R. K. Kaul, Interaction-induced dirac fermions from quadratic band touching in bilayer graphene, Physical Review Letters **117** (2016), 10.1103/physrevlett.117.086404.

[81] C. Honerkamp, Influence of hopping self-energy effects and quasiparticle degradation on the antiferromagnetic ordering in the bilayer honeycomb hubbard model, Physical Review B **96** (2017), 10.1103/physrevb.96.245134.

[82] S. Hesselmann, C. Honerkamp, S. Wessel, and T. C. Lang, Quantifying the fragility of unprotected quadratic band crossing points, Phys. Rev. B **101**, 075128 (2020).